

Index 35726 X
ISSN 0867-888X

POLISH
ACADEMY
OF SCIENCES
INSTITUTE
OF FUNDAMENTAL
TECHNOLOGICAL
RESEARCH

NATIONAL
ENGINEERING
SCHOOL
OF METZ

ENGINEERING TRANSACTIONS

ROZPRAWY INŻYNIERSKIE - TRAITE d'INGENIERIE



QUARTERLY
VOLUME 61
ISSUE 4

WARSZAWA - METZ 2013



Faster online
<http://et.ippt.pan.pl>

Contents of issue 4 vol. LXI

- 239 P. NAISSON, J. RECH, H. PARIS, *Characterization of friction properties during machining of various stainless steels*
- 249 V. GYLIENE, V. OSTASEVICIUS, *The validation of Fe modeling of orthogonal turning process using Cowper–Symonds material behavior law*
- 265 CH.F. MARKIDES, S.K KOURKOULIS, *Revisiting the reflected caustics method: the accurate shape of the “initial curve”*
- 289 W. MOĆKO, T. SZYMCZAK, Z.L. KOWALEWSKI, *Mechanical properties of AW8S-V polyester composite under various loading conditions*
- 301 A. MASSAQ, A. RUSINEK, M. KLÓSAK, *Method for determination of the dynamic elastic modulus for composite materials*
- 317 FROM THE EDITORIAL BOARD, *Our Reviewers*

Copyright ©2013 by Institute of Fundamental Technological Research
Polish Academy of Sciences, Warsaw, Poland

Aims and Scope

ENGINEERING TRANSACTIONS promotes research and practise in engineering science and provides a forum for interdisciplinary publications combining mechanics with material science, electronics (mechatronics), medical science and biotechnologies (biomechanics), environmental science, photonics, information technologies and other engineering applications. The Journal publishes original papers covering a broad area of research activities including experimental and hybrid techniques as well as analytical and numerical approaches. Engineering Transactions is a quarterly issued journal for researchers in academic and industrial communities.

INTERNATIONAL COMMITTEE

S. A. ASTAPCIK (<i>Byelorussia</i>)	P. PERZYNA (<i>Poland</i>)
A. CARPINTERI (<i>Italy</i>)	L. TOTH (<i>France</i>)
G. DOBMANN (<i>Germany</i>)	Z. WESOŁOWSKI (<i>Poland</i>)
T. IWAMOTO (<i>Japan</i>)	P. WOOD (<i>U.K.</i>)
A. N. KOUNADIS (<i>Greece</i>)	G. VOYIADJIS (<i>USA</i>)
J. LIN (<i>U.K.</i>)	R. ZAERA (<i>Spain</i>)
T. ŁODYGOWSKI (<i>Poland</i>)	

EDITORIAL COMMITTEE

R. PECHERSKI – Editor	A. RUSINEK – Co Editor
Z. AZARI	K. KOWALCZYK-GAJEWSKA
P. CHEVRIER	Z. KOWALEWSKI
B. GAMBIN	P. LIPIŃSKI
J. HOLNICKI-SZULC	K. KRIEGEL – assistant of the Co Editor
	ENIM, 1 route d'Ars Laquenexy
	57078 Metz Cedex 03
	Phone: +33 3 87344266, E-mail: relinter@enim.fr

J. ŻYCHOWICZ-POKULNIEWICZ – secretary

Address of the Editorial Office:
Engineering Transactions
Institute of Fundamental Technological Research
Pawińskiego 5B, PL 02-106 Warsaw, Poland

Phone: (48-22) 826 12 81 ext. 206, Fax: (48-22) 826 98 15, E-mail: engtrans@ippt.pan.pl

Abstracted/indexed in:

Applied Mechanics Reviews, Current Mathematical Publications, Elsevier, EMBASE, Engineering Village, Inspec, Mathematical Reviews, MathSci, Reaxys, Scopus, Zentralblatt für Mathematik.

<http://et.ippt.pan.pl/>

Address of the Editorial Office:

Engineering Transactions
Institute of Fundamental Technological Research
Pawińskiego 5B
PL 02-106 Warsaw, Poland
Phone: (48-22) 826 12 81 ext. 206, Fax: (48-22) 826 98 15
E-mail: engtrans@ippt.pan.pl

SUBSCRIPTIONS

**Subscription orders for all journals edited by Institute of Fundamental Technological Research (IPPT) may be sent directly to the Publisher: Institute of Fundamental Technological Research
e-mail: subscribe@ippt.pan.pl**

Please transfer the subscription fee to our bank account:
Payee: IPPT PAN
Bank: Pekao S.A. IV O/Warszawa
Account number 05124010531111000004426875.

WARUNKI PRENUMERATY

Prenumeratę na wszystkie czasopisma wydawane przez Instytut Podstawowych Problemów Techniki PAN przyjmuje Dział Wydawnictw IPPT.

Bieżące numery Engineering Transactions można nabyć bezpośrednio w Redakcji:

**ul. Pawińskiego 5B, 02-106 Warszawa
Tel.: (48-22) 826 60 22; Fax: (48-22) 826 98 15
e-mail: subscribe@ippt.pan.pl**

Characterization of Friction Properties During Machining of Various Stainless Steels

Pierre NAISSON^{1), 2), 3)}, Joël RECH¹⁾, Henri PARIS²⁾

¹⁾ *Université de Lyon, Ecole Nationale d'Ingénieurs de Saint Etienne*
LTDS, CNRS UMR 5513, 58 rue Jean Parot, 42000 Saint Etienne, France
e-mail: pierre.naisson@enise.fr

²⁾ *Université de Grenoble, Université Joseph Fourier*
G-SCOP, 46 avenue Félix Viallet, 38031, Grenoble cedex 1

³⁾ *CETIM*
7 rue de la presse, BP802, 42952 Saint-Etienne cedex 9

Many issues in machining are related to interface characteristics, such as the friction coefficient, adhesive layer, or heat transfer coefficient. A specially designed tribometer is used to quantify these contact parameters in the case of four stainless steels (three austenite grade with controlled composition and an austenite-ferritic one). The sensitivity to sliding velocity and coatings is investigated. It is highlighted that the contact pressure effect is limited compared with the influence of sliding speed. Moreover, tool damage can also be explained by local phenomena exhibited by the tribometer, such as adhesion layer or thermal aspects, which are critical in case of stainless steels.

Key words: friction, tribometer, stainless steels.

1. INTRODUCTION

Stainless steels are extensively used in industry, for a large range of applications such as medical, nuclear, or aeronautics. In the field of machining processes, a major objective consists in predicting cutting tools performance. Some authors have proposed analytical or numerical predictive models for material removal mechanisms. However, friction modelling at the tool/work-material interface remains an issue. Indeed, scientific literature [1, 2] reports that machining stainless steel induces intensive thermal and mechanical loads (temperatures 500 to 1000°C, contact pressures up to 3 GPa, and friction velocity from 0 to 400 m·min⁻¹) which makes it difficult to simulate by a tribological test. Moreover, it is obvious that cutting operations can be considered as “open

tribo-systems”, as defined by ZAMBELLI in [3], i.e. cutting tools rub continuously against a refreshed surface.

There are two main ways to investigate friction in cutting. The first approach consists in comparing forces during elementary cutting operations. FROMENTIN propose in [4] to use a tap test to measure influence of lubricants on friction and diffusive properties. HARRIS [5] used drilling tests to understand wear behaviour of multi-layer coatings, while EZUGWU [6] use intermittent cutting test of TiN coated inserts for tool life prediction. These methods ensure relevant friction conditions. Unfortunately, macroscopic forces do not provide quantitative value of local friction coefficients and heat partition coefficient along the interface.

Moreover, BONNET *et al.* [7] have shown that friction properties vary continuously along this interface during the machining of an AISI316L stainless steel depending on local sliding velocity and pressure (Fig. 1). There is a need for a dedicated friction test simulating relevant conditions (pressure, velocity and open tribo-system). Thus, ZEMZEMI developed a special tribometer [8] providing friction coefficient, heat flux, and adhesion. This system has been improved by CLAUDIN [9] to characterize the frictional properties of various steel grades in machining under a larger range of sliding velocity, like CLAUDIN [10] or RECH [11].

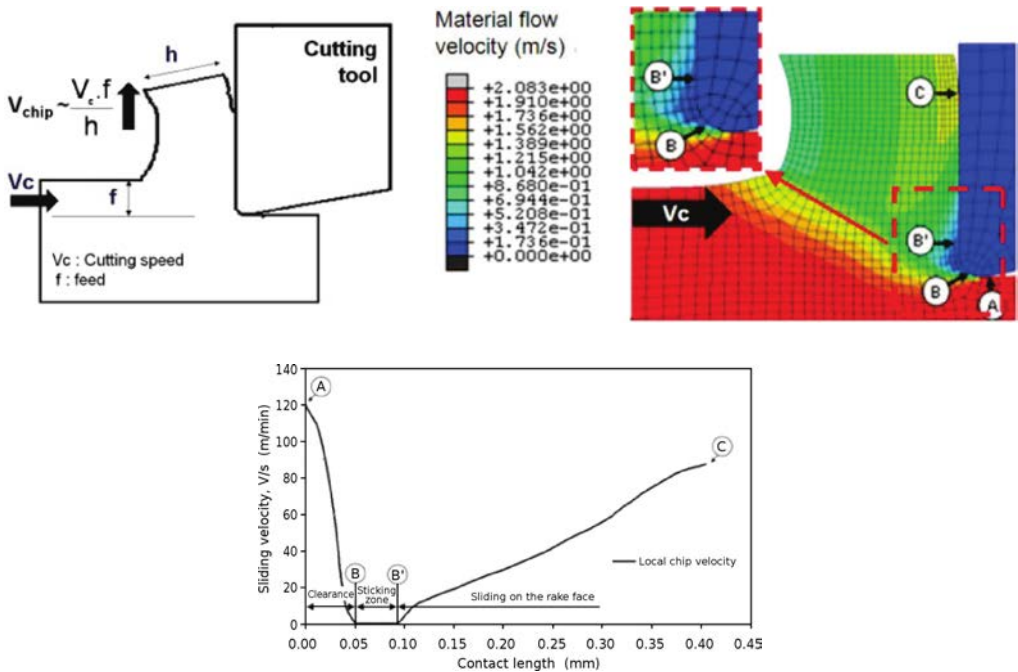


FIG. 1. Illustration of strategic zones in orthogonal cutting [7].

The present paper aims at applying this tribometer to quantify the frictional properties in machining of stainless steel grades for a large range of sliding velocities. The 4404HM (i.e. AISI316L) and 4305HM (i.e. AISI303) are austenitic grade, both with a special heat and chemical treatment improving their machinability. The 4441 is an austenitic grade with a highly controlled composition designed for medical application. This material is well known as a difficult one to machine, as is the 4362, which is a duplex austenite ferrite grade. In addition, the sensitivity of one of these work-material to cutting tool coatings is also evaluated.

2. EXPERIMENTAL SETUP

The tribometer (Fig. 2) has been used already in various published work [7, 10, 12]. The work-material is a cylindrical bar of stainless steel, and cutting tool is a cemented carbide pin, with a 10% Co and grain size closed to $0.8 \mu\text{m}$. The sliding area of the pin is polished to reach a roughness R_a lower than $0.3 \mu\text{m}$. Three different sliding speeds of 20, 60, and $180 \text{ m}\cdot\text{min}^{-1}$ have been chosen, in order to simulate a large range of cutting conditions. A refreshing procedure is applied before each friction test, consisting in a turning phase followed by a belt finishing phase, to ensure a relative stability in mechanical state of the material.

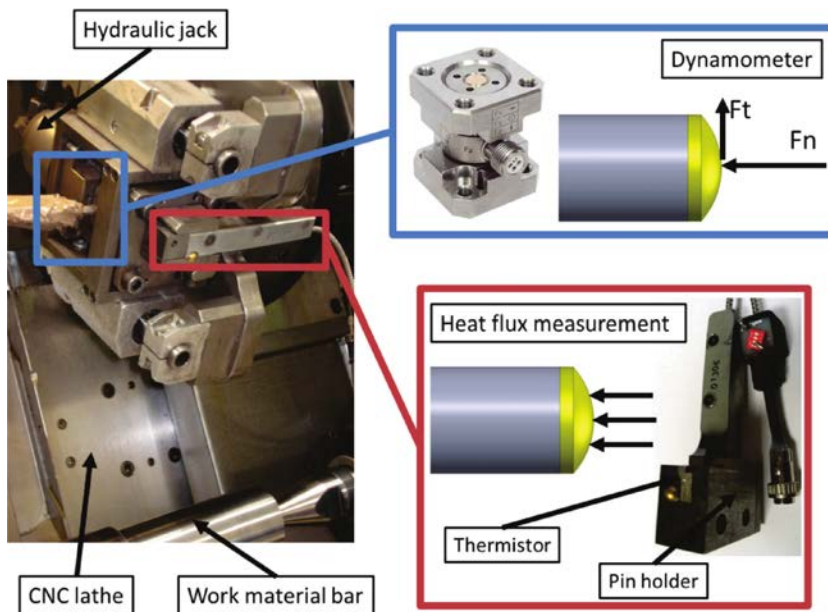


FIG. 2. Design of the tribometer used.

For each test, the tribometer provides normal and tangential forces through a dynamometer, while the pin holder is instrumented to estimate the heat flow transmitted to the pin. From two force components in the stabilized phase, it's possible to calculate apparent friction coefficient (2.1). As presented in [13], the apparent friction coefficient can be divided into an adhesive friction coefficient μ_{adh} and a plastic deformation coefficient μ_{def} .

$$(2.1) \quad \mu_{\text{app}} = \frac{F_t}{F_n} = \mu_{\text{def}} + \mu_{\text{adh}}.$$

An analytical method has been developed in [13] to identify adhesive friction coefficient μ_{adh} from the apparent friction coefficient μ_{app} . BONNET *et al.* have shown in [7] that the adhesive part μ_{adh} is close to 90% of the apparent friction coefficient μ_{app} in the case of a 316L austenitic stainless steel (which is close to 4404HM in term of composition and work-material characteristics). CLAUDIN has arrived at [10] the same conclusion in the case of AISI 1045 steel with TiN coated pins. This model will not be presented in this paper because similar qualitative conclusions can be announced with μ_{app} or with μ_{adh} .

The tribometer also provides the heat flux transmitted to pin ϕ_{pin} . This heat flux is only part of the total heat flux generated at the interface. The fraction β of heat transmitted to pins, also called heat partition coefficient, is provided by Eq. (2.2), with V_g the sliding velocity (m/s).

$$(2.2) \quad \beta = \frac{\phi_{\text{pin}}}{F_t \times V_g}.$$

The work-material in this study is stainless steel. Four different steels have been chosen in order to measure influence of composition or microstructure over frictional behaviour. Table 1 give chemical composition (percentage of volume) and grade type.

Table 1. Chemical composition of the stainless steels tested.

Name	Structure	C	Si	Mn	Ni	Cr	Mo	Cu	P	S
4404HM	Austenitic	≤ 0.03	≤ 1	≤ 2	11	17	2.2	≤ 0.75	≤ 0.04	0.025
4441	Austenitic, electro-slag-remelted	0.03	1.00	2.00	14	18	2.9	–	0.025	0.01
4362	Duplex austenitic / ferritic	≤ 0.03	≤ 1	≤ 2	4.5	23	0.35	0.4	≤ 0.04	≤ 0.02
4305HM	Austenitic + resulphurised	< 0.07	< 0.75	1.8	9	17.5	< 0.5	< 0.75	< 0.04	0.3

3. FRICTION PARAMETERS ANALYSIS

3.1. Influence of contact pressure and sliding velocity

The tribometer allows adjusting both pin diameter and normal force in order to influence the contact pressure. Three pin diameters (9, 13 and 17 mm) and two normal forces (1000 N and 650 N in case of 17 mm diameter pin) have been chosen with TiN coated pins. The following graphs (Fig. 3) show the evolution of friction parameters *versus* sliding speeds for a 4441 stainless steel grade.

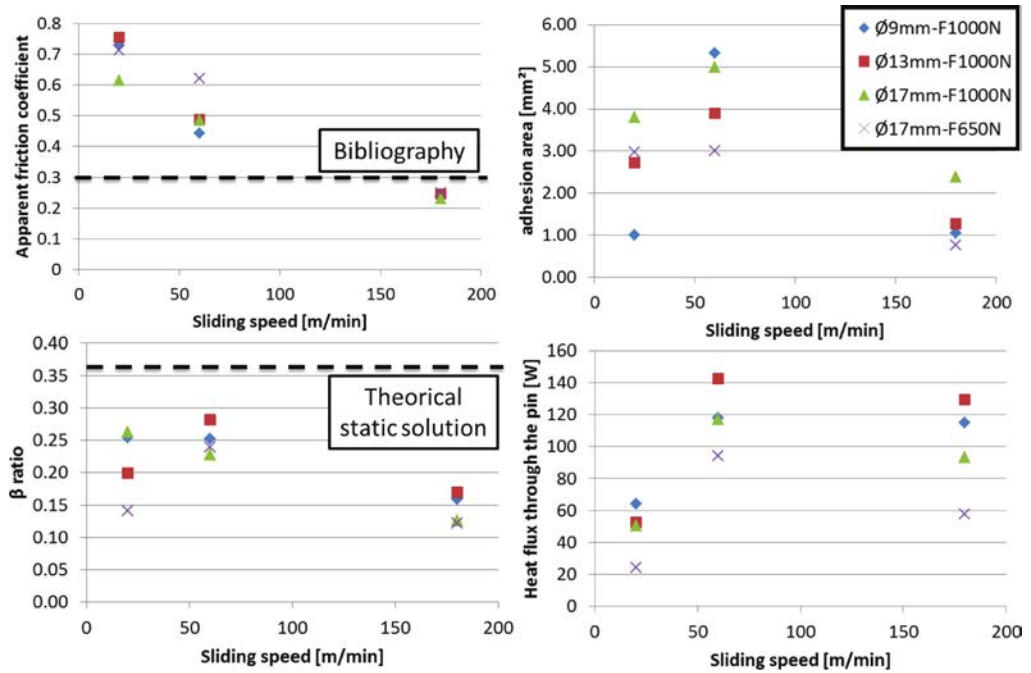


FIG. 3. Influence of contact pressure and sliding velocity on friction properties.

One can observe that both the friction coefficient and the heat partition ratio depend on sliding speed, which is not mentioned in literature (with disc/pin method in one hand [7], or static effusivity ratio on other hand [14]). It shows that sliding velocity has much more influence than contact pressure on the friction coefficient and heat partition coefficient. When increasing sliding velocity, the friction coefficient decreases. This trend has already been observed in several previous papers [7, 10, 12], including a similar grade. On the contrary, the heat partition coefficient exhibits an unusual behaviour. Heat partition coefficient commonly decreases with increasing sliding speed. In the case of stainless steels however, the fraction β is significantly lower at low speed which is very different

from the tribological properties of conventional steels leading to a continuous decrease.

However, it is obvious that contact pressure increases when normal force increases or when pins diameter decreases. Despite the variation of contact pressure, friction coefficient and heat partition ratio (β) are influenced under low sliding velocities whereas they remain almost constant under high sliding velocities. It appears that a higher contact pressure leads to a lower friction coefficient under low sliding velocities. On the contrary, a higher heat partition ratio is obtained for high contact pressure.

3.2. Sensitivity to cutting tool coatings

In this test, only the 4441 austenitic steel grade (highly controlled composition grade) is involved since it is considered as a difficult to cut material due to its thermal properties and to its capacity to induce adhesion on cutting tools. For a defined contact pressure configuration ($F_n = 1000$ N, $d = 17$ mm), TiN and AlTiN coatings are investigated. As shown in Fig. 4, TiN coating exhibits the lowest friction coefficient under low sliding velocities. On the contrary, both coatings lead to similar friction coefficients under high sliding velocities. Deviations in measurement are not plotted here because they are not significant.

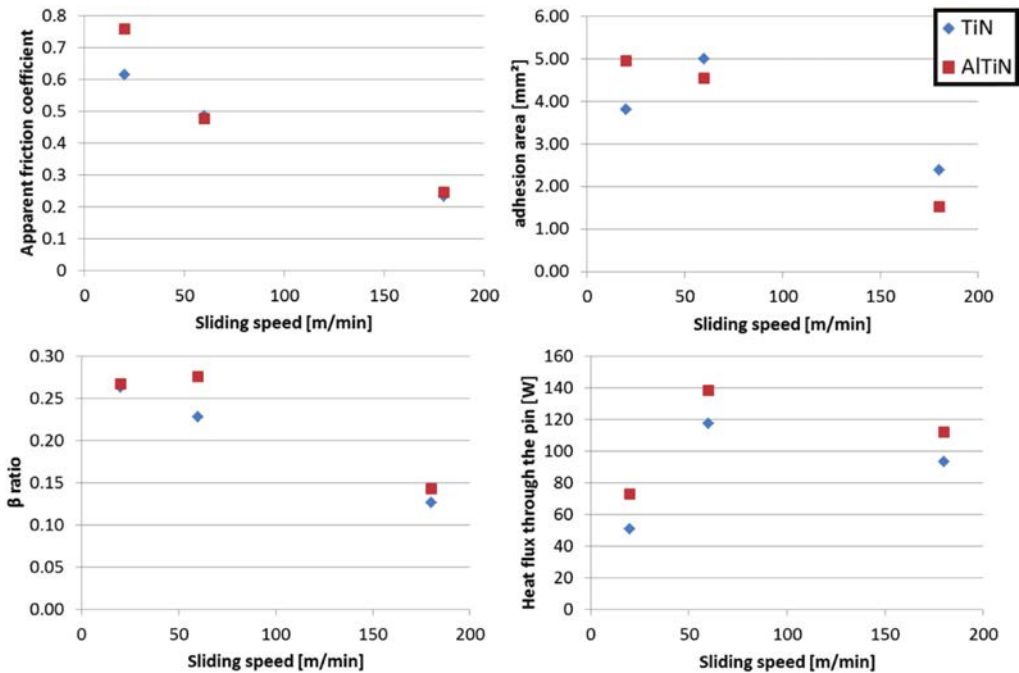


FIG. 4. Influence of coatings on friction coefficient and heat partition ratio.

Concerning the affect on thermal properties, TiN coating leads to smaller heat partition coefficient. As a consequence these two properties of TiN coatings enable to decrease the amount of heat transmitted to pins as shown in Fig. 5. Moreover, adhesion at low speed is greater for AlTiN. So, TiN coating seems to be more appropriate for austenitic steel machining. This observation has now to be correlated with wear tests in order to investigate the chemical wear resistance of both coatings which cannot be estimated through such rapid friction tests.

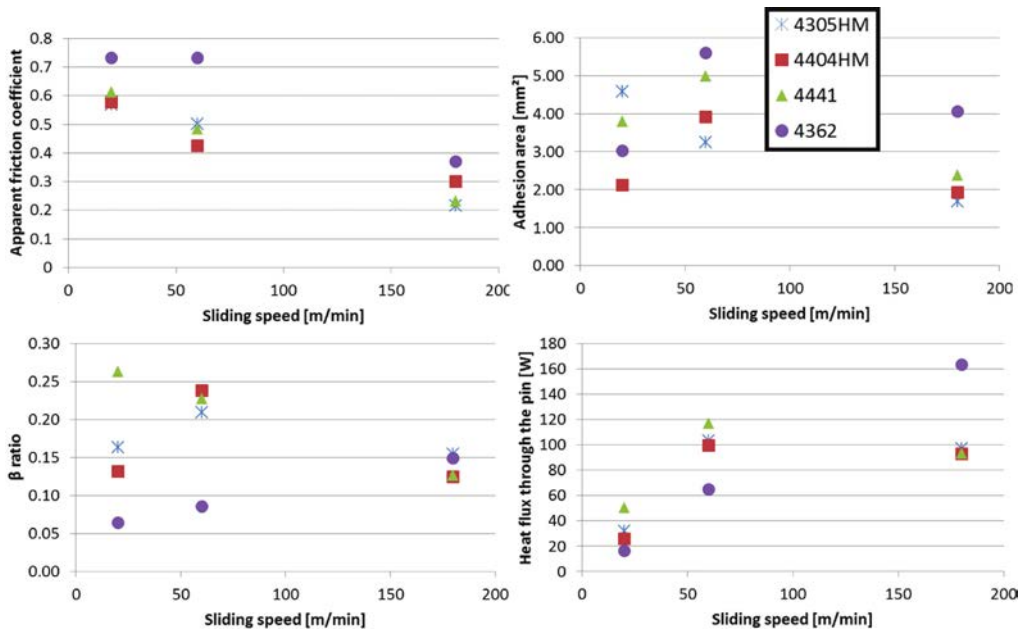


FIG. 5. Friction properties of various stainless steel.

3.3. Influence of work-material

In this section, only TiN coated pins are considered to investigate the influence of the work-material. Pins with a 9 mm diameter are used under a normal force of 1000 N. Concerning the evolution of friction coefficient; Fig. 5 reveals that the duplex austenite-ferritic grade (4362) leads to much higher friction coefficients than other grades. On the contrary, the heat partition ratio is very small in this case. As a consequence, a stronger adhesion occurs, especially at high speed and, at the same time, this adhesion induces a thermal insulation effect.

From a productivity point of view, end users are interested in high cutting speeds. When machining austenite-ferritic grades, they will face higher fric-

tion coefficient and about three time higher thermal conductivity compared to austenitic grades. While conductivity trends to a faster evacuation of heat generated at the interface in the work-material, the higher friction coefficient leads to about 30% more energy production in contact zone. Finally, at low speed, 4362 absorbs most part of energy, while at higher speeds, the tool have to resist to a significantly higher amount of energy.

Austenite-ferritic grades will induce both higher mechanical strength and higher thermal loads on cutting tools. More precisely, they will induce higher thermo-mechanical loads in some tool/work-material interface where sliding speeds will be high (see Fig. 1). As an example at the end of the flank face and at the end of the rake face. So there is a higher risk of crater wear in such zones. This result is in accordance to the well-known poor machinability of such grades, and is represented by adhesion on the pin, as one can observe in Fig. 6 (contour of adhesion area is highlighted).

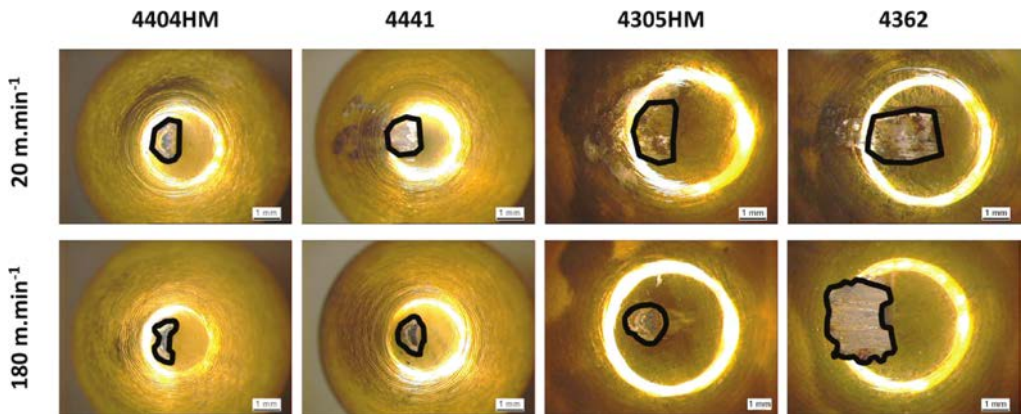


FIG. 6. Adhesion phenomenon for TiN coated pin at $20 \text{ m}\cdot\text{min}^{-1}$ (top) and $180 \text{ m}\cdot\text{min}^{-1}$ (bottom).

By comparing the austenitic grades 4404HM and 4305HM, it seems that they lead to similar friction coefficient and heat partition coefficient. In this case, the tribometer is not able to discriminate a variation of machinability induce by resulphurising process. On the contrary the low machinability austenitic grade 4441 leads to higher friction coefficient under low sliding velocities, whereas no difference are observable under high sliding velocities compared to the same material but in its high machinability grade 4404HM. Concerning the thermal behaviour, it appears that the heat partition ratio of the low machinability grade is higher than the high machinability grade. As a consequence, a larger amount of heat is transmitted to pins under low sliding velocities. The consequence of these observations is that 4441 grade will lead to higher adhesion at

the tool/work-material interface where sliding velocity is low. This is especially observed around the cutting tool edge. As a consequence, a higher sensitivity to built-up edge can be expected with such grades. These tribological observations are in accordance with experimental observations in cutting.

4. CONCLUSION

The present work has presented the application of a tribometer dedicated to the characterization of the frictional properties at the tool/work-material interface for four various stainless steel grades. It has been shown that sliding velocity is the major parameter influencing friction coefficient and heat partition coefficient in any cases. The higher the sliding velocity is, the lower the friction coefficient and the heat partition coefficient are. But at low speed, stainless steel grades present a significantly lower heat partition ratio, which is quite different from usual steel material.

In the case of austenitic stainless steels, the TiN coating seems to lead to lower friction coefficients and heat partition ratio compared to AlTiN coatings. Concerning the influence of work-material, it seems that austenite-ferritic grades exhibits higher friction coefficient and at the same time a lower heat partition coefficient compared to other grades, which make cutting tools sensitive to crater wear.

The tribometer does not allow one to discriminate any large difference between austenitic high machinability grades, whereas high purity controlled austenitic grade have exhibited higher friction coefficient and heat partition coefficient under low sliding velocities which confirms its ability to built-up edge creation.

In order to compare machinability of stainless steels, and influence of composition and micro-structure, tool wear tests have to be conducted. Observation and measure of built-up or crater wear can confirmed our conclusions on the influence of work-material composition and structure over tribological phenomenon.

ACKNOWLEDGMENT

Authors would like to express their gratitude to the partners of FGVV program and especially to the CETIM for financial support to this study, to THERMIPLATIN for the coatings deposition and to UGITECH for the stainless steel furniture. This work was carried out within the context of the working group Manufacturing'21 which gathers 16 French research laboratories. The topics approached are modelling of the manufacturing process, virtual machining, emerging manufacturing methods.

REFERENCES

1. TRENT E.M., WRIGHT P.K., *Metal Cutting*, 4th ed., Butterworth-Heinemann, 2000, ISBN 075067069X.
2. STEPHENSON D.A., AGAPIOU, J.S., *Metal Cutting Theory and Practice*, 2nd ed., Taylor and Francis CRC Press, 2005, ISBN 9780824758882.
3. ZAMBELLI G., VINCENT L., *Matériaux et contacts*, Presses polytechniques et universitaires romandes, 1998, ISBN 9782880743383.
4. FROMENTIN G., BIERLA A., MINFRAY C., POULACHON G., *An experimental study on the effects of lubrication in form tapping*, Tribology International, **43**, 9, 1726–1734, 2010.
5. HARRIS S.G., DOYLE E.D., VLASVELD A.C., AUDY J., QUICK, D., *A study of the wear mechanisms of Ti1-xAlxN and Ti1-x-yAlxCryN coated high-speed steel twist drills under dry machining conditions*, Wear, **254**, 7-8, 723–734, 2003.
6. EZUGWU E.O., OKEKE C.I., *Tool life and wear mechanisms of TiN coated tools in an intermittent cutting operation*, Journal of Materials Processing Technology, **116**, 1, 10–15, 2001.
7. BONNET C., VALIORGUE F., RECH J., CLAUDIN C., HAMDI H., BERGHEAU J.M., GILLES P., *Identification of a friction model-Application to the context of dry cutting of an AISI 316L austenitic stainless steel with a TiN coated carbide tool*, International Journal of Machine Tools and Manufacture, **48**, 11, 1211–1223, 2008.
8. ZEMZEMI F., RECH J., SALEM W.B., DOGUI A., KAPSA P., *Development of a friction model for the tool-chip-workpiece interfaces during dry machining of AISI4142 steel with TiN coated carbide cutting tools*, International Journal of Machining and Machinability of Materials, **2**, 3/4, 361–377, 2007.
9. CLAUDIN C., RECH J., GRZESIK W., *Development of a new tribometer to identify the effects of coatings and lubricants during machining processes*, 2nd International Conference “Innovative Cutting Processes and Smart Machining”, Cluny, 2008.
10. CLAUDIN C., MONDELIN A., RECH, J., FROMENTIN G., *Effects of a straight oil on friction at the tool-workmaterial interface in machining*, International Journal of Machine Tools and Manufacture, **50**, 8, 681–688, 2010.
11. RECH J., CLAUDIN C., D’ERAMO E., *Identification of a friction model – Application to the context of dry cutting of an AISI 1045 annealed steel with a TiN-coated carbide tool*, Tribology International, **42**, 5, 738–744, 2009.
12. ZEMZEMI F., RECH J., SALEM W.B., DOGUI A., KAPSA P., *Identification of a friction model at tool/chip/workpiece interfaces in dry machining of AISI4142 treated steels*, Journal of Materials Processing Technology, **209**, 8, 3978–3990, 2009.
13. CHALLEN J.M., OXLEY P.L.B., *An explanation of the different regimes of friction*, Wear, pp. 229–243, 1979.
14. THERMILYON, *Documentation technique des revêtements*, 2007.

Received revised version September 27, 2012.

The Validation of Fe Modeling of Orthogonal Turning Process Using Cowper–Symonds Material Behavior Law

Virginija GYLIENE, Vytautas OSTASEVICIUS

*Kaunas University of Technology (KTU), Department of Engineering Design
Faculty of Mechanical Engineering and Mechatronics
Kęstučio St. 27, LT-44312 Kaunas, Lithuania; e-mail: virginija.gyliene@ktu.lt*

The article contains a literature review, experimental results, and a Finite Element Model (FEM) composition. Orthogonal turning tests were executed in the range of cutting speeds and feed rate, after every test chip was collected.

Further investigation was done using FE model validation and experimentation, which uses results of the experimental zone in which the built-up edge did not form and the cutting itself is of even plastic deformation.

The essence of this research is that the adequacy of the composed FE model to the real physical process should conform not only to the evaluation of cutting forces, but also to the evaluation of chip form, that is, segmentation frequency.

Key words: orthogonal cutting, FE modelling, deformation rate, chip segmentation.

1. INTRODUCTION

Material removal by cutting remains one of the most common technological processes for producing complex and high-precision components (taking into account the coefficient of component complexity [1]). Research of cutting processes may be subdivided into the following fields: tribology, cutting tools and coatings, environment-friendly machining, vibration phenomena in cutting, machinability, process optimization, component quality, mechatronic problems, improvement of process efficiency, and diagnostics and computer systems [2].

The aforementioned classification demonstrates the multitude of mutually interrelated research fields that are important in studying different cutting processes. The machining research community is particularly interested in the chip formation processes, which deals with material deformation during cutting, including the influence of deformable material on the tool. Cutting forces, temperature, tool wear, friction between tool and chip, machining power, and surface quality are all dependent on chip formation [3]. These physical effects are studied

by means of numerical methods. Mathematical modeling of the associated technological processes involves such important procedures as task description and verification of numerical solution against experimental values obtained during investigation of actual physical processes.

Modeling of cutting processes is predominantly performed by means of simplified approaches, which have been already employed by Tresca and Mallock in their initial research works [1]. One group of researchers has used of finite element procedures for studying the influence of the cutting edge on the cutting process [4–7]. Meanwhile, another group of scientists has focused on investigation of the chip formation mechanism with consideration of aspects of tool durability [8–10]. These studies require physically validated finite element models, which are commonly verified by using experimentally determined cutting forces; though, there is an increasing trend to pay more research attention to the geometrical configuration of the removed chip [11]. Author ZHANG *et al.* [12] proposes an FE model with an improved friction model. Further investigation [12] presents the impact of cutting speed to the morphology of the cutting chip. On the other hand, in cases when numerical and experimental results are compared, the reliability of data used for FEM validation must be ensured too.

A wider scope of investigated parameters and effects in cutting are promoted by increasing the application of explicit numerical schemes during finite element analysis. Engineering analysis software with implemented explicit approaches employ more efficient algorithms for solution of contact and other dynamic problems, thereby reducing required computational time that is directly proportional to size of finite elements [13]. Machining with “low” and “high” cutting velocities leads to increased material deformation rates that may vary in the range of 10^3 – 10^6 s⁻¹ [9]. Thus, characterization of material flow in these conditions is a highly sophisticated problem. Some of the researchers use high-velocity compression and Hopkinson tests for evaluation of material behavior under large strain rates, while others rely on application of experimental results of orthogonal turning in conjunction with finite element analysis [14].

This paper presents experimental results that have obtained in a wide range of cutting velocities with the purpose to avoid formation of built-up edge zones. This experimental research consisted in measurement of cutting forces and characterization of accumulated chips. The actual material characteristics had established by means of tensile testing. For further FE analysis plastic kinematic material deformation model was suited to model isotropic and kinematic hardening plasticity with option of including rate effects. A finite element model had developed for investigation of orthogonal cutting process by employing a tool with a sharp cutting edge. Literature survey indicates that a tool is considered to have a “sharp” edge when its sharpness value is within the limits of 0–31 μm [15–17]. A measurement device was used to determine sharpness of tool edge by

means of method of tangential lines [18, 19]. As it will be reasoned later in this paper, one parameter for FE model validation is not sufficient.

2. EXPERIMENTAL INVESTIGATION

2.1. Turning Experiments

The experimental research was performed for the case of orthogonal cutting with the aim of measuring the generated cutting forces and determining the change of chip form ($F = f(V_c)$, $F = f(p)$). The experimental setup and geometrical approach for FE model composition is presented in Fig. 1.

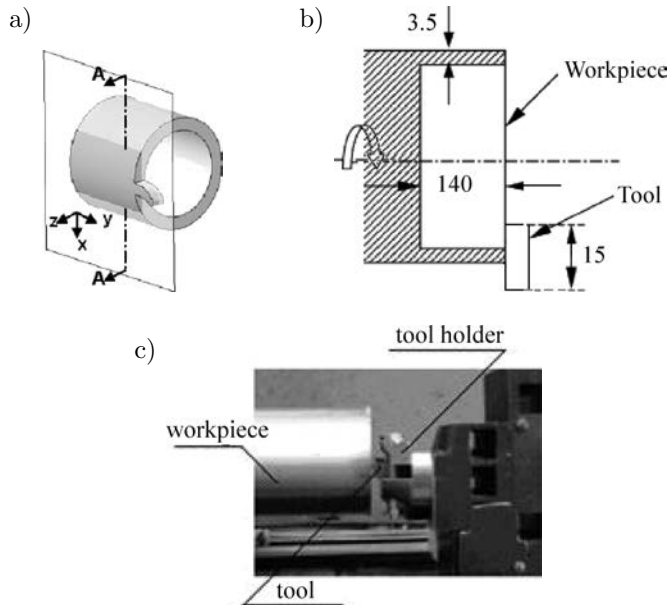


FIG. 1. Schematics of orthogonal turning experiment setup: a) cross-sectional workpiece for FEM (adopted from [20]); b) workpiece dimensions; c) experimental setup.

A special “tube-type” work-piece was fabricated to conduct orthogonal cutting experiments. This type of work-piece is not so commonly used as, for example, disks or toothed shafts. However, the main benefit of the “tube-type” work-piece is that its diameter remains unmodified during orthogonal cutting.

The experiments were carried out by using carbide tool T5K10 (85% WC, 6% TiC, 9% Co), which rake and clearance angles are respectively equal to $\gamma = 0^\circ$, $\alpha = 20^\circ$. The tool was mounted into a special holder, with strain-gauge dynamometer mounted underneath, thereby enabling measuring of tangential (F_T) and radial (F_R) cutting force components. Dynamometer signals were amplified and subsequently processed by means of Picolog software.

Generated chips were collected after each test sequence (each experiment was repeated 3 times) when the workpiece was machined in the range of cutting velocities of 0.42–3.6 m/s and feed rate (or so-called depth of cut, which is the particularity of orthogonal turning process) $p = 0.05 \div 0.1$ mm/rot.

Figure 2a provides the distribution of measured cutting forces, which variation character indicates specific physical phenomena. The presented relationships reveal three distinct zones:

- 1 – zone of low cutting velocities (up to 0.72 m/s), which was characterized by force increase or decrease due to discontinuous formation of chips as well as plastic irregularities.
- 2 – zone of velocities from 0.72 m/s (250 rot/min) till 1.81 m/s (630 rot/min), which was not an optimal cutting condition from the technological point of view because of rapid increase of cutting forces. Figure 2a indicates that maximal values of the tangential force depends on the feed rate, i.e. under lower feed value, maximal tangential force is reached under larger cutting velocities and *vice versa*.
- 3 – zone of velocities up from 1.88 m/s (*in these particular experimental study*), which was characterized by continuous plastic deformation (*without formation of built-up edge*) and settled/decreasing cutting forces.

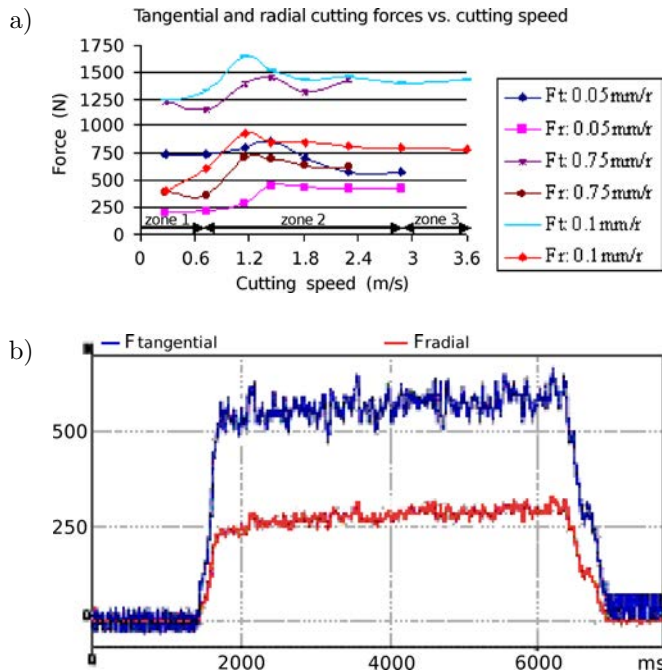


FIG. 2. Cutting forces distribution, assuming cutting speed and cutting feed rate: a) all performed orthogonal tests results; b) measured forces from test: 0.05 mm/rot and 2.88 m/s.

After the cutting experiments, the microsections were prepared and used to determine chip thickness and segmentation frequency. Experimental results that are characteristic to the 3rd zone were subsequently applied for finite element modeling. The chips form of the so-called 3rd zone of cutting was estimated. According to results, presented in Fig. 2a the cutting conditions ($V_c = 2.88$ m/s, $p = 0.05$ mm/rot) were taken for future FE modeling. Figure 3 presents chip form change according to cutting depth. In order to take the pictures, a Nikon Eclipse LV150 microscope was used equipped with an Infinity 1 camera connected to a computer.

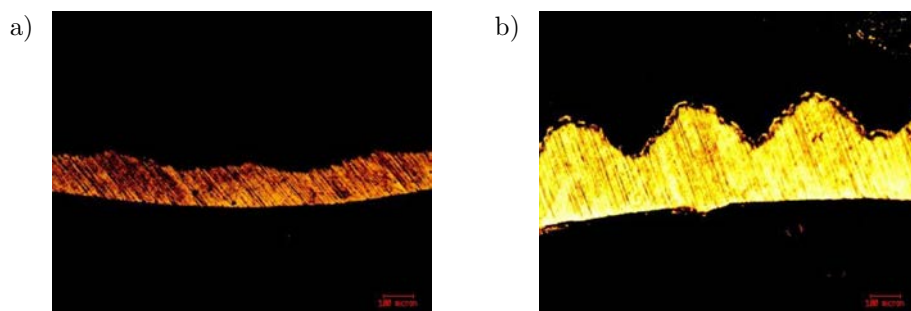


FIG. 3. Chips from 3rd cutting zone according to cutting speed and cutting feed:
 a) $V_c = 2.88$ m/s, $p = 0.05$ mm/rot; b) $V_c = 2.88$ m/s, $p = 0.1$ mm/rot.

To determine the chip segmentation frequency the geometric parameters, as the width of repeated segments were measured. Assuming the shape of chip for cutting speed in the 3rd zone it was defined, that segmentation frequency was about 6.1 kHz and 6.7 kHz respectively for feed 0.05 mm/rot and 0.1 mm/rot.

2.2. Determination of mechanical properties of material

Actual mechanical properties of 35-grade steel (0.32–0.4% C) were determined by tensile testing in order to obtain reliable input data for the developed FE model. During each test the average results of the thickness and load were obtained and approximated to determine the real characteristics of the materials. Figure 4 presents the dependence of the real tension to the deformation.

The material strengthening effect is determined by the material hardness [21]. Rockwell hardness testing yielded the value of 35 HRC for the tested steel material. It is known that cutting of steels of such or similar hardness under both low and high velocities results in formation of continuous chip (*when the feed rate is small*) [22].

Table 1 provides the determined mechanical properties of 35 grade steel, which were applied for construction of deformation law of the material in the finite element model.

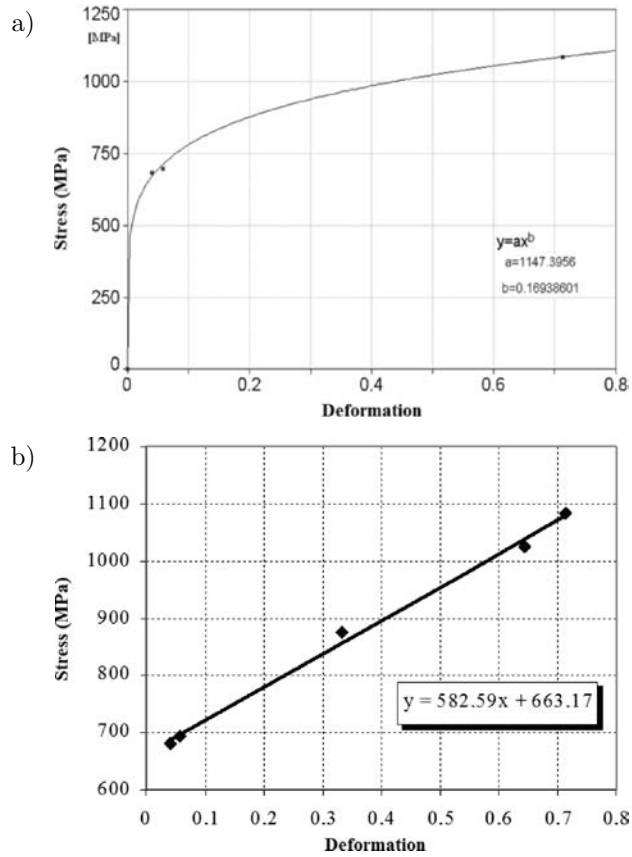


FIG. 4. The dependence of the real stress to the deformation: a) dependence between the stresses and deformation during the testing; b) schematized dependence between the stresses and deformation.

Table 1. Material properties of 35 grade steel.

Characteristics	Defined by Tensile Test	Used in FEM Cowper-Symonds law
Density [kg/m ³]	7800	+
Young modulus [GPa]	200	+
Poisson index [-]	0.29	+
Yield stress [MPa]	663	+
Strength limit [MPa]	698	-
Failure strain [-]	0.72	+
Tangential modulus [MPa]	582.6	+
Hardening index [-]	0.169	-
Cowper-Symonds constants C [s ⁻¹]; P [-]	-	220; 5
Kinematic-isotropic material hardening constants [-]	-	0-1

3. NUMERICAL SIMULATION OF ORTHOGONAL TURNING PROCESS

3.1. Description of the numerical model

LS-DYNA/Explicit FE code was employed for modeling purposes. For 3D modeling and nonlinear dynamic simulations a solid element SOLID164 was used, which consists of 8 nodes with three degrees of freedom at each node in X , Y , Z directions. Both coarse and fine meshing was used in the FE model depending on deformation intensity in the considered zone. The number of finite elements was appropriately reduced by diminishing the size of the FE elements only in the area of contact interaction, which usually requires an extremely fine mesh resulting in huge computational efforts. Figure 5 presents the developed FE model that was divided into several zones, which was accomplished by means of commands *lesize*, *nmgall* of Ansys that was used as a pre-processor environment in this research work. Parameters of the model are as follows: rake angle $\gamma = 0^\circ$, clearance angle $\alpha = 20^\circ$, edge sharpness $r = 13 \mu\text{m}$, cutting depth $p = 0.05 \text{ mm}$. From the results presented in Fig. 5 it was found that the mesh density (8 elements per layer to cut – depth of cut) is sufficient for the accuracy

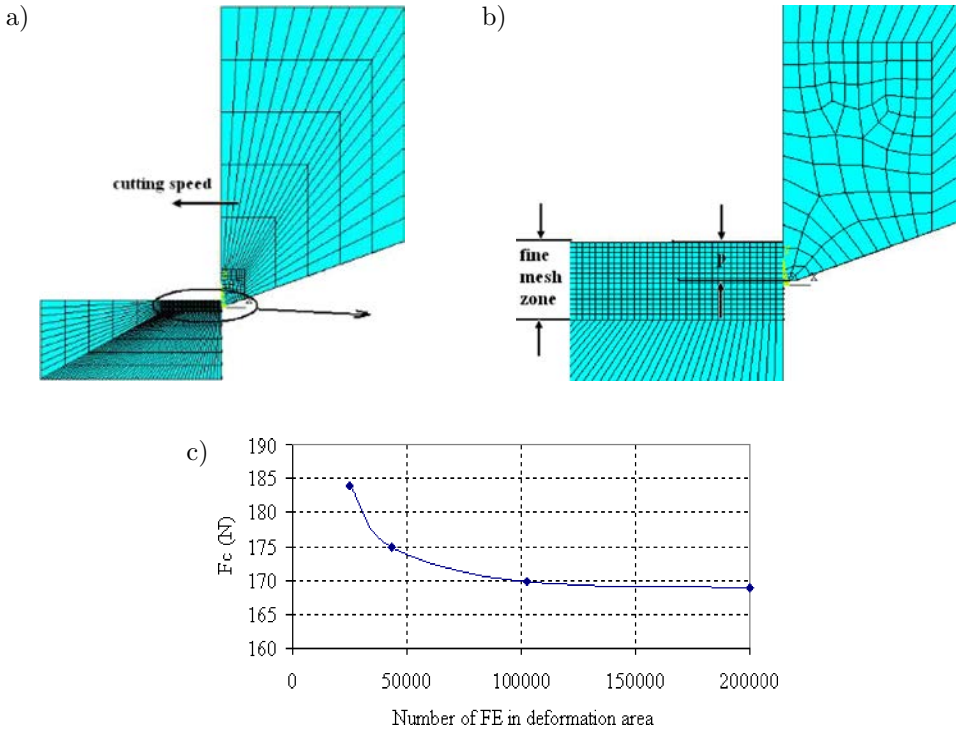


FIG. 5. Finite element model: a) full FE model; b) FE model in detail; c) definition of mesh size (*test without dynamic characteristic*).

according to mesh size. Finally, for time cost saving and the need of small time step the area to remove was diminished to 0.05×0.05 mm (workpiece: 28980 elements). Boundary conditions of the FE model were as follows. The workpiece was constrained in all six DOFs. Load of type $U = f(t)$ was imposed on the tool with the purpose to simulate cutting motion with respect to cutting velocity. Numerical FE model of cutting process was formed evaluating contact between interacting bodies (*deformable body – rigid body*). In *LS-DYNA* package contact interaction between two bodies was formulated using “master–slave” methodology and penalty method. The friction in the contact, in *LS-DYNA* package, is expressed in the following way [23]:

$$(3.1) \quad f = f_s + (f_s - f_d)e^{-DC|V_{\text{rel}}|},$$

here f_d – dynamic coefficient of friction; f_s – static coefficient of friction; DC – exponential decay coefficient; V_{rel} – relative velocity.

A literature survey [24–27] indicates that in the case of our cutting experiments ($p = 0.05$ mm, $V_c = 2.88$ m/s) the coefficient of friction may vary in the range of $\mu = 0.43 \div 0.72$. A value of 0.5 was used for determination of dynamic constants.

The problem as cutting process simulation is classified as high velocity contact–impact interaction problem. So, elastic–plastic material model with kinematic–isotropic hardening was chosen. The strain rate is accounted for by using the Cowper and Symonds model which scales the yield stress by strain rate dependent factor [23]:

$$(3.2) \quad \sigma_Y = \left[1 + \left(\frac{\dot{\epsilon}}{C} \right)^{1/P} \right] (\sigma_{Y0} + \beta E_P \varepsilon_{\text{eff}}^P),$$

where σ_Y , σ_{Y0} – yield stress limits of the material defined with and without the influence of strain rate $\dot{\epsilon}$; P and C are user defined input constants.

The current radius of the yield surface σ_Y is the sum of the initial yield strength σ_{Y0} , plus the growth $\beta E_P \varepsilon_{\text{eff}}^P$, where E_P is the plastic hardening modulus:

$$(3.3) \quad E_P = \frac{E_t E}{E - E_t},$$

where E_t – tangential modulus (MPa), $\varepsilon_{\text{eff}}^P$ – effective plastic strain, β – constant, defining kinematic ($\beta = 0$), isotropic ($\beta = 1$) or kinematic–isotropic hardening ($0 < \beta < 1$).

On the basis of Eq. (3.2), it is clear that the static and dynamic yield stress ratio depends on deformation speed. Values P and C in relation (3.2) and the

kind of hardening hypothesis (kinematical, isotropic or the combination of two) can be assumed as parameters the values of which need to be determined in order to achieve the adequacy of simulation results to reality [28]. Tangent modulus needed for the simulation was defined by tensile tests. All material parameters defined by tensile test and parameters used in material model are listed in Table 1.

Time step size control measures can be regarded as common practice in explicit dynamics calculation where very large strains [9] are expected. They can be interpreted as a “safety catch”, activated in order to cope with the elements that lose their physical meaning because of excessive straining [28]. During impact–contact simulation the elements of the material to remove (the chip) are highly deformed and require to decrease the time integration step. The time integration step in explicit integration techniques cannot be greater than the least time duration during which the elastic longitudinal wave passes the smallest element of the structure [28]. As the simulation goes on, the time step tends to become shorter and solution may never end. So, in the presented work, a time step size control technique implemented in LS-DYNA was used as deletion of solid elements too degenerated. The material failure criterion was set as failure strain.

At the initial stage of simulations deformation rate was ignored. Dynamic constants C and P of Cowper–Symonds function were not used during modeling of orthogonal cutting process. Chip separation constitutes one of the most important parts of chip removal process. At the initial stage, the failure strain was set to 0.8 (*similar to the static value obtained from tensile tests*). Some researchers claim that the magnitude of the fracture deformation does not affect simulation results [8]. It was demonstrated that when neglecting deformation rate (*i.e. without artificial enlarging of yield limit*), the maximal achieved value of cutting force is equal to 170 N, which is 3.4 times smaller than the experimental value.

Thus, taking into consideration that in the course of cutting process the material was subjected both to temperature effect and influences arising from high deformation rate, the actual failure strain value maybe be 1.16–1.75 times larger than its static equivalent [29]. Finally, the set of simulations with different failure strain (0.8; 1.0; 1.2; 1.4) were performed. Figures 6a and 6b presents the FE modeling results, assuming failure strain at the initial stage of chip formation.

It was defined, that failure strain influence the shape of chip in the initial cutting stage, the distribution of strain, shear localization and distribution (according to 1st and 2nd shear in cutting zone) and finally cutting force. Failure strain non influences shear formation (this is the case study with 0 rake angle).

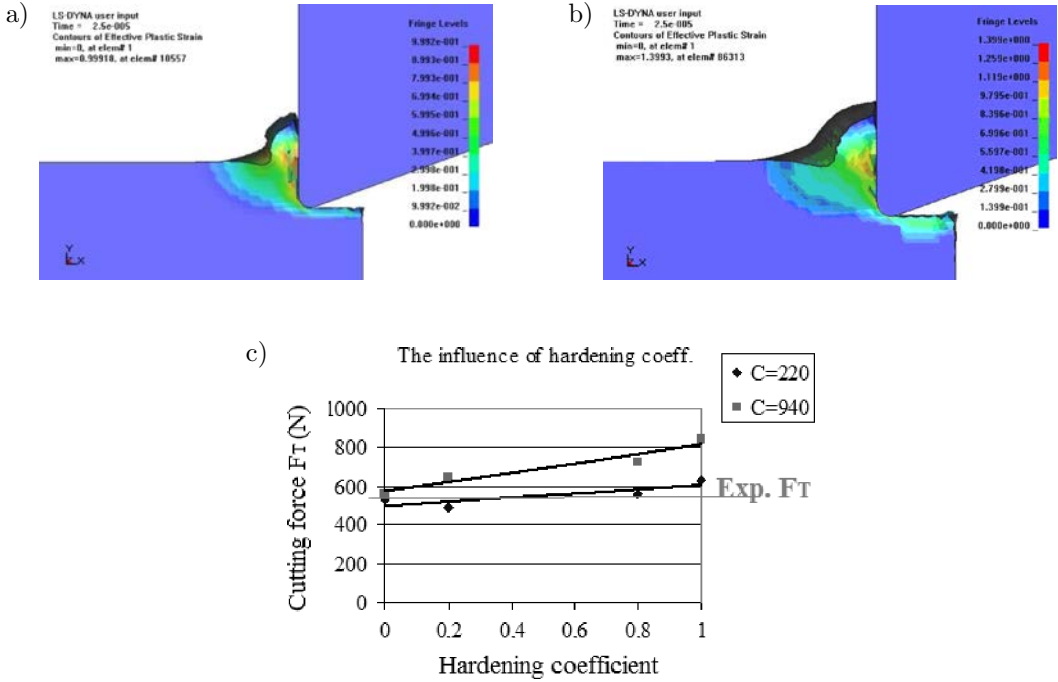


FIG. 6. Chip formation: a) $f_{st}=1.0$, $t = 0.025$ ms; b) $f_{st} = 1.4$, $t = 0.025$ ms.

Figure 6c presents the cutting force variation according to Cowper–Symonds constants and material hardening coefficients ($C = 220 \text{ s}^{-1}$, $P = 5$ and $C = 940 \text{ s}^{-1}$, $P = 3.5$; $f_{st} = 0.8$). The choice of the type of hardening law may influence the results dramatically. Both series of simulations the combination with hardening coefficient which corresponds correctly (2.1%) with experimental results ($F_t = 572 \text{ N}$), when using kinematic hardening with constants $C = 940 \text{ s}^{-1}$, $P = 3.5$. The same results are achieved using kinematic–isotropic hardening ($\beta = 0.8$) with constants $C = 220 \text{ s}^{-1}$, $P = 5$. Consequently, it is here that another precision of chip formation is needed. The chip form, specifically the chip segmentation frequency, is defined from chip geometrical elements and was introduced to the precise FE model.

According to the authors [28], the choice of dynamic constants can not be an “accidental mix”; and here the ambiguity is possible while selecting Cowper–Symonds (C and P) constants. Both of them belong to Cowper–Symonds yield limit scaling model and to some extent are able to compensate each other [28]. For that reason as presented in Fig. 6c more attention is paid to FE model adjustment. It is suggested to check not only one experiment output parameter with numerical results. Figure 7 presents modelling results with extreme material hardening constants.

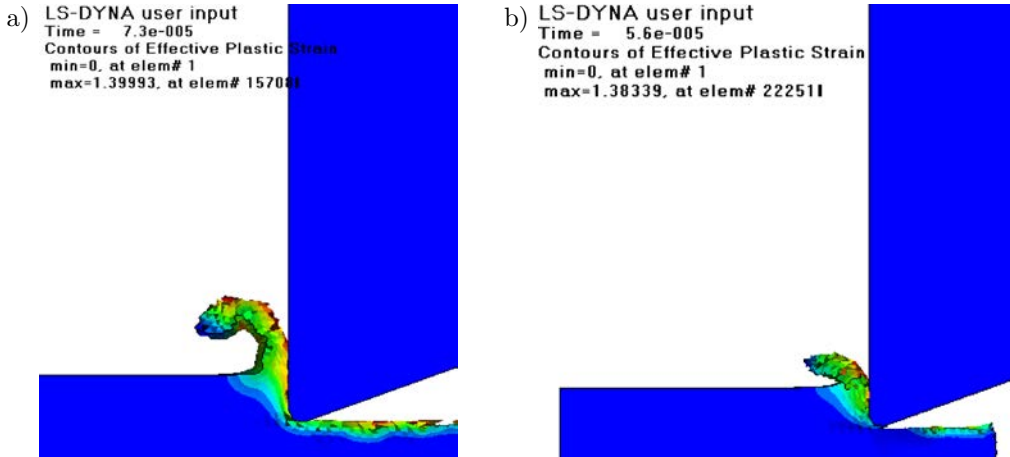


FIG. 7. Chip formation, according to material kinematic and isotropic hardening: a) chip formation with kinematic hardening: continuous chip with formed segments ($C = 220 \text{ s}^{-1}$, $P = 5$, $\beta = 0$, $f_{st} = 1.4$), $F_{t \text{ calc}} = 529 \text{ N}$ (7.6% less experimental value); b) chip formation with isotropic hardening: failure of chip ($C = 220 \text{ s}^{-1}$, $P = 5$, $\beta = 1$, $f_{st} = 1.4$), $F_{t \text{ calc}} = 640 \text{ N}$ (11.8% more experimental value).

Performed orthogonal turning simulations in the range of material kinematic, kinematic–isotropic, isotropic hardening presented chip formation from continuous segmented (or laminar) to chip failure. Idem, cutting force increase going to use kinematic–isotropic and isotropic hardening (Fig. 6c).

Finally, it was tested the set of Cowper–Symonds constants and material hardening constant which matches up to experimental results. Figure 8 presents the results of simulation with material constants: $C = 940 \text{ s}^{-1}$, $P = 3.5$ ($\beta = 0$) and $C = 220 \text{ s}^{-1}$, $P = 5$ ($\beta = 0.8$) and $f_{st} = 1.4$.

As it is presented in Fig. 8a kinematic hardening perform much more regular chip comparing with isotropic material hardening. However, some authors [28], using Cowper–Symonds material behavior law in ballistics proposes to use isotropic hardening if thermal phenomenon appears. The main application of the developed FE model can be the field of high-speed machining (HSM) processes. Because, only 17% of primary heat zone flows into the workpiece [30].

As it was demonstrated the material behavior law, assuming constants, defining deformation rate can't be used only by validation numerical model with only on numerical model output parameter. However, chip form, especially chip segmentation frequency was chosen to validate FE model. It was defined finally, that performed FE model with failure strain 1.4 (kinematic or isotropic hardening) does not match the segmentation frequency of chip (with a difference of least four times). Though it was stated, what Cowper–Symonds material behavior law with kinematic hardening numerically generate perfectly continuous

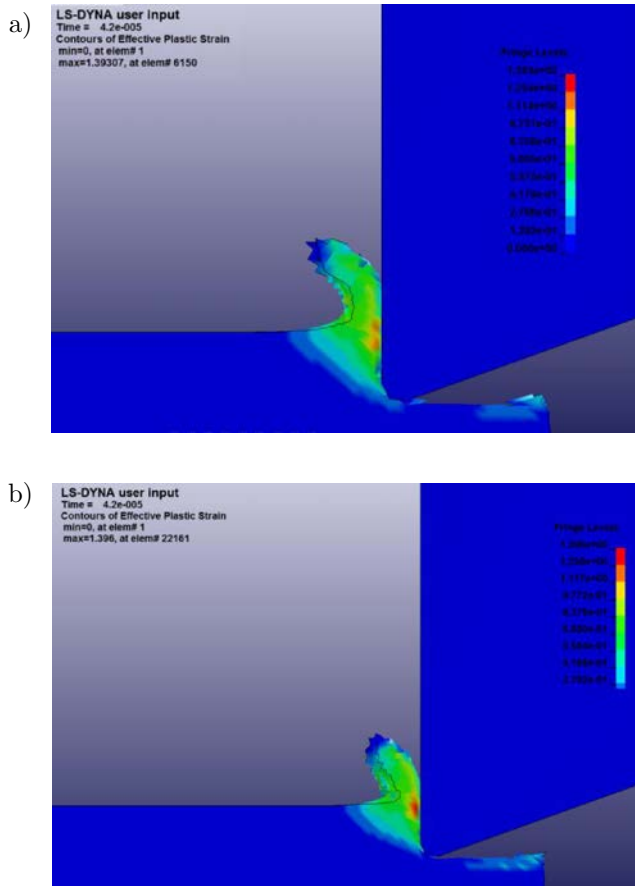


FIG. 8. Chip formation, according to material kinematic and isotropic hardening: a) chip formation with kinematic hardening: continuous chip ($C = 940 \text{ s}^{-1}$, $P = 3.5$, $\beta = 0$, $f_{st} = 1.4$), $F_{t \text{ calc}} = 588 \text{ N}$ (+2.7% experimental value); b) chip formation with kinematic-isotropic hardening: ($C = 220 \text{ s}^{-1}$, $P = 5$, $\beta = 1$, $f_{st} = 1.4$), $F_{t \text{ calc}} = 644 \text{ N}$ (+12% experimental value).

chip. Thus, there it can be stated that the best application of composed FE numerical model can be the generated chip load on cutting tool.

4. CONCLUSIONS AND PERSPECTIVES

The large experimental area of turning tests provided the experimental case (*uniform plastic deformation, no built-up formation, no resonance phenomenon*) for FE modelling of orthogonal cutting process. The analysis presented showed the ambiguity of the use of Cowper–Symonds material behavior law in modelling of cutting process.

First, both isotropic and kinematic material hardening presents “desirable” numerical results, according to the cutting force. Secondly, the final adjustment of numerical model of the cutting process can be done only by checking the chip form generation.

There it can be stated that the best application of composed FE numerical model can be the generated chip load on cutting tool.

Assuming chip form for further FE modelling elastic–plastic material model with kinematic (or kinematic–isotropic) hardening should be proposed.

ACKNOWLEDGMENTS

Research support was provided by Research Council of Lithuania through the project No. MIP–113/2010 (VibroCut).

REFERENCES

1. CHILDS T., MAEKAWA K., OBIKAWA T., YAMANE Y., *Metal machining. Theory and applications*, London, 2000.
2. ZATARAIN M., *Manufacturing technologies: current researching trends*, 5th International Conference on High Speed Machining, pp. 1–38, Metz, France, 2006.
3. XIE J.Q., BAYOUMI A.E., ZBIB H.M., *FEA modeling and simulation of shear localized chip formation in metal cutting*, Int. J. of Machine Tools & Manufacture, **38**, 1067–1087, 1998.
4. RECH J., YEN Y.C., HAMDI H., ALTAN T., BOUZAKIS K.D., *Influence of cutting edge radius of coated tool in orthogonal cutting of alloy steel*, Materials Processing and Design: Modeling, Simulation and Applications – NUMIFORM 2004 – Proceedings of the 8th International Conference on Numerical Methods in Industrial Forming Processes, AIP Conference Proceedings, Volume 712, pp. 1402–1407, 2004.
5. YEN Y.C., JAIN A., ALTAN T., *A finite element analysis of orthogonal machining using different tool edge geometries*, Journal of Materials Processing Technology, **146**, 1, 72–81, 2004.
6. ASTAKHOV V.P., *A treatise on material characterization in the metal cutting process. Part 2: Cutting as the fracture of workpiece material*, J. of Materials Processing Technology, **96**, 34–41, 1999.
7. BOUZAKIS K.D., MICHAILIDIS N., SKORDARIS G., KOMBOGIANNIS S., HADJIYIANNIS S., EFSTATHIOU K., ERKENS G., RAMBADT S., WIRTH I., *Effect of cutting edge radius and its manufacturing procedure, on the milling performance of PVD coated cemented carbide inserts*, Annals of the CIRP, **51**, 61–64, 2002.
8. HAMMAN J.C., GROLLEAU V., LE MAITRE F., *Machinability improvement of steels at high cutting speeds – study of tool/work material interaction*, Annals of the CIRP, **45**, 87–92, 1996.
9. GUO Y.B., *An integral method to determine the mechanical behavior of materials in metal cutting*, J. of Materials Processing Technology, **142**, 72–81, 2003.

10. GUO Y.B., LIU C.R., *Residual stress formation mechanism and its control by sequential cuts*, Transactions of Namri/ASME, **28**, 179–184, 2000.
11. BAKER M., *Finite element investigation of the flow stress dependence of chip formation*, J. of Materials Processing Technology, **167**, 1, 1–13, 2005.
12. ZHANG Y.C., MABROUKI T., NELIAS D., GONG Y.D., *Chip formation in orthogonal cutting considering interface limiting shear stress and damage evolution based on fracture energy approach*, Finite Elem. Anal. Des., **47**, 7, 850–863, 2011.
13. GARCIA ARANDA M.L., *Etude thermo-mécanique et modélisation numérique de l'emboutissage à chaud de l'Usibor 1500* [in French], PhD-Thesis, Ecole des Mines de Paris, 2004.
14. CHIGURUPATI P., JINN J.T., OH J.Y., YIN Y., ZHANG H., WU W.T., *Advances in Machining Process Modeling*, AIP Conference Proceedings, **712**, 2004.
15. HUA J., SHIVRUPI R., CHENG X., BEDEKAR V., MATSUMOTO Y., HASCHIMOTO F., WATKINS T.R., *Effect of feed rate, workpiece hardness and cutting edge on subsurface residual stress in the hard turning of bearing steel using chamfer + hone cutting edge geometry*, Materials Science and Engineering, **394**, 238–248, 2005.
16. ARRAZOLA P.J., DONE U., VILLAR J.A., MARYA S., *Finite element modelling: a qualitative tool to study high speed machining*, 5th International Conference on High Speed Machining, pp. 239–246, Metz, France, 2006.
17. FILONENKO S.N., *Metal cutting* [in Russian], Kiev, 1969.
18. SKIEDRAITE I., KUWAHARA M., FUJI H., *Contact tangential method for measurement of tool geometry* [in Japanese], Patent No 37163310, Japan.
19. SKIEDRAITE I., SLEINIUTE V., *Measurement of tool – edge geometry*, Mechanics, **6**, 50, 64–67, 2004.
20. RACZY A., ALTENHOF W.J., ALPAS A.T., *An Eulerian Finite Element Model of the Metal Cutting Process*, Proceedings of 8th international Ls–Dyna Users conference, 11–25, 2004.
21. BAKER M., ROSLER J., SIEMERS C., *A finite element model of high speed metal cutting with adiabatic shearing*, Computers & Structures, **80**, 495–513, 2002.
22. FALLBOHMER P., RODRIGUEZ C.A., OZEL T., ALTAN T., *High-speed machining of cast iron and alloy steels for die and mould manufacturing*, J. of Materials Processing Technology, **98**, 104–115, 2000.
23. *LS-DYNA Theoretical manual*, Livermore Software Technology Corporation, 1998.
24. SHAW MILTON C., *Metal cutting principles*, Oxford, 1997.
25. GRANOVSKI G.I., GRANOVSKI V.G., *Metal cutting* [in Russian], Moscow, 1985.
26. MOLINARI A., MOUFKI A., *A new thermomechanical model of cutting applied to turning operations. Part 1, Theory*, Int. J. of Machine Tools and Manufacture, **45**, 166–180, 2005.
27. MOUFKI A., *Contribution à la modélisation de l'usinage par une approche thermo viscoplastique. Application la coupe, orthogonale et oblique* [in French], PhD-Thesis, University of Metz, 1998.
28. BARAUSKAS R., ABRAITIENE A., *Computational analysis of impact of a bullet against the multilayer fabrics in LS-DYNA*, International Journal of Impact Engineering, **34**, 1286–1305, 2007.

29. DEY S., BORVIK T., HOPPERSTAD O.S., LANGSETH M., *On the influence of fracture criterion in projectile impact of steel plates*, Computational Materials Science, **38**, 176–191, 2006.
30. ABUKHSHIM N.A., MATIVENGA P.T., SHEIKH M.A., *Heat generation and temperature prediction in metal cutting: A review and implications for high speed machining*, International Journal of Machine Tools and Manufacture, **46**, 7-8, 782–800, 2006.

Received November 15, 2012; revised version November 25, 2013.

Revisiting the Reflected Caustics Method: the Accurate Shape of the “Initial Curve”

Christos F. MARKIDES, Stavros K. KOURKOULIS

*National Technical University of Athens, Department of Mechanics,
Laboratory of Testing and Materials*

5, Heroes of Polytechnion Avenue, 157 73 Zografou Campus, Athens, Greece
e-mail: stakkour@central.ntua.gr

The shape of the “initial curve”, i.e. the locus of material points, which if properly illuminated provide (under specific conditions) the “caustic curve”, is explored. Adopting the method of complex potentials improved formulae for the shape of the “initial curve” are obtained. Application of these formulae for two typical problems, i.e. the mode-I crack and the infinite plate with a finite circular hole under uniaxial tension, indicates that the “initial curve” is in fact not a circular locus. It is either an open curve or a closed contour, respectively, the actual shape of which depends also on the in-plane displacement field.

Key words: reflected caustics, “initial curve”, complex potentials, mode-I crack, stress intensity factor, plate with a circular hole.

1. INTRODUCTION

The experimental method of Caustics was first applied for the solution of Fracture Mechanics problems by Manogg in 1964 for transparent materials in the form of “Transmitted Caustics” [1]. A few years later Theocaris broadened the application field of the method by introducing the theory of “Reflected Caustics” [2]. In this way it became possible to study the stress singularity in an elastic plate, irrespectively of whether the material of the plate is transparent or opaque. Initially the method was applied under the title “Shadow Optical Technique”. It was only in 1971 when Theocaris introduced the term “Method of Caustics” (from the ancient Greek word “καυστική” originating from the verb “καίω” which means “burn”) [3].

The underlying principle of the method is that in case a light beam impinges on a specimen at the immediate vicinity of a singularity the transmitted or reflected rays (received on a reference plane parallel to the specimen’s plane) will concentrate along a strongly illuminated curve (called “caustic curve”) due to

the strong variations of both the thickness and refractive index at the region close to the singularity. It is exactly the shape and dimensions of this illuminated locus that permit quantitative investigation of critical characteristics of the stress field around the singularity, like for example the Stress Intensity Factor (SIF).

Since its introduction, the method of caustics has been used by many researchers, as analytically described by KALTHOFF [4] in his concise review paper. From the very first period of its development the application of the method covered a wide field of static engineering problems ranging from the calculation of SIFs (in either isotropic [5] or anisotropic materials [6]) to the determination of material properties [7, 8] and to the study of contact problems [9] and deformed boundaries [10]. In parallel the method was used to study the behaviour of materials under dynamic loading conditions [11–14]. In the same period ROSAKIS and FREUND [15] applied the method to confront plasticity problems while KIKUCHI and HAMANAKA [16] used caustics for the experimental determination of the J -integral.

Today the method of caustics is still under further development [17, 18] and is widely used to determine the intensity of stress fields around static cracks [17], to study dynamic [18] and impact problems [19], interfacial cracks [20, 21], fatigue [22] and contact problems [23, 24] and recently problems at the nano-scale [25]. Moreover the method is widely applied for the study of anisotropic- [26, 27], transversely isotropic- [28], orthotropic- [29] or even graded- [30] and composite materials [31]. Recently Gdoutos used the method of caustics for quantification of the triaxial effects around crack tips [32]. Finally, it is worth mentioning that Younis introduced applications of the method in engineering education by designing appropriate experiments [33].

Although the method gradually became very popular its application is not yet fully standardized (CARAZO-ALVAREZ and PATTERSON [34] were the first who proposed a standardizing procedure around 1999). Moreover little attention is paid to the quantification of errors and inaccuracies introduced by various factors which can be in general classified into two broad categories related to: (i) the experimental set-up and the specimens and (ii) approximations adopted during the development of the theory and the derivation of the respective formulae.

For the first category THEOCARIS and RAZEM [35], already from 1981, attempted a quantification of the errors due to the screen position and the specimen's thickness. Later ROSSMANITH [36] studied the errors due to irregular specimen thickness. A more systematic approach to the problem was presented by WALLHEAD *et al.* [37] while KONSTA-GDOUTOS and GDOUTOS [38] introduced useful guidelines for the correct application of the method setting also the respective applicability limits.

In the second category the most systematic study was that by ROSAKIS and ZEHNDER [39] who developed the exact mapping equations describing reflected

caustics. They pointed out that if the SIFs are evaluated by caustics according to the approximate analysis the errors could be as large as 15%. The accuracy of the method was also assessed by SPYROPOULOS [40] who pointed out that only the exact expressions of the complex potentials should be employed since in case approximate formulae are used errors slip into the results shadowing the actual phenomena.

In the direction of further improving the accuracy of the method an attempt is here presented to eliminate an additional source of errors related to the “initial curve”. This term designates the geometric locus of the plate’s points which under specific conditions [2, 4] provide the set of reflected rays forming the caustic curve on the screen. The “initial curve” depends on the optical constants of the material and it is not the same for reflections from the rear and the front face of the plate. Moreover it depends on the type of light bundle impinging on the plate (parallel, converging or diverging light rays) as well as on the optical arrangement.

The study is focused to the Reflected Caustics method. Disregarding the discussion about the conditions that must be fulfilled in order for the points of the “initial curve” to provide a caustic curve, attention is paid to the fact that light rays impinge on an already deformed plate. Therefore it appears reasonable to derive the equations of the “initial curve” by considering the deformed state contrary to what is commonly adopted in the classic literature about caustics where the “initial curve” is described ignoring the in-plane deformation (assuming in fact that the magnitude of displacements is negligible with respect to the size of the “initial curve” itself). The approach here described is relieved from this restriction and improved formulae are obtained for the “initial curve”. These formulae are then applied in two configurations widely studied by employing the method of caustics, i.e. (i) the mode-I crack and (ii) the infinite plate with a finite circular hole under uniaxial tension at infinity. The results of the analysis indicate that for stiff materials the classic approach (i.e. considering the “initial curve” a circular locus of points on the undeformed specimen) is quite satisfactory even in the presence of strong singularities like crack tips. On the contrary, in case of materials with increased compliance the discrepancy between the two approaches becomes non-negligible, exceeding even 12%.

2. THE “INITIAL CURVE” ACCORDING TO THE CLASSIC APPROACH [2]

A parallel light beam (planar wave-fronts) impinges normally on a thin plate of thickness t , which is in equilibrium under a system of external in-plane loads F (Fig. 1). Due to lateral deformation of the plate’s initially plane surface the light rays reflected form spherical wave-fronts $S(x, y, z)$ the gradient ∇S of which

that P' is the normal projection of P on the screen. Then according to Snell's law rays impinging on P_p (or on P considering the negligible magnitude of the out of plane deformation at P with respect to the distance Z_o) are reflected at an angle 2ϕ and the vector \mathbf{W} defines the image Q of P on the caustic curve (Fig. 1). It holds that:

$$(2.1) \quad \mathbf{W} = \mathbf{r}_o + \mathbf{w} = \mathbf{r}_o + Z_o \nabla s(x, y).$$

Vector \mathbf{r}_o corresponds to point P while vector $\mathbf{w} = Z_o \nabla s(x, y)$ describes the deviation of light rays on the screen due to the distortion of the plate at point P . Moreover $s(x, y)$ is the path change of the light rays. Furthermore for Eq. (2.1) to be valid self-similarity for the reflected wave-fronts has been assumed (parallel bent fronts rather than the exact spherical ones [39]):

$$(2.2) \quad S(x, y, z) = z + s(x, y) = \mathcal{C}_1,$$

where \mathcal{C}_1 is a constant. Equation (2.2) is valid for small deflection angles ϕ , an assumption well acceptable within the frame of Linear Elasticity. Along the same line of thought it is assumed that:

$$(2.3) \quad s(x, y) \approx \Delta t(x, y) = \frac{\nu t}{E}(\sigma_1 + \sigma_2).$$

In Eq. (2.3) $\Delta t(x, y)$ is the thickness change of the plate (due to the out of plane deformation of the plate) at point P expressed (through Hooke's generalized law) in terms of the principal stresses, σ_1 and σ_2 , Poisson's ratio ν , and Young's modulus E . The sum of the two principal stresses is expressed with the aid of the complex potential $\Phi(z)$ [41] as:

$$(2.4) \quad \sigma_1 + \sigma_2 = 4\Re\Phi(z),$$

\Re denotes the real part and $z = x + iy = re^{i\theta}$ is the complex variable (not to be confused with the z coordinate axis). Then it is readily seen that Eq. (2.1) for the caustic curve can be written in the quite convenient complex form:

$$(2.5) \quad W = z + \underbrace{4Z_o t}_{C} \overbrace{\left(\frac{\nu}{E}\right)^{c_f} \Phi'(z)} = z + C \overline{\Phi'(z)},$$

where $z = r_o e^{i\theta}$ is to be understood as the point P on the "initial curve", prime denotes first order derivative and over-bar the conjugate complex value. Separating real, \Re , from imaginary, \Im , parts, in Eq. (2.5), the parametric equations of the caustic curve are written as:

$$(2.6) \quad W_{x'} = x + C \Re \left\{ \overline{\Phi'(z)} \right\}, \quad W_{y'} = y + C \Im \left\{ \overline{\Phi'(z)} \right\}.$$

In Eq. (2.6) $W_{x'}$, $W_{y'}$ are the horizontal and vertical components of \mathbf{W} on the screen reference (Fig. 1).

The formation of a caustic curve on the screen is the result of a light singularity. Therefore the Jacobian determinant of the transformation of Eqs. (2.6) must be zeroed leading to:

$$(2.7) \quad C |\Phi''(z)| = 1.$$

Double prime denotes second order derivative. According to the classical approach and terminology Eq. (2.7) provides the so-called “initial curve” [2, 4], i.e. the locus of points of the front face of the plate, (ignoring the in-plane deformation of the plate), on which the impinging light rays are reflected forming the caustic curve on the screen.

In case of a non-parallel impinging light beam Eqs. (2.6), (2.7) become:

$$(2.8) \quad W_{x'} = \lambda_m x + C \Re \left\{ \overline{\Phi'(z)} \right\}, \quad W_{y'} = \lambda_m y + C \Im \left\{ \overline{\Phi'(z)} \right\},$$

$$(2.9) \quad C \left| \frac{\Phi''(z)}{\lambda_m} \right| = 1,$$

where λ_m is the magnification ratio of the optical setup equal to $(Z_o \pm Z_i)/Z_i$ for a divergent or convergent impinging light beam, respectively; Z_i is the distance of the focus of the divergent or convergent light beam from the loaded plate [4].

3. THE ACCURATE SHAPE OF THE “INITIAL-” AND CAUSTIC-CURVES

It is seen that according to the above line of thought the “initial curve” is considered as a locus of points P on the in-plane undeformed face of the plate. In fact only the out of plane deformation has been taken into account while the in-plane displacements field induced by the external loading system is assumed negligibly small compared to the size of the “initial curve” itself. Such an assumption is quite acceptable for stiff materials, however it could lead to erroneous results in the case of increased compliance materials for which the magnitude of the displacement components is not ignorable. Thus it appears necessary to discriminate between the deformed and the undeformed state of the plate since the external load causes (in case of plane stress) both out-of-plane as well as in-plane deformations translating any point P of the face of the undeformed plate to a new position P_d and then to P_p . Indeed as it is shown in Fig. 2, neglecting rigid body displacements, point $P(x, y)$ of the undeformed plate, corresponding to vector \mathbf{r}_o , shifts to $P_d(x_d, y_d)$ due to the in-plane deformation of the plate through the $\{u, v\}$ displacements (green line in Fig. 2).

Therefore Eq. (2.1) of the classic approach is modified to:

$$(3.2) \quad \mathbf{W} = \mathbf{r} + \mathbf{w} = (\mathbf{r}_o + \mathbf{u}) + Z_o \nabla s(x_d, y_d), \quad \mathbf{u} = u(x, y)\mathbf{i} + v(x, y)\mathbf{j},$$

where u and v are the horizontal and vertical components of the displacement at $P(x, y)$ (Fig. 2), vector \mathbf{r} corresponds to point $P_d(x_d, y_d)$ and $\mathbf{w} = Z_o \nabla s(x_d, x_d)$, $\nabla = \frac{\partial}{\partial x_d}\mathbf{i} + \frac{\partial}{\partial y_d}\mathbf{j}$. In addition $s(x_d, y_d)$ is the change of the path of light rays in the space between points P_d of the in-plane deformed face of the plate and the reference screen. Assuming again self-similar reflected wave-fronts instead of Eq. (2.2) one should now write:

$$(3.3) \quad S(x_d, y_d, z) = z + s(x_d, y_d) = \mathcal{C}_2,$$

where \mathcal{C}_2 is again a constant. Accordingly Eq. (2.3) is rewritten as:

$$(3.4) \quad s(x_d, y_d) \approx \Delta t(x, y) = \frac{\nu t}{E}(\sigma_1 + \sigma_2).$$

Eq. (3.4) differs from Eq. (2.3) in that $s(x, y)$ was substituted by $s(x_d, y_d)$. This substitution is always feasible assuming that s depends only on the out-of-plane deformation Δt . Therefore Δt may equally well be superimposed either to P (undeformed state – classic approach) or to P_d (deformed state – present approach), according to any succession, as long as the principle of superposition is valid. Introducing Eq. (3.4) in $\mathbf{w} = Z_o \nabla s(x_d, x_d)$, leads to:

$$(3.5) \quad \mathbf{w} = Z_o \left[\frac{\partial \Delta t(x, y)}{\partial x_d} \mathbf{i} + \frac{\partial \Delta t(x, y)}{\partial y_d} \mathbf{j} \right] \\ = Z_o \left[\frac{\partial \Delta t(x, y)}{\partial x} \frac{\partial x}{\partial x_d} \mathbf{i} + \frac{\partial \Delta t(x, y)}{\partial y} \frac{\partial y}{\partial y_d} \mathbf{j} \right].$$

For relatively small deformations and taking into consideration Eqs. (3.1) it follows that:

$$(3.6) \quad \frac{\partial x_d}{\partial x} = \frac{\partial [x + u(x, y)]}{\partial x} = 1 + \frac{\partial u(x, y)}{\partial x} \approx 1, \\ \frac{\partial y_d}{\partial y} = \frac{\partial [y + v(x, y)]}{\partial y} = 1 + \frac{\partial v(x, y)}{\partial y} \approx 1.$$

Therefore Eq. (3.5) is reduced to:

$$(3.7) \quad \mathbf{w} = Z_o \left[\frac{\partial \Delta t(x, y)}{\partial x} \mathbf{i} + \frac{\partial \Delta t(x, y)}{\partial y} \mathbf{j} \right]$$

which is found to be identical to the respective formula obtained for \mathbf{w} according to the classic approach. In turn Eq. (2.5) is now written as:

$$(3.8) \quad W = z + u + iv + C\overline{\Phi'(z)}$$

while the parametric equations of the caustic curve (Eqs. (2.6) of Sec. 2) become:

$$(3.9) \quad \begin{aligned} W_{x'} &= x_d + C\Re\left\{\overline{\Phi'(z)}\right\} = x + u + C\Re\left\{\overline{\Phi'(z)}\right\}, \\ W_{y'} &= y_d + C\Im\left\{\overline{\Phi'(z)}\right\} = y + v + C\Im\left\{\overline{\Phi'(z)}\right\}. \end{aligned}$$

Again, as in Sec. 2 the Jacobian of the transformation between the plate (considered now under in-plane deformation also) and the screen must be zeroed. In other words:

$$(3.10) \quad J = \begin{vmatrix} \frac{\partial W_{x'}}{\partial x_d} & \frac{\partial W_{x'}}{\partial y_d} \\ \frac{\partial W_{y'}}{\partial x_d} & \frac{\partial W_{y'}}{\partial y_d} \end{vmatrix} = 0.$$

Due to the Cauchy-Riemann conditions, it holds that:

$$(3.11) \quad \Re\left\{\overline{\Phi'(z)}\right\} = \frac{\partial\Re\{\Phi(z)\}}{\partial x}, \quad \Im\left\{\overline{\Phi'(z)}\right\} = \frac{\partial\Re\{\Phi(z)\}}{\partial y}$$

and taking into account Eqs. (3.6), the Jacobian's elements become:

$$(3.12) \quad \begin{aligned} \frac{\partial W_{x'}}{\partial x_d} &= 1 + C \frac{\partial\Re\left\{\overline{\Phi'(z)}\right\}}{\partial x_d} = 1 + C \frac{\partial^2\Re\{\Phi(z)\}}{\partial x^2} \frac{\partial x}{\partial x_d} = 1 + C \frac{\partial^2\Re\{\Phi(z)\}}{\partial x^2}, \\ \frac{\partial W_{x'}}{\partial y_d} &= C \frac{\partial\Re\left\{\overline{\Phi'(z)}\right\}}{\partial y_d} = C \frac{\partial^2\Re\{\Phi(z)\}}{\partial x\partial y} \frac{\partial y}{\partial y_d} = C \frac{\partial^2\Re\{\Phi(z)\}}{\partial x\partial y}, \\ \frac{\partial W_{y'}}{\partial x_d} &= C \frac{\partial\Im\left\{\overline{\Phi'(z)}\right\}}{\partial x_d} = C \frac{\partial^2\Re\{\Phi(z)\}}{\partial y\partial x} \frac{\partial x}{\partial x_d} = C \frac{\partial^2\Re\{\Phi(z)\}}{\partial x\partial y}, \\ \frac{\partial W_{y'}}{\partial y_d} &= 1 + C \frac{\partial\Im\left\{\overline{\Phi'(z)}\right\}}{\partial y_d} = 1 + C \frac{\partial^2\Re\{\Phi(z)\}}{\partial y^2} \frac{\partial y}{\partial y_d} = 1 + C \frac{\partial^2\Re\{\Phi(z)\}}{\partial y^2}, \end{aligned}$$

whence

$$(3.13) \quad C|\Phi''(z)| = 1.$$

At this point it is worth mentioning that Eq. (3.13) is identical to Eq. (2.7), as a direct consequence of Eqs. (3.6) holding for the relatively small deformations considered here. However there is a critical difference between the two approaches lying in the fact that according to the classic one Eq. (2.7) is the “initial curve” itself while according to the present one Eq. (2.7) or Eq. (3.13) describes the locus of points z (or P) on the undeformed plate to which one should add the respective displacements $\{u, v\}$ in order to obtain the actual “initial curve” (in the sense that the later lies on the deformed face of the plate rather than on the undeformed one).

In case of a divergent or convergent light beam, i.e. for $\lambda_m \neq 1$, Eqs. (3.9), (3.13) become:

$$(3.14) \quad W_{x'} = \lambda_m x_d + C\Re \left\{ \overline{\Phi'(z)} \right\} = \lambda_m(x + u) + C\Re \left\{ \overline{\Phi'(z)} \right\},$$

$$W_{y'} = \lambda_m y_d + C\Im \left\{ \overline{\Phi'(z)} \right\} = \lambda_m(y + v) + C\Im \left\{ \overline{\Phi'(z)} \right\},$$

$$(3.15) \quad C \left| \frac{\Phi''(z)}{\lambda_m} \right| = 1.$$

Again Eq. (3.15) is identical to Eq. (2.9) while Eqs. (3.14) represent the improved version of Eqs. (2.8) of the classic approach.

4. APPLICATIONS

Two typical problems, widely studied by employing the method of Reflected Caustics, are here revisited in order to reveal the main features of the present approach and also to quantify the difference from the classic approach:

- (i) The mode-I crack.
- (ii) The infinite plate with a circular hole under tension.

4.1. The mode-I crack

The configuration of the problem and the optical setup in case of parallel light impinging normally to the plate ($\lambda_m = 1$) are shown in Fig. 3. The initial (undeformed) crack (thin lines) of length 2α opens symmetrically with respect to its axis due to the uniaxial tension σ_o at infinity. The origin of the coordinate axes is the crack tip. The complex potentials for the singular solution are [41]:

$$(4.1) \quad \left. \begin{matrix} \Phi(z) \\ \Omega(z) \end{matrix} \right\} = \frac{\sigma_o}{2} \left(\sqrt{\frac{\alpha}{2z} \mp \frac{1}{2}} \right), \quad \left. \begin{matrix} \varphi(z) \\ \omega(z) \end{matrix} \right\} = \frac{\sigma_o}{2} \left(\sqrt{2\alpha z} \mp \frac{\alpha + z}{2} \right),$$

whence

$$(4.2) \quad |\Phi''(z)| = \frac{3\sigma_o}{8} \sqrt{\frac{\alpha}{2}} \frac{1}{r^{5/2}}.$$

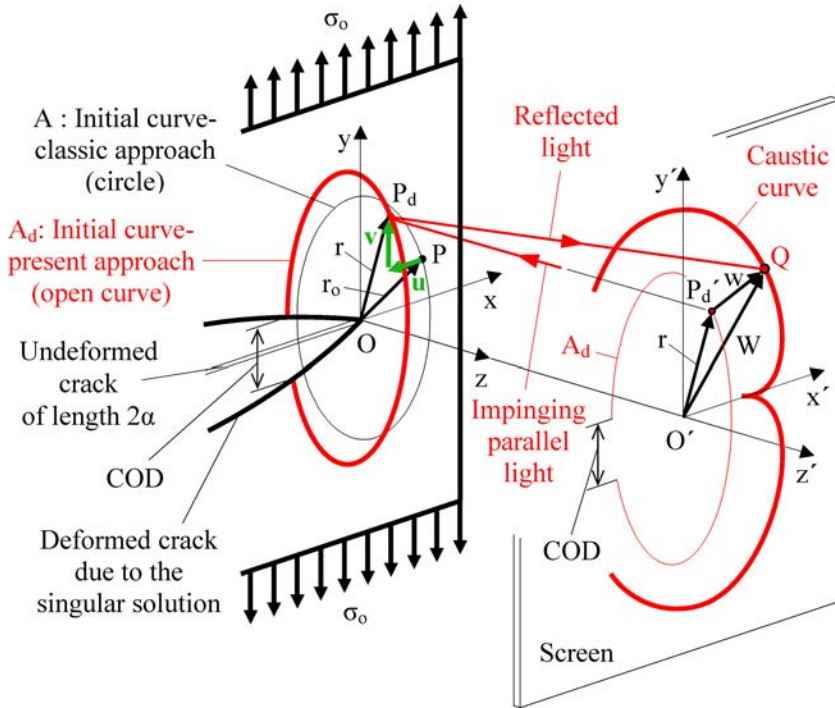


FIG. 3. Reflected caustic curve due to a crack tip according to the present approach.

The deformed (opened) lips of the crack, due to the singular solution, are shown with a bold line in Fig. 3. According to the classic approach points $P(x, y)$ (or in complex form $z = r_0 e^{i\vartheta}$) of the undeformed plate forming the “initial curve” are obtained through Eq. (2.9) as:

$$(4.3) \quad r_0 = \left(\frac{3C\sigma_0}{8|\lambda_m|} \sqrt{\frac{\alpha}{2}} \right)^{2/5}.$$

Clearly due to Eq. (4.3) the “initial curve” is a (closed) circle denoted by A (thin line) in Fig. 3 (Fig. 3 refers to the case with $\lambda_m = 1$). According to the present approach in order to obtain the actual “initial curve” the displacement field of points P (on A) have to be added to the circle A . Taking advantage of the well-known formula [41]:

$$(4.4) \quad 2\mu(u + iv) = \kappa\phi(z) - \omega(\bar{z}) - (z - \bar{z})\overline{\Phi(z)},$$

(κ is Muskhelishvili’s constant and μ the shear modulus of the plate’s material) one obtains with the aid of Eqs. (4.1) the components of the displacement of points P (or $z = r_0 e^{i\vartheta}$) on A as:

$$\begin{aligned}
 (4.5) \quad u &= \frac{\sigma_o}{2\mu} \left[(\kappa - 1) \sqrt{\frac{\alpha r_o}{2}} \cos \frac{\vartheta}{2} - \frac{\kappa + 1}{4} (\alpha + r \cos \vartheta) \right. \\
 &\quad \left. - \frac{1}{2} \sqrt{\frac{\alpha r_o}{2}} \left(\cos \frac{3\vartheta}{2} - \cos \frac{\vartheta}{2} \right) \right], \\
 v &= \frac{\sigma_o}{2\mu} \left[(\kappa + 1) \sqrt{\frac{\alpha r_o}{2}} \sin \frac{\vartheta}{2} - \frac{\kappa - 1}{4} r \sin \vartheta \right. \\
 &\quad \left. - \frac{1}{2} \sqrt{\frac{\alpha r_o}{2}} \left(\sin \frac{3\vartheta}{2} + \sin \frac{\vartheta}{2} \right) \right].
 \end{aligned}$$

Then by adding the above u and v (green line in Fig. 3) to points P of Eq. (4.3) on A one obtains points P_d on the actual, according to the present approach, “initial curve” A_d of varying radius r . As it is shown in Fig. 3, the “initial curve” A_d (red bold line), referred to the deformed plate, is not a closed circle but an elliptic not closed curve due to the crack opening displacement. In Fig. 3 also the projection of A_d on the screen has been drawn (red thin line). Moreover according to the classic approach the parametric equations of the caustic curve are obtained through Eqs. (2.8) (for $\lambda_m \neq 1$) as follows:

$$(4.6) \quad W_{x'} = \lambda_m r_o \left(\cos \vartheta - \frac{2}{3} \cos \frac{3\vartheta}{2} \right), \quad W_{y'} = \lambda_m r_o \left(\sin \vartheta - \frac{2}{3} \sin \frac{3\vartheta}{2} \right),$$

while according to the present approach Eqs. (3.14) in combination with Eqs. (4.5) yield the parametric equations for point Q on the caustic curve (red bold line on the screen Fig. 3) as:

$$\begin{aligned}
 (4.7) \quad W_{x'} &= \lambda_m r_o \left\{ \left(\cos \vartheta - \frac{2}{3} \cos \frac{3\vartheta}{2} \right) + \frac{\sigma_o}{2\mu} \left[(\kappa - 1) \sqrt{\frac{\alpha}{2r_o}} \cos \frac{\vartheta}{2} \right. \right. \\
 &\quad \left. \left. - \frac{\kappa + 1}{4} \left(\frac{\alpha}{r_o} + \cos \vartheta \right) - \frac{1}{2} \sqrt{\frac{\alpha}{2r_o}} \left(\cos \frac{3\vartheta}{2} - \cos \frac{\vartheta}{2} \right) \right] \right\}, \\
 W_{y'} &= \lambda_m r_o \left\{ \left(\sin \vartheta - \frac{2}{3} \sin \frac{3\vartheta}{2} \right) + \frac{\sigma_o}{2\mu} \left[(\kappa + 1) \sqrt{\frac{\alpha}{2r_o}} \sin \frac{\vartheta}{2} \right. \right. \\
 &\quad \left. \left. - \frac{\kappa - 1}{4} \sin \vartheta - \frac{1}{2} \sqrt{\frac{\alpha}{2r_o}} \left(\sin \frac{3\vartheta}{2} + \sin \frac{\vartheta}{2} \right) \right] \right\}.
 \end{aligned}$$

The “initial curves” obtained according to the two approaches considered (the classic and the present one) are plotted in juxtaposition in Fig. 4. Dotted line corresponds to the circular “initial curve” of the classic approach while the continuous one to the improved version. For plotting Fig. 4 plane stress conditions were assumed for a rectangular centrally cracked plate (made from PCBA with Young’s modulus $E = 2.5$ GPa and Poisson’s ratio $\nu = 0.38$) of

length $\ell = 0.10$ m, thickness $t = 2$ mm, and half crack length $\alpha = 0.01$ m. The plate is subjected to a tensile stress at infinity equal to one fifth of the yield stress acting normally to the crack axis. The magnification factor λ_m was set equal to 4. As it is seen from Fig. 4 the improved version of the “initial curve” is slightly displaced inwards, with respect to the crack tip, without being self-similar with the approximate one. Moreover it is discontinuous since the initial crack is no longer a mathematic line, but rather it’s two lips are at a finite distance from each other and equal to the crack opening displacement at the point where the “initial curve” intersects the crack boundaries. Although the differences are rather small from a quantitative point of view they significantly change the data obtained from the respective caustic curves.

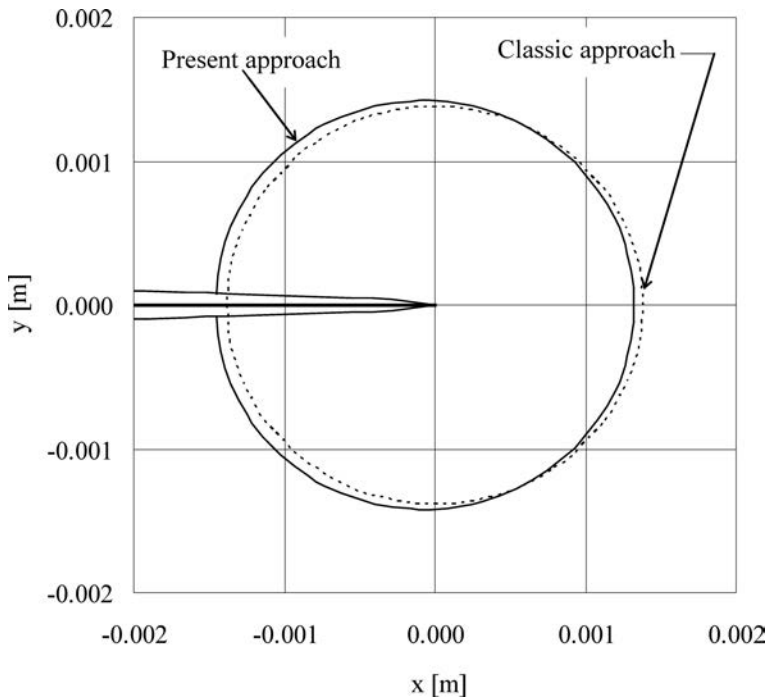


FIG. 4. The “initial curve” in case of the two approaches considered. Dotted line represents the approximate circular “initial curve” (classic approach) while the continuous line corresponds to the exact shape according to the present approach.

For the above statement to be verified, the two caustic curves obtained from Eqs. (4.6) and (4.7) (for the same numerical data as previously), are plotted in Fig. 5. It is seen that the caustic curve obtained from the accurate “initial curve” encompasses that obtained from the classic circular “initial curve” for the major $[-\pi, \pi]$ region. For the differences to be quantified the distance between the two tangents to the caustic curve parallel to the crack axis are compared in

Fig. 5. This distance is usually denoted as D_1^{\min} . As it can be seen from Fig. 5 the distance $D_{1,P}^{\min}$ obtained from the present approach exceeds $D_{1,C}^{\min}$ of the classic approach, by about 5.5%. Taking into account the proof by Theocaris and Pazis [42] (based on the general theory of epicycloid curves), that D_1^{\min} is directly related to the stress intensity factor through the formulae [42]:

$$(4.8) \quad K_I \sim \sqrt[2]{(D_1^{\min})^5}$$

it is easily concluded that the mode-I stress intensity factors K_I calculated according to the two approaches differ by more than 12%.

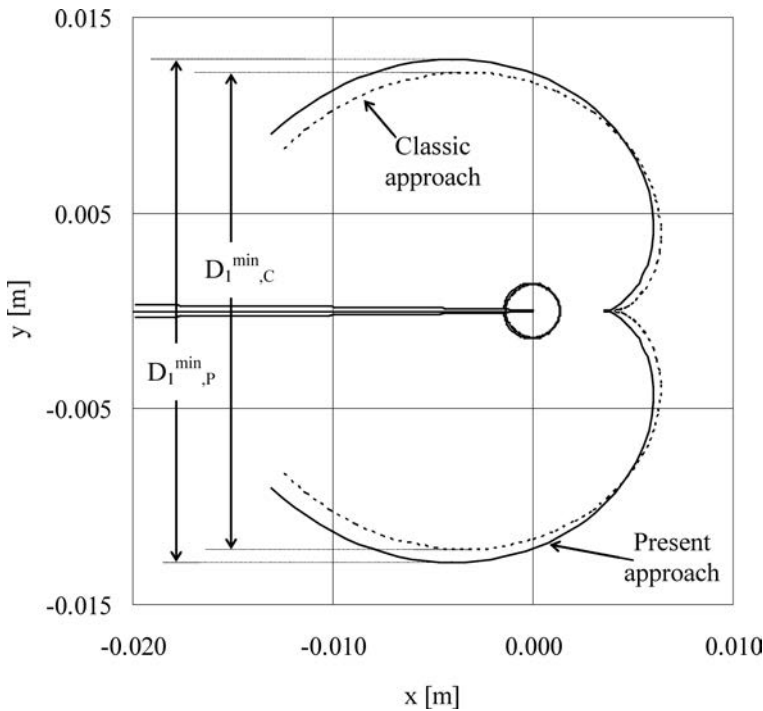


FIG. 5. The caustic curves, dotted and continuous lines, in case of a strong singularity (crack tip) as obtained from light rays reflected on the approximate and on the exact) “initial curves”, respectively.

4.2. *The infinite plate with a finite circular hole under uniaxial tension at infinity*

The configuration of the problem and the optical setup in case of parallel light impinging normally to the plate ($\lambda_m = 1$) are shown in Fig. 6. The initial (undeformed) hole (thin line) of radius R deforms to an ellipse (bold line) due to the uniaxial tension σ_o at infinity. The origin of the coordinate system is

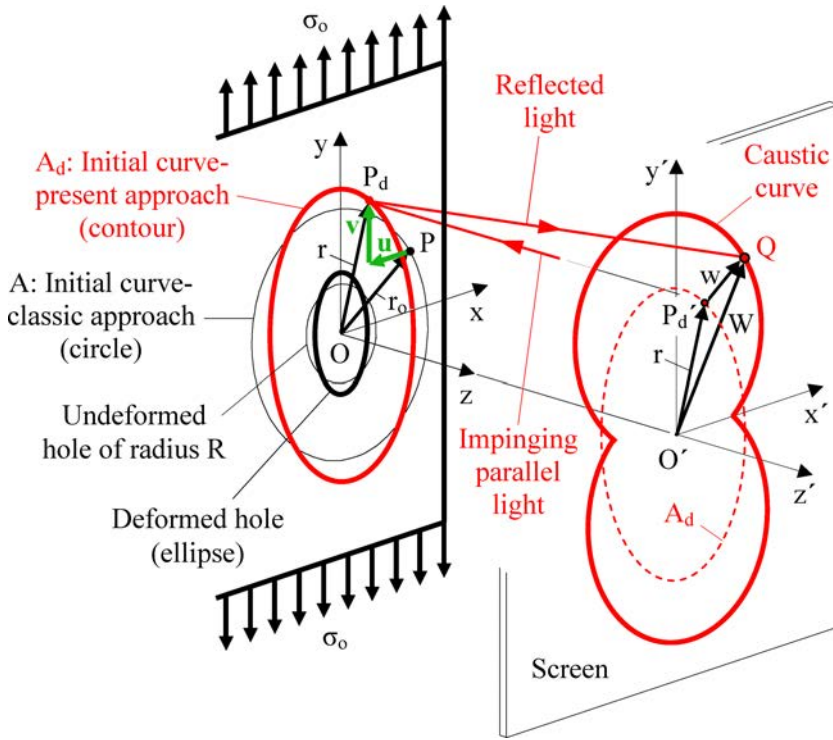


FIG. 6. Reflected caustic curve due to a circular hole according to the present approach.

the centre of the hole. The complex potentials required for the solution of the problem are [41]:

$$\begin{aligned}
 \Phi(z) &= \frac{\sigma_o}{4} \left(1 + \frac{2R^2}{z^2} \right), & \varphi(z) &= \frac{\sigma_o}{4} \left(z - \frac{2R^2}{z} \right), \\
 \psi(z) &= \frac{\sigma_o}{2} \left(z - \frac{R^2}{z} - \frac{R^4}{z^3} \right),
 \end{aligned}
 \tag{4.9}$$

whence

$$|\Phi''(z)| = \frac{3\sigma_o R^2}{r^4}.
 \tag{4.10}$$

Again according to the classic approach points $P(x, y)$ (or $z = r_o e^{i\theta}$) of the undeformed plate forming the “initial curve” are obtained through Eq. (2.9) as:

$$r_o = \left(\frac{3C\sigma_o R^2}{|\lambda_m|} \right)^{1/4}
 \tag{4.11}$$

Eq. (4.11) is in fact the equation of a circle, denoted by A (thin line) in Fig. 6 (Fig. 6 refers to the case $\lambda_m = 1$). On the contrary according to the present approach the actual “initial curve” follows from A by adding the displacement field of points P (on A).

In this direction, employing Muskhelishvili’s formula [41]:

$$(4.12) \quad 2\mu(u + iv) = \kappa\varphi(z) - z\overline{\varphi'(z)} - \overline{\psi(z)}$$

in combination with Eqs. (4.9) one obtains the components of displacement of points P (or $z = r_o e^{i\vartheta}$) on A as:

$$(4.13) \quad \begin{aligned} u &= \frac{\sigma_o}{8\mu r_o} \left\{ [\kappa(r_o^2 - 2R^2) + 2R^2 - 3r_o^2] \cos \vartheta - \frac{2R^2(r_o^2 - R^2)}{r_o^2} \cos 3\vartheta \right\}, \\ v &= \frac{\sigma_o}{8\mu r_o} \left\{ [\kappa(r_o^2 + 2R^2) + 2R^2 + r_o^2] \sin \vartheta - \frac{2R^2(r_o^2 - R^2)}{r_o^2} \sin 3\vartheta \right\}. \end{aligned}$$

Adding u and v (green line in Fig. 6) from Eqs. (4.13) to points P of Eq. (4.11) one obtains points P_d on the actual, according to the present approach, “initial curve” A_d (red bold line in Fig. 6) of varying radius r . In Fig. 6 also the projection of A_d on the screen has been drawn (red dotted line).

Moreover according to the classic approach the parametric equations of the caustic curve are obtained through Eqs. (2.8) as:

$$(4.14) \quad W_{x'} = \lambda_m r_o \left(\cos \vartheta - \frac{1}{3} \cos 3\vartheta \right), \quad W_{y'} = \lambda_m r_o \left(\sin \vartheta - \frac{1}{3} \sin 3\vartheta \right).$$

On the contrary according to the present approach Eqs. (3.14) in combination with Eqs. (4.13) yield the parametric equations for point Q on the caustic curve (red bold line on the screen Fig. 6) as:

$$(4.15) \quad \begin{aligned} W_{x'} &= \lambda_m r_o \left\{ \left(\cos \vartheta - \frac{1}{3} \cos 3\vartheta \right) \right. \\ &\quad \left. + \frac{\sigma_o}{8\mu} \left\{ \left[\kappa \left(1 - \frac{2R^2}{r_o^2} \right) + \frac{2R^2}{r_o^2} - 3 \right] \cos \vartheta - \frac{2R^2(r_o^2 - R^2)}{r_o^4} \cos 3\vartheta \right\} \right\}, \\ W_{y'} &= \lambda_m r_o \left\{ \left(\sin \vartheta - \frac{1}{3} \sin 3\vartheta \right) \right. \\ &\quad \left. + \frac{\sigma_o}{8\mu} \left\{ \left[\kappa \left(1 + \frac{2R^2}{r_o^2} \right) + \frac{2R^2}{r_o^2} + 1 \right] \sin \vartheta - \frac{2R^2(r_o^2 - R^2)}{r_o^4} \sin 3\vartheta \right\} \right\}. \end{aligned}$$

Considering again a PCBA plate of the same as previously dimensions and mechanical properties with a central circular hole of radius $R = 0.01$ m one

can plot the caustic curves due to the classic (Eqs. (4.14)) and the present (Eqs. (4.15)) approaches as it is seen in Fig. 7 (only one quarter of the plate is plotted for double symmetry reasons). Obviously the differences are less striking given that the singularity is now weaker (compared to the crack tip). However even in this case there is an increase of the maximum transverse dimension of the caustic (denote as D_m in Fig. 7) equal to about 2.5%.

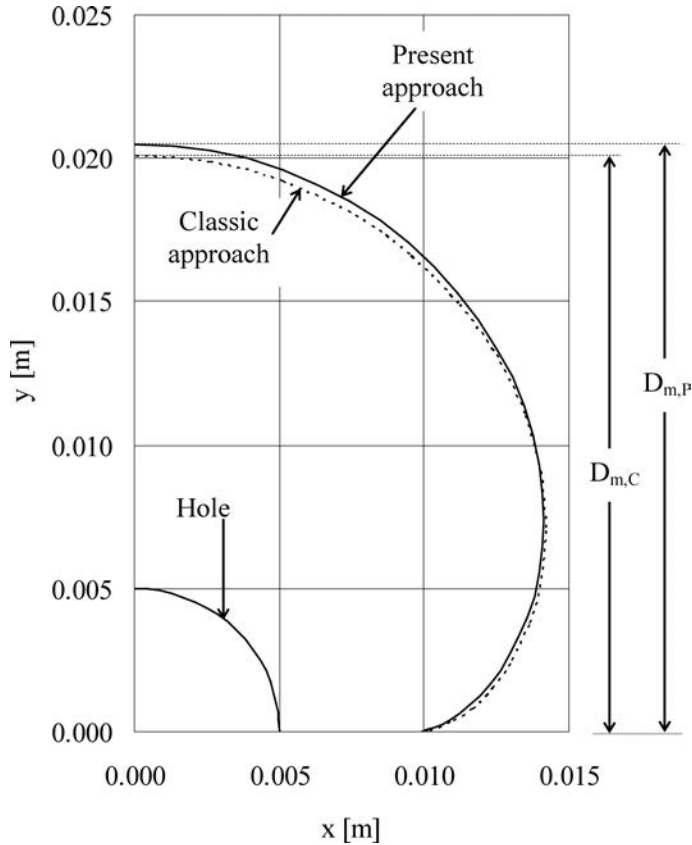


FIG. 7. The caustic curves, dotted and continuous lines, in case of a weak singularity (circular hole) as obtained from light rays reflected on the approximate and the exact “initial curves”, respectively.

Recalling the familiar formula [43]:

$$(4.16) \quad \sigma_o \sim D_m^4$$

which relates the stress induced at infinity σ_o to the characteristic dimension of the caustic, differences of the order of 10% are obtained for σ_o if it is calculated according to the two approaches here considered.

5. DISCUSSION AND CONCLUSIONS

The experimental method of caustics, either transmitted or reflected, is considered nowadays a useful and flexible tool for the exploration of specific features of the stress field around singularities due to its sensitivity to deformation gradients. Despite the fact that the method was introduced almost fifty years ago, it is not yet standardized and a few questions are still open concerning its natural foundation, the optimum procedure for its application, as well as the assessment of the experimental results. Despite these open questions the method is nowadays widely used in various modern fields of experimental strength of materials (as it was mentioned in the introductory section) covering both mechanical- (i.e. roller bearing contact [44]) and civil-engineering applications (i.e. behaviour of rocks under impact [45]).

The present study was devoted to the determination of the accurate shape of the “initial curve” without falling back on the assumption that the deformation field is negligible compared to the size of the “initial curve”. The importance of the correct determination of the “initial curve” is better understood taking into account that all points of the “initial curve” are mapped onto the caustic curve while all points inside and outside this curve are mapped outside the caustic. Considering that the light rays forming the caustic curve originate exclusively from the “initial curve”, it is understood that all information gathered from the caustic curve depends exclusively on the respective “initial curve”. The significance of the “initial curve” is further accentuated considering that by varying Z_o (changing for example the focal plane of the recording system), the position of the “initial curve” varies accordingly, permitting a scanning of the near-tip region enlightening critical features of the stress field surrounding the singularity.

In this direction closed-form formulae for the actual shape of the “initial curve” were deduced. Taking advantage of these formulae the caustic curves formed by light rays reflected at the points of the actual “initial curve” were drawn and compared with the respective ones corresponding to a circular “initial curve” on the undeformed plate. Both qualitative and quantitative differences between the two approaches (the approximate classic one and the more accurate one proposed here) were detected which are essentially independent from both the kind of light bundle impinging on the plate (parallel, converging or diverging light rays) and also from the experimental setup. From a quantitative point of view the importance of these differences depends on the nature of the specimen’s material. In fact for brittle and relatively stiff materials like PMMA the differences quantified between the two approaches are either negligible (for weak singularities like the circular hole) or they fall well within experimental error (i.e. less than 4%) for strong singularities (like the crack tip). On the contrary for less stiff materials like PCBA the differences are of the order of 10% or even

higher for both weak and strong singularities. Obviously differences of the order here detected should not be ignored for either weak or strong singularities.

A quantitative overview of this point is gained from Fig. 8 where the percentage difference between the classic and the present approaches is plotted versus the elastic modulus of a wide class of real materials ranging from stiff ones (a type of soft rock) to materials with increased compliance (PTFE). Both the cases of weak (hole in an infinite plate) and strong (mode-I crack) singularities are described. For comparison reasons in the case of a weak singularity the load induced was equal to one third of the respective yield stress while for the strong singularity the stress at infinity was one fifth of the respective yield one. Both the raw data (characteristic dimension of the caustic curve) and the quantities obtained from these data (mode-I stress intensity factor K_I and stress at infinity σ_o) are plotted in Fig. 8, clearly supporting the conclusions drawn in the previous paragraphs.

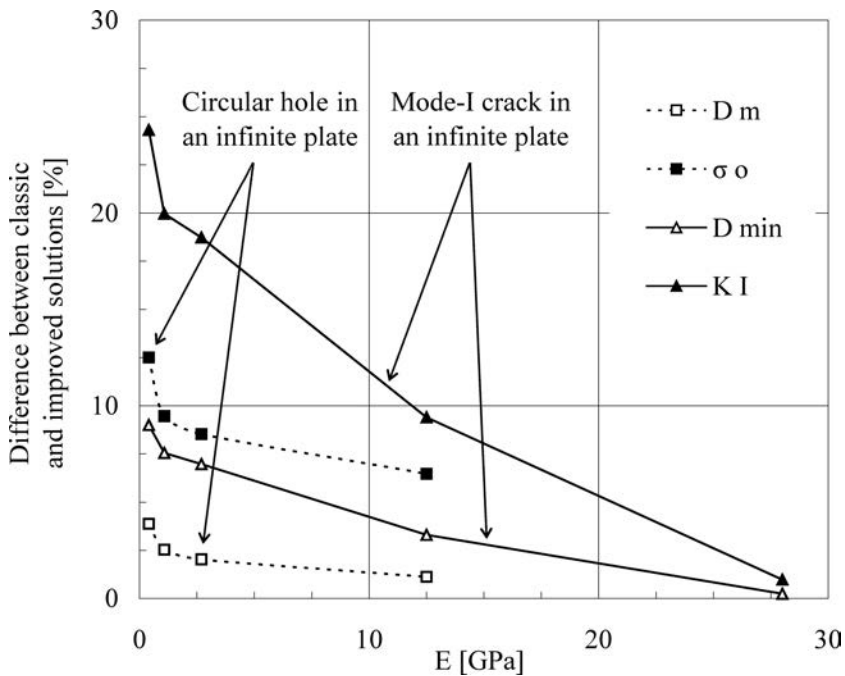


FIG. 8. The difference between the two approaches versus the elastic modulus of the specimens' material. Triangular symbols correspond to the strong singularity while the rectangular ones to the weak singularity. Empty symbols represent the raw data obtained directly from the caustic while the filled ones correspond to the indirectly calculated quantities.

Before concluding it is once again emphasized that the approach introduced here assumes relatively small deformations, as it is in the case of the classic approach. The difference lies in that the classic approach ignores both the gra-

dients of the in-plane displacements and the in-plane displacements themselves. On the contrary, in the present approach only the gradients of the displacement field were ignored while the displacements themselves were taken into account. This could be proved very beneficial in specific applications such as for example, the determination of the contact length in case of two elastic bodies in contact using the method of reflected caustics. In such a case where the quantity to be determined (contact length) is well comparable to the dimensions of the displacement field's components it is obvious that ignoring the displacement components themselves is erroneous. The specific problem for the case of two elastic discs (radius $R = 50$ mm and thickness $t = 10$ mm) made of PMMA and compressed against each other along a common generatrix of their external surfaces was recently solved analytically [46] according to the improved approach introduced in Sec. 4. Characteristic results of this analysis are shown in Fig. 9, where the

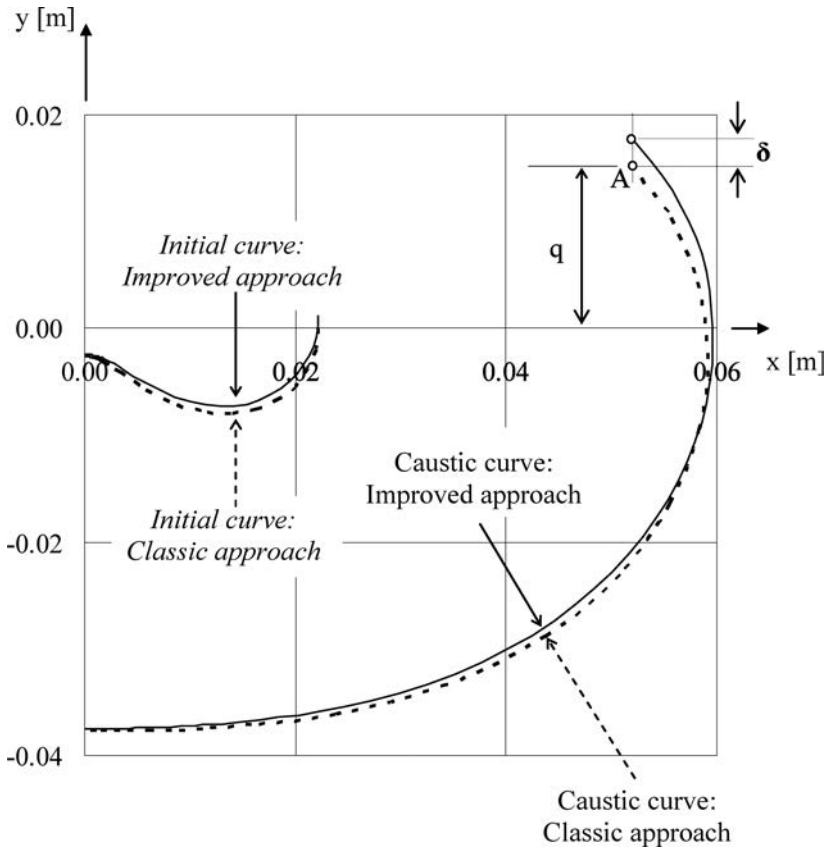


FIG. 9. The “initial curves” and the respective caustics obtained from the contact area of two discs compressed against each other along a common generatrix of their external surface. Dotted lines represent the classic formulation while the continuous ones correspond to the present approach.

“initial curves” and the respective contact caustics are plotted according to both the classic and the improved approaches. According to the theoretical analysis described in detail in ref. [46] the “elevation” q of the end-points A of the caustic curve is directly related to the length of the contact arc developed between the two discs. As it can be seen from Fig. 9, the difference δ of the elevation determined by employing the classic and the improved approaches of the reflected caustics method exceeds 15%. Obviously in case the discs were made from a less stiff material (like for example PTFE or PCBA) the difference would become higher rendering the results of the classic approach unreliable.

ACKNOWLEDGMENT

The authors express their sincere gratitude to Professor D.N. Pazis of the Department of Mechanics of the National Technical University of Athens. His deep knowledge on the founding principles of the method of caustics and his unique experience on its laboratory application were unsparingly offered and greatly contributed to the final outcome of the present research.

REFERENCES

1. MANOGG P., *Schattenoptische Messung der spezifischen Bruchenergie waehrend des Bruchvorgangs bei Plexiglas*, Proceedings of the International Conference on Physics of Noncrystalline Solids, Prins J.A. [Ed.], Delft, The Netherlands, 481–490, 1964.
2. THEOCARIS P.S., *Local Yielding Around a Crack-Tip in Plexiglas*, Journal of Applied Mechanics, **37**, 409–415, 1970,
3. THEOCARIS P.S., *The Constrained Zones in Collinear Asymmetric Cracks by the Method of Caustics*, Proceedings of the 7th All Union Conference on Photoelasticity, Tallinn, November 1971, **2**, 221–236, 1971.
4. KALTHOFF J.F., *Shadow optical method of caustics*, Handbook of Experimental Mechanics, Kobayashi A.S. [Ed.], Prentice-Hall, New York, pp. 430–498, 1987.
5. THEOCARIS P.S., GDOUTOS E.E., *An optical method for determining opening-mode and edge sliding-mode stress intensity factors*, Journal of Applied Mechanics, **39**, 91–97, 1972.
6. ROSSMANITH H.P., *General mode-1 caustic evaluation for optically anisotropic materials*, Archive of Applied Mechanics, **50**, 73–83, 1981.
7. THEOCARIS P.S., IOAKIMIDIS N.I., *Application of the method of caustics to the determination of the ratio of Poisson's ratio to the modulus of elasticity*, Journal of Physics D: Applied Physics, **12**, 1321–1324, 1979.
8. YOUNIS N.T., ZACHARY L.W., *A new technique for the determination of stress-optical constants using the shadow spot method*, Experimental Mechanics, **29**, 75–79, 1989.
9. THEOCARIS P.S., *Experimental study of plane elastic contact problems by the pseudocaustics method*, Journal of Mechanics and Physics of Solids, **27**, 15–32, 1979.
10. THEOCARIS P.S., RAZEM C., *Deformed boundaries determined by the method of caustics*, The Journal of Strain Analysis for Engineering Design, **12**, 223–232, 1977.

11. KALTHOFF J.F., WINKLER S., BEINERT J., *Dynamic SIFs for arresting cracks in DCB Specimens*, International Journal of Fracture, **12**, 317–319, 1976.
12. THEOCARIS P.S., ANDRIANOPOULOS N.P., *Dynamic three-point bending of short beams studied by caustics*, International Journal of Solids and Structures, **17**, 707–715, 1981.
13. PAPADOPOULOS G.A., *Dynamic Caustics and its Applications*, Optics and Lasers in Engineering, **13**, 211–249, 1990.
14. GEORGIADIS H.G., PAPADOPOULOS G.A., *On the method of dynamic caustics in crack propagation experiments*, International Journal of Fracture, **54**, R19–R22, 1992.
15. ROSAKIS A.J., FREUND L.B., *Optical measurements of the plastic strain concentration at a tip in a ductile steel plate*, Journal of Engineering Materials and Technology (Transactions of the ASME), **104**, 115–125, 1982.
16. KIKUCHI M., HAMANAKA S., *Evaluation of the J-Integral by the Caustics Method*, Transactions of the Japan Society of Mechanical Engineers A, **56**(532), 2581–2587, 1990.
17. PAPADOPOULOS G.A., *New formula of experimental stress intensity factor evaluation by caustics*, International Journal of Fracture, **171**, 79–84, 2011.
18. YAO XUEFENG, XU WEI, *Recent application of caustics on experimental dynamic fracture studies*, Fatigue & Fracture of Engineering Materials & Structures, **34**, 448–459, 2011.
19. YAO XUEFENG, XU WEI, JIN GUAN CHANG, YEH HSIEN YANG, *Low velocity impact study of laminate composites with mode I crack using dynamic optical caustics*, Journal of Reinforced Plastics and Composites, **23**, 1833–1844, 2004.
20. XIONG CHUNYANG, YAO XUEFENG, FANG JING, *A study of dynamic caustics around running interface crack tip*, Acta Mechanica Sinica (English Series) **15**, 182–192, 1999.
21. SHEN S.-P., NISHIOKA T., *Theoretical development of the method of caustics for intersonically propagating interfacial crack*, Engineering Fracture Mechanics, **70**, 643–655, 2003.
22. TOMLINSON R.A., PATTERSON E.A., *A study of residual caustics generated from fatigue cracks*, Fatigue and Fracture of Engineering Materials & Structures, **20**, 1467–1479, 1997.
23. SEMENSKI D., *Optical method of caustics – Fulfilled experimental application to the contact problem*, Proceedings of the XVII IMEKO World Congress Metrology in the 3rd Millennium, June 22–27, 2003, Dubrovnik, Croatia, pp. 1952–1955, 2003.
24. BAKIĆ A., SEMENSKI D., JECIĆ S., *Contact caustics measurements expanded to anisotropic materials*, Archives of Civil and Mechanical Engineering, **11**, 497–505, 2011.
25. PATTERSON E.A., WHELAN M.P., *Tracking nanoparticles in an optical microscope using caustics*, Nanotechnology, **19**, 105502 (7pp), 2008.
26. SEMENSKI D., *Method of caustics in fracture mechanics of mechanically anisotropic materials*, Engineering Fracture Mechanics, **58**, 1–10, 1997.
27. SEMENSKI D., JECIĆ S., *Experimental caustics analysis in fracture mechanics of anisotropic materials*, Experimental Mechanics, **39**, 177–183, 1999.
28. YAO XUEFENG, ZHAO HONG PING, YEH HSIEN-YANG, *Dynamic caustic analysis of propagating Mode II cracks in transversely isotropic material*, Journal of Reinforced Plastics and Composites, **24**, 657–667, 2005.
29. KEZHUANG GONG, ZHENG LI, *Caustics method in dynamic fracture problem of orthotropic materials*, Optics and Lasers in Engineering, **46**, 614–619, 2008.

30. YAO XUEFENG, XU WEI, BAI SHULIN, YEH, HSIEN-YANG, *Caustics analysis of the crack initiation and propagation of graded materials*, Composites Science and Technology, **68**, 953–962, 2008.
31. GONG KEZ HUANG, LI ZHENG, QIN WEI HONG, *Influence of loading rate on dynamic fracture behavior of fiber-reinforced composites*, Acta Mechanica Solida Sinica, **21**, 457–460, 2008.
32. GDOUTOS E.E., *Stress Triaxiality at Crack Tips Studied by Caustics*, Recent Advances in Mechanics, Gdoutos E.E., Kounadis A.N. [Eds.], pp. 383–396, Springer, 2011.
33. YOUNIS N.T., *Designing an optical mechanics experiment*, World Transactions on Engineering and Technology Education, **9**, 137–144, 2011.
34. CARAZO-ALVAREZ J., PATTERSON E.A., *A general method for automated analysis of caustics*, Optics and Lasers in Engineering, **32**, 95–110, 1999.
35. THEOCARIS P.S., RAZEM C., *Error analysis in evaluating SIFs by reflected caustics*, International Journal of Mechanical Sciences, **23**, 275–284, 1981.
36. ROSSMANITH H.P., *The influence of geometrical imperfections in the method of caustics*, Engineering Fracture Mechanics, **18**, 903–908, 1983.
37. WALLHEAD I.R., GUNGOR S., EDWARDS L., *Optimisation of the optical method of caustics for the determination of stress intensity factors*, Optics and Lasers in Engineering, **20**, 109–133, 1994.
38. KONSTA-GDOUTOS M., GDOUTOS E.E., *Guidelines for applying the method of caustics in crack problems*, Experimental Techniques, **16**, 25–28, 1992.
39. ROSAKIS A.J., ZEHNDER A.T., *On the method of caustics: An exact analysis based on geometrical optics*, Journal of Elasticity, **15**, 347–367, 1985.
40. SPYROPOULOS C.P., *Stress intensity factor determination error by the method of caustics*, Theoretical and Applied Fracture Mechanics, **35**, 179–186, 2001.
41. MUSKHELISHVILI N.I., *Some Basic Problems of the Mathematical Theory of Elasticity*, Groningen, Noordhoff, 1963.
42. THEOCARIS P.S., PAZIS D.N., *Some further properties of caustics useful in mechanical applications*, Applied Optics, **20**, 4009–4018, 1981.
43. MANOGG P., *Investigation of the rupture of a plexiglas plate by means of an optical method involving high-speed filming of the shadows originating around holes drilled in the plate*, International Journal of Fracture, **2**, 604–613, 1966.
44. RAPTIS K., PAPADOPOULOS G.A., COSTOPOULOS T.N., TSOLAKIS A.D., *Experimental study of load sharing in roller bearing contact by caustics and photoelasticity*, American J. Engineering and Applied Sciences, **4**, 294–300, 2011.
45. YANG R., YUE Z., SUN Z., XIAO T., GUO D., *Dynamic fracture behavior of rock under impact load using the caustics method*, Mining Science and Technology, **19**, 79–83, 2009.
46. KOURKOULIS S.K., MARKIDES CH.F., BAKALIS G., *Smooth elastic contact of cylinders by caustics: the contact length in the Brazilian-disc test*, Archives of Mechanics, **65**, 4, 313–338, 2013.

Received March 29, 2013; revised version July 11, 2013.

Mechanical Properties of AW8S-V Polyester Composite under Various Loading Conditions

Wojciech MOĆKO^{1),2)}, Tadeusz SZYMCZAK²⁾
Zbigniew L. KOWALEWSKI¹⁾

¹⁾ *Institute of Fundamental Technological Research PAN*
Pawińskiego 5B, 02-106 Warszawa, Poland

²⁾ *Motor Transport Institute*
Jagiellońska 80, 03-301 Warsaw, Poland
e-mail: wmocko@ippt.pan.pl

This article presents the results of an analysis of the mechanical properties of the AW8S-V polyester composite reinforced by a roving fabric under tensile loading. The stress-strain curves show an increase of the maximum stress and elastic modulus with increasing strain rate. By contrast, an increase of the temperature led to decrease of the maximum stress and elastic modulus. It is also shown that, failure mechanisms are dependent on the loading type. Shear cracks occurred in the specimens under quasi-static loading whereas composite layers damage was observed under dynamic loading. Temperature increase resulted to stronger fragmentation of the specimens.

Key words: polyester composite, Hopkinson bar, high strain rate, damage.

1. INTRODUCTION

Polyester composites are commonly used in many different branches of industry, including the naval, aeronautics, motor transport and energetics (wind farm), because of their excellent mechanical properties, low cost, ease of fabrication and good strength-to-weight ratio. Polyester composites are applied, for example, in energy-absorbing structures [1, 2] and ballistic shields [3, 4]. Both of these applications involve exposure to extreme loading and high strain levels, which may lead to material damage. Therefore, material characterisation over a wide range of strain rates and temperatures is required for the design of energy-absorbing and protective structures. Previous studies of polyester matrix composites have reported that the strain rate affects the elastic modulus and maximum stress of these composite materials [1, 5]. In addition, it has been

observed that changes in the strain rate affect the mechanism by which material damage occurs.

This study analyses the mechanical properties of the AW8S-V polyester matrix composite, developed by the Military Institute of Armour and Vehicle Technology and the Alter Company. It was originally designed for a lightweight armour used by soldiers and military vehicles. The polyester composite, in the form of 8-mm plate, was made of the resin ATLAC 580 ACT and reinforced by 15 layers of the single oriented roving fabric STR-003-500-110.

2. COMPOSITE BEHAVIOUR UNDER MONOTONIC DEFORMATION AT VARIOUS TENSILE STRAIN RATES

The objective of this section is to report the results of tests performed to evaluate the mechanical parameters of the AW8S-V, i.e., Young's modulus, ultimate tensile stress and their variations as a function of the tensile strain rate. All tests were conducted at room temperature on a servo-hydraulic Instron testing machine using flat specimens with a gauge length and width equal to 80 mm and 16 mm, respectively. Three load-frame velocities of the testing machine were applied, and as a result, the following strain rates were obtained: $2.0 \times 10^{-4} \text{ s}^{-1}$, $3.0 \times 10^{-4} \text{ s}^{-1}$ and $4.2 \times 10^{-3} \text{ s}^{-1}$. The material deformation was measured by a clip-on knife edge extensometer with a gauge length of 80 mm. To identify any possible anisotropy of the composite, the specimens were cut out from the composite plate along three directions, i.e., 0° , 45° , and 90° , with respect to the symmetry axis.

Figure 1 presents the stress-strain characteristics obtained for each orientation considered. The figure illustrates differences in the tensile curves, and hence differences in such mechanical parameters as Young's modulus and ultimate tensile stress. For the 0° and 90° orientations, the stress-strain relationship was

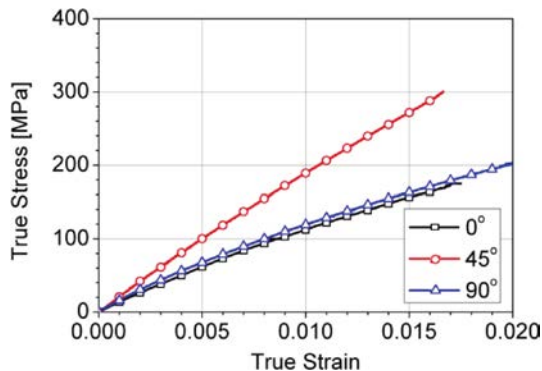


FIG. 1. Stress-strain characteristics of the composite, selected along the three directions considered.

non-linear, whereas for 45° , it could be well described by a linear function. The elastic modulus was strongly dependent on the specimens' orientation. For the directions indicated – 0° , 45° and 90° – the following values of the elastic modulus were obtained: 11890 MPa, 20186 MPa, 12902 MPa, respectively (Figs. 1 and 2a). The lowest ultimate tensile stress, 174 MPa, was recorded for the 0° orientation, whereas the highest, 301 MPa, was achieved for the 45° direction (Fig. 2b).

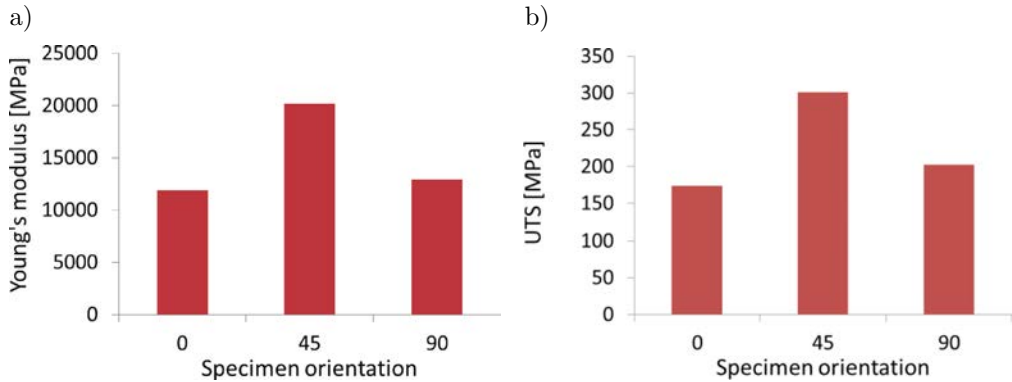


FIG. 2. Variations of Young's modulus (a) and ultimate tensile stress (b) versus specimen orientation.

In addition to the variation of the composite properties, different types of decohesion were clearly observed (Fig. 3a). A fracture zone of specimens cut

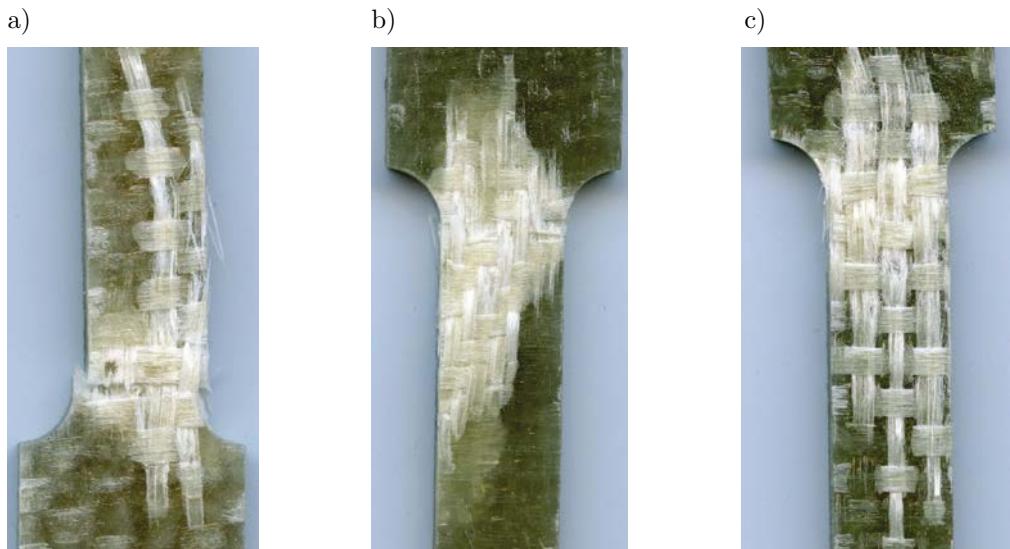


FIG. 3. Photographs of the fractured specimens cut out along the 0° (a), 45° (b) and 90° (c) directions.

out along the 0° and 90° directions showed similar features (Figs. 3a and 3c). Damage was developed mainly in the fibres oriented either longitudinal or perpendicular to the specimen surface. In the case of specimens cut out along the 45° direction, damage appeared over the whole cross-section of the material volume (Fig. 3b).

The effect of tension velocity on the mechanical parameters of the composite is illustrated in Fig. 4. It can be clearly observed that the Young's modulus and ultimate tensile stress for the 0° and 90° directions slightly increased in comparison to their initial values. For specimens oriented along the 45° direction, a slight decrease of the Young's modulus and an increase of the ultimate tensile stress were obtained.

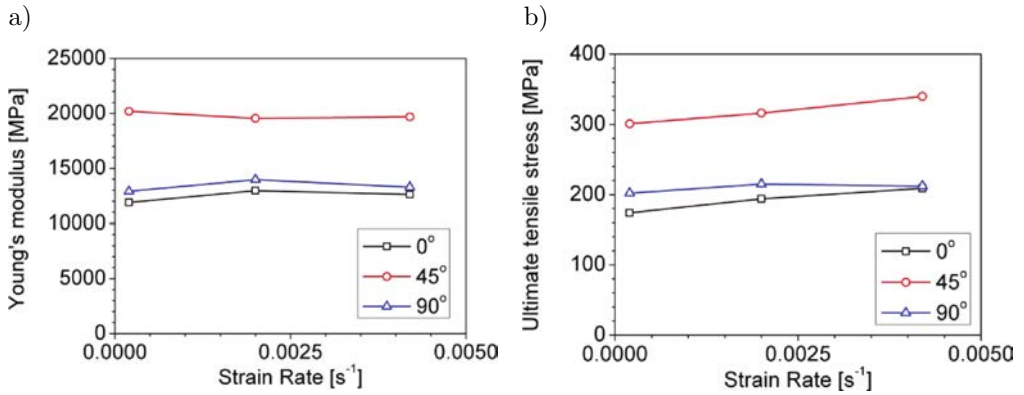


FIG. 4. Young's modulus (a) and ultimate tensile stress (b) *versus* strain rate.

3. COMPRESSION TESTS OVER WIDE RANGE OF STRAIN RATES AND TEMPERATURES

An analysis of the mechanical properties of the polyester composite was performed using two different test setups for cylindrical specimens machined from the composite plate. The diameter and height of the specimens were equal to 8 mm. A servo-hydraulic testing machine equipped with a laser extensometer was used for the quasi-static deformation test, and the split Hopkinson pressure bar (SHPB) was applied for testing at high strain rates [6]. The SHPB test setup incorporated two bars of 2 m length and 20 mm diameter, which were fabricated using maraging steel characterised by a very high yield point (2200 MPa). Electrical signals measurements were carried using tensometers bonded to the centre of the bars. The electrical signals emitted by the tensometers were amplified using a wideband measurement bridge provided by Vishay, and the data were then captured and stored using an Agilent digital oscilloscope. The stress, strain and strain rate of the specimens were estimated based on the stress recorded in the

incident and transmitter bars, similarly to the method described in the literature [6–11]. Stress-strain curves of the AWS8S-V composite at various temperatures were obtained using the SHPB test setup equipped with an environmental chamber. To obtain a homogenous temperature distribution across the materials, the specimens were conditioned for 30 minutes before the start of mechanical testing. The subsequent deformation stages of the composite were recorded using a high-speed camera (Fig. 5).

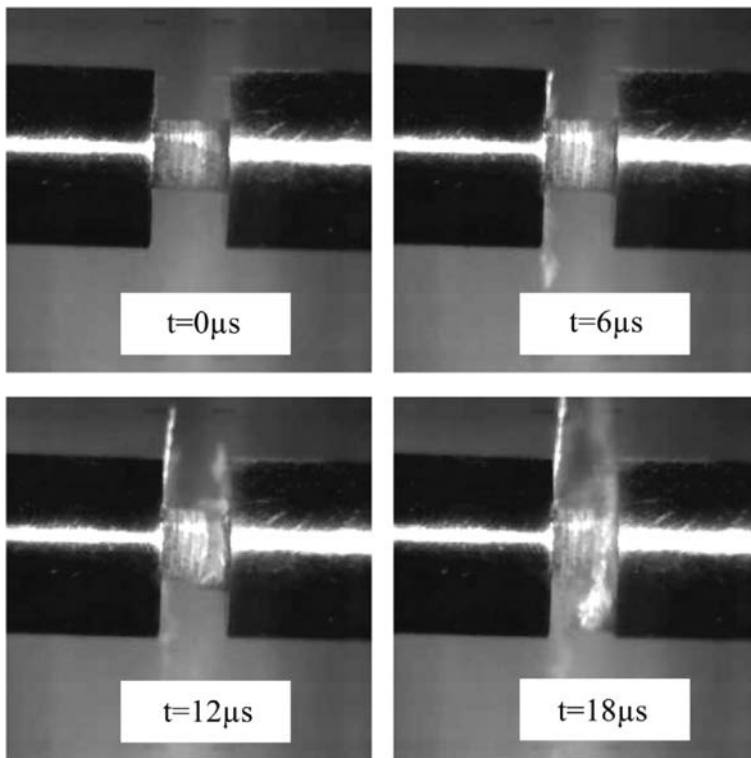


FIG. 5. Stages of composite compression using the SHPB method.

The results of the dynamic compression test, conducted over an initial temperature range of -35°C to 100°C , are shown in Fig. 6. Since the composite shows brittle behaviour it may be assumed that temperature increase due to plastic deformation is negligible. All stress-strain curves presented in this figure can be divided into three stages [12]. In the first stage, up to a strain $\varepsilon = 0.03$, a linear relationship between stress and strain was observed. At higher strain, all characteristics became non-linear, i.e., their slope with respect to the strain axis started to decrease. Such behaviour may be attributed to microdamage of the composite structure [13, 14]. In the final stage of deformation, macroscopic

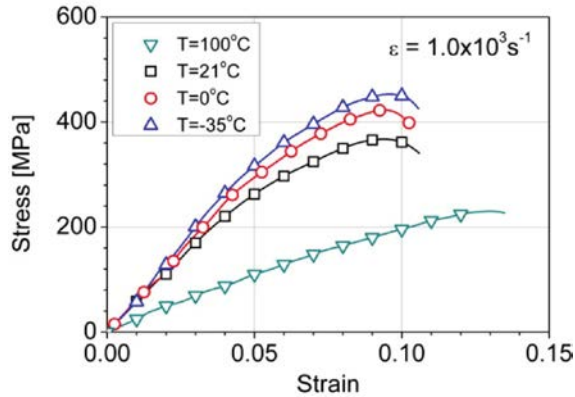


FIG. 6. Adiabatic stress-strain curves at various temperatures.

material damage appeared when the stress attained a maximum value, as shown in the diagram. Analysis of the curves shown in Fig. 6 indicates that the temperature increase led to a decrease of the stress-strain slope and the maximum stress required for macroscopic material damage to be initiated.

Photographs and SEM images of fractured specimens taken after the tests at various temperatures are shown in Fig. 7 and Fig. 8, respectively. The specimens tested at -35°C and 0°C exhibited damage limited to a single composite layer of the material. The damage was manifested as extensive fragmentation of the composite without visible macroscopic cracks. Contrary to such behaviour, the specimens tested at higher temperatures, 21°C and 100°C , displayed strong fragmentation as well as delamination of the matrix and reinforcement phase.

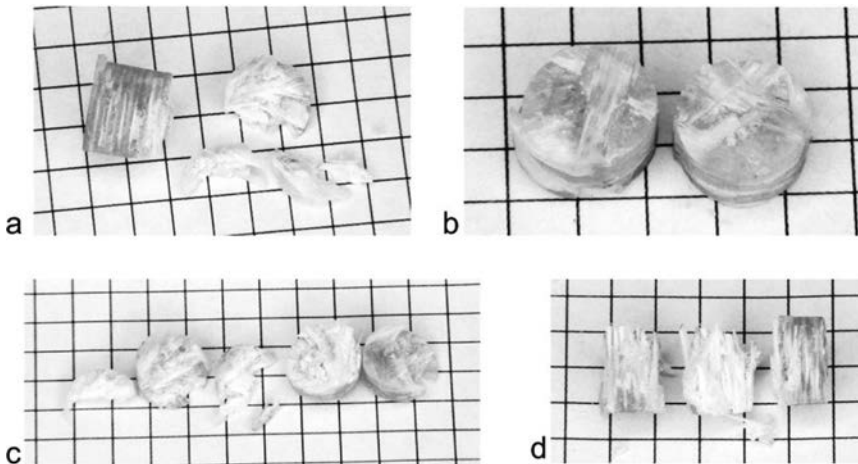


FIG. 7. Photographs of specimens damaged during dynamic loading at various temperatures: a) $T = -35^{\circ}\text{C}$; b) $T = 0^{\circ}\text{C}$; c) $T = 21^{\circ}\text{C}$; d) $T = 100^{\circ}\text{C}$.

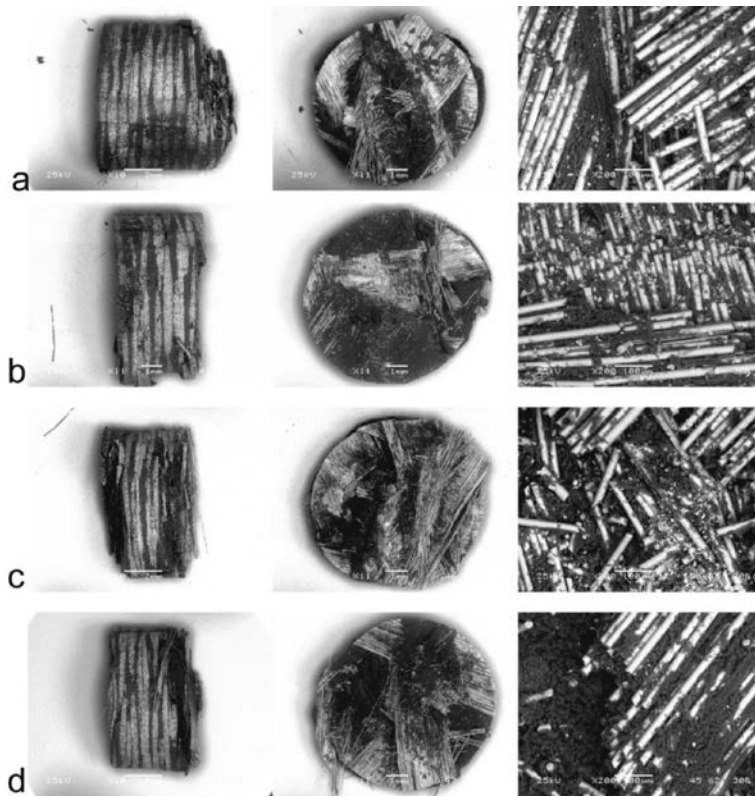


FIG. 8. SEM images of specimen damaged under dynamic loading conditions at various temperatures: a) $T = -35^{\circ}\text{C}$; b) $T = 0^{\circ}\text{C}$; c) $T = 21^{\circ}\text{C}$; d) $T = 100^{\circ}\text{C}$.

The stress-strain relationship calculated for various strain rates within the range of $1.9 \times 10^{-4} \text{ s}^{-1}$ to $1.6 \times 10^3 \text{ s}^{-1}$ are shown in Fig. 9. An increase of the curves slope was observed with an increase of the strain rate.

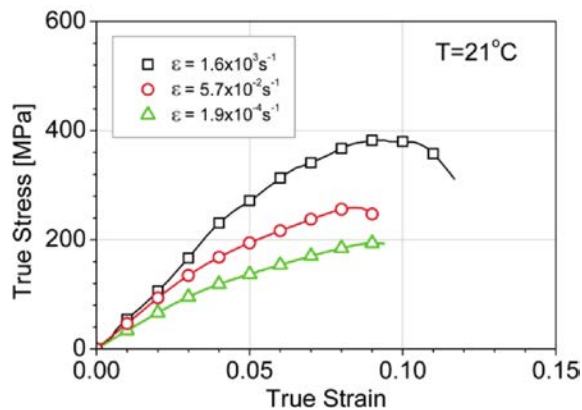


FIG. 9. Stress-strain curves at various strain rates.

Material damage occurred at the same strain level of approximately 0.08, independently of the strain rate, in all specimens tested. The maximum stress required for material damage increased significantly with the strain rate.

Photographs and SEM views of the specimens after compressive load testing at various strain rates are shown in Figs. 10 and 11, respectively. Oblique cracks

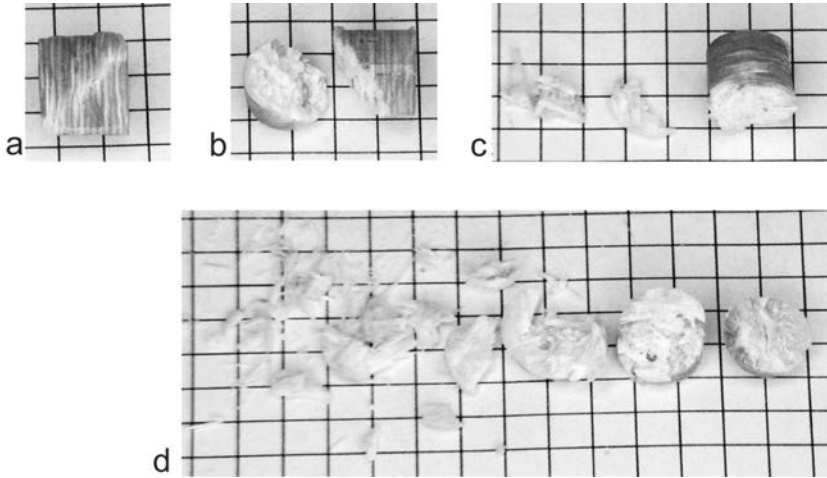


FIG. 10. Photographs of the specimens damaged at room temperature at various strain rates: a) $\dot{\epsilon} = 1.9 \times 10^{-4} \text{ s}^{-1}$; b) $\dot{\epsilon} = 5.7 \times 10^{-2} \text{ s}^{-1}$; c) $\dot{\epsilon} = 1.0 \times 10^3 \text{ s}^{-1}$; d) $\dot{\epsilon} = 1.6 \times 10^3 \text{ s}^{-1}$.

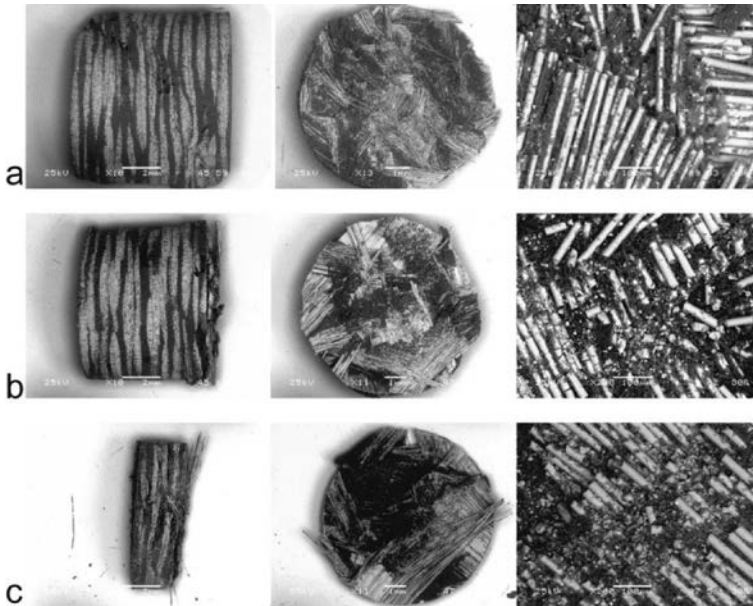


FIG. 11. SEM images of specimens damaged under dynamic loading conditions at various strain rates: a) $\dot{\epsilon} = 5.7 \times 10^{-2} \text{ s}^{-1}$; b) $\dot{\epsilon} = 1.0 \times 10^3 \text{ s}^{-1}$; c) $\dot{\epsilon} = 1.6 \times 10^3 \text{ s}^{-1}$.

at an angle of 45° relative to the perpendicular direction were observed in the specimens that were tested using the servo-hydraulic testing machine. Therefore, it may be concluded that material damage occurs as a result of shear stress. For the strain rate of $1.9 \times 10^{-4} \text{ s}^{-1}$, a clearly visible crack without material separation was observed in the specimen. In the case of specimen tested at the strain rate of $5.7 \times 10^{-2} \text{ s}^{-1}$ it was split into two parts. Macroscopic oblique cracks were not visible in the specimens under dynamic loading, indicating that the mechanism of material damage is different than for the static one. At a strain rate of $1.0 \times 10^3 \text{ s}^{-1}$, the surface layer of the composite was destroyed, whereas the further increase of the strain rate, up to $1.6 \times 10^3 \text{ s}^{-1}$, resulted to the damage and fragmentation of the entire volume of the specimen.

The elastic modulus values were determined from the linear sections of the stress-strain curves and were observed to be strongly related to the temperature and strain rate, as shown in Fig. 12. It can be observed that the elastic modulus increased with the strain rate (Fig. 12a) due to the viscoelastic behaviour of the matrix material.

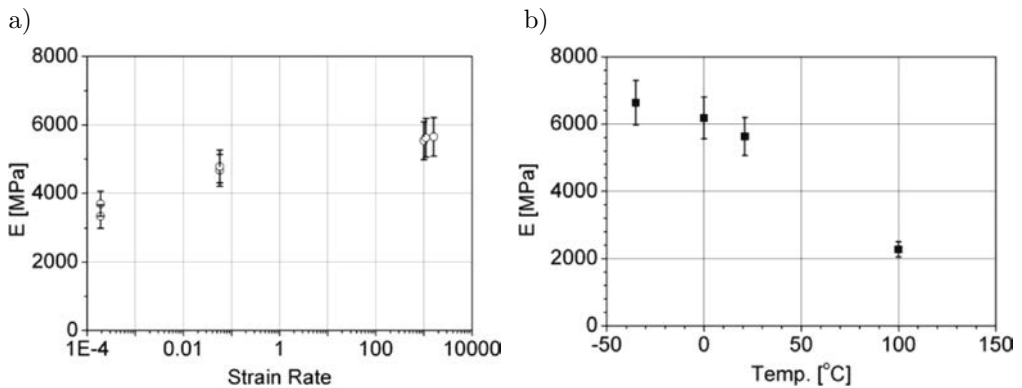


FIG. 12. Elastic modulus *versus* strain rate (a) and temperature (b).

Wide range of the mathematical models of mechanical behaviour of composites was already introduced [15–21]. In this work very accurate solution is proposed taking into account temperature and strain rate effect. The effect of the strain rate on the material stiffness may be described using the following formula [22]:

$$(3.1) \quad E_{rt} = E_0 \left(1 + C_i \ln \frac{\dot{\epsilon}_i}{\dot{\epsilon}_0} \right), \quad i = 2, \dots, 4,$$

where E_{rt} – the rate-dependent stiffness; E_0 – the stiffness determined from quasi-static tests at a strain rate equal to $\dot{\epsilon}_0$; C_2 , C_3 and C_4 – the strain rate constants for the longitudinal, shear and transverse modules, respectively; $\dot{\epsilon}$ – the

current strain rate. Equation (3.1) was calibrated using the data obtained during through-thickness compression tests performed over a wide range of strain rates. The experimental and model-based Young's moduli are compared in Fig. 13a.

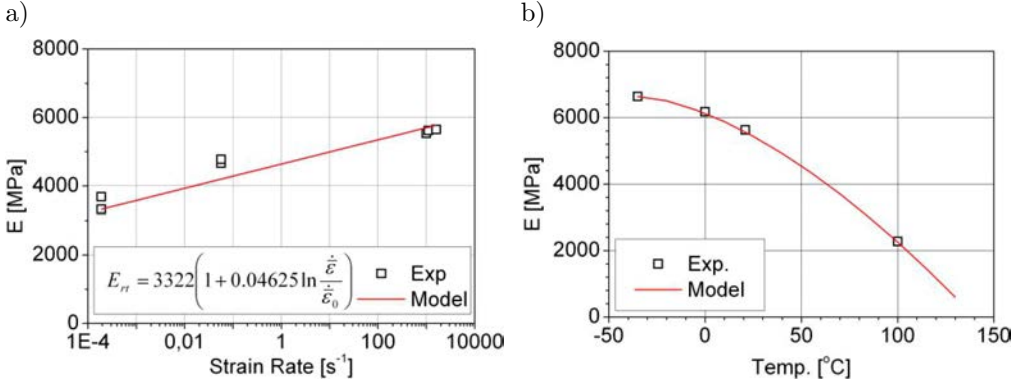


FIG. 13. Predictions of the elastic modulus versus strain rate (a) and temperature (b).

The other factor that affects the value of the elastic modulus is temperature. It can be observed that an increase of temperature causes material softening. The thermal softening phenomenon can be expressed analytically as follows:

$$(3.2) \quad E(T) = E_0 \left[1 - \left(\frac{T - T_0}{T_m - T_0} \right)^m \right],$$

where E_0 , T_m and m denote the Young's modulus at the reference temperature T_0 , melting temperature, and temperature coefficient, respectively.

Taking into account Young's modulus dependence on both, strain rate and temperature, Eq. (3.1) and Eq. (3.2) can be rewritten as:

$$(3.3) \quad E(\dot{\epsilon}, T) = E_0 \left(1 + C_i \ln \frac{\dot{\epsilon}}{\dot{\epsilon}_0} \right) \left[1 - \left(\frac{T - T_0}{T_m - T_0} \right)^m \right], \quad i = 2, \dots, 4.$$

Based on experimental data obtained during Hopkinson bar tests at various temperatures, the following parameters were estimated: $E_0 = 46\,634$ MPa, $T_m = 140^{\circ}C$ and $m = 1.6$. The model prediction results are presented in Fig. 13b.

4. CONCLUSIONS

The mechanical properties of the polyester composite AWS8S-V were measured under tensile loading along three various directions of the composite sheet plane and under compressive loading perpendicular to the surface.

Summarising of the experimental results from tension tests, it is worth to emphasise that the AWS8S-V composite is an anisotropic material, and its mechanical properties are strongly dependent on the orientation of the material

volume. The maximum values of Young's modulus and ultimate tensile strength were achieved along the direction of 45° . As demonstrated by the results, these parameters were not significantly sensitive to variation of the tension velocity within the range of values applied.

The results of the compression test showed that the mechanical properties were strongly affected by the strain rate and temperature. Increase of the strain rate resulted in material hardening effects, including an increase of the elastic modulus and the generation of maximum stress leading to material damage [5, 23]. This behaviour may be caused by the viscoelastic properties of the composite matrix. In addition, the type of loading affects the mechanism of material damage; for example, shear cracks were observed under quasi-static loading conditions, whereas strong fragmentation of the material layers was observed under dynamic ones [23]. Rapid damage and delamination of the whole specimen volume occurred at the highest strain rate considered.

In addition, a temperature increase led to material softening behaviour, i.e. a decrease of the elastic modulus and generation of the maximum stress responsible for material damage. Stronger composite fragmentation and delamination were observed for higher values of temperature.

REFERENCES

1. SOLAIMURUGAN S., VELMURUGAN R., *Progressive crushing of stitched glass/polyester composite cylindrical shells*, Compos. Sci. Technol., **67**, 422–437, 2007.
2. OBRADOVIC J., BORIA S., BELINGARDI G., *Lightweight design and crash analysis of composite frontal impact energy absorbing structures*, Compos. Struct., **94**, 423–430, 2012.
3. ALMOHANDES A.A., ABDEL-KADER M.S., ELEICHE A.M., *Experimental investigation of the ballistic resistance of steel-fiberglass reinforced polyester laminated plates*, Compos. Part B-Eng., **27**, 447–458, 1996.
4. BUITRAGO B.L., GARCÍA-CASTILLO S.K., BARBERO E., *Experimental analysis of perforation of glass/polyester structures subjected to high-velocity impact*, Mater. Lett., **64**, 1052–1054, 2010.
5. SHAH KHAN M.Z., SIMPSON G., TOWNSEND C.R., *A comparison of the mechanical properties in compression of two resin systems*, Mater. Lett., **52**, 173–179, 2002.
6. KOLSKY H., *An Investigation of the mechanical properties of materials at very high rates of deformation of loading*, Proc. Phys. Soc., **62B**, 647, 1949.
7. MOĆKO W., KOWALEWSKI Z.L., *Dynamic Compression Tests – Current Achievements and Future Development*, Eng. Trans., **59**, 235–248, 2011.
8. MOĆKO W., KRUSZKA L., *Results of Strain Rate and Temperature on Mechanical Properties of Selected Structural Steels*, Procedia Engineering, **57**, 789–797, 2013.
9. MOĆKO W., KOWALEWSKI Z.L., *Application of FEM in the assessment of phenomena associated with dynamic investigations on a miniaturised DICT testing stand*, Kovove Mater., **51**, 71–82, 2013.

10. MOĆKO W., RODRÍGUEZ-MARTÍNEZ J.A., KOWALEWSKI Z.L., RUSINEK A., *Compressive viscoplastic response of 6082-T6 and 7075-T6 aluminium alloys under wide range of strain rate at room temperature: Experiments and modelling*, *Strain*, **48**, 498–509, 2012.
11. MOĆKO W., KOWALEWSKI Z.L., *Mechanical properties of the A359/SiCp metal matrix composite at wide range of strain rates*, *Appl. Mech. Mater.*, **82**, 166–171, 2011.
12. DI BELLA G., CALABRESE L., BORSELLINO C., *Mechanical characterization of a glass/polyester sandwich structure for marine applications*, *Mater. Design.*, **42**, 486–494, 2012.
13. SUMELKA W., ŁODYGOWSKI T., *The influence of the initial microdamage anisotropy on macrodamage mode during extremely fast thermomechanical processes*, *Arch. Appl. Mech.*, **81**, 1973–1992, 2011.
14. GLEMA A., ŁODYGOWSKI T., SUMELKA W., PERZYNA P., *The numerical analysis of the intrinsic anisotropic microdamage evolution in elasto-viscoplastic solids*, *Int. J. Damage Mech.*, **18**, 205–231, 2009.
15. GIELETA R., KRUSZKA L., *Dynamic testing of reinforced glass fibre-epoxy composite at elevated temperatures*, *Strength Mater.*, **34**, 238–241, 2002.
16. MAHMOUDI N., HEBBAR A., ZENASNI R., LOUSDAD A., *Effect of impact directions, fiber orientation, and temperature on composite material*, *J. Compos. Mater.*, **43**, 1713–1727, 2009.
17. WANG W., MAKAROV G., SHENOI R.A., *An analytical model for assessing strain rate sensitivity of unidirectional composite laminates*, *Compos. Struct.*, **69**, 45–54, 2005.
18. SHOKRIEH M.M., OMIDI M.J., *Compressive response of glass-fiber reinforced polymeric composites to increasing compressive strain rates*, *Compos. Struct.*, **89**, 517–523, 2009.
19. THIRUPPUKUZHI S.V., SUN C.T., *Models for the strain-rate-dependent behaviour of polymer composites*, *Compos. Sci. Technol.*, **61**, 1–12, 2001.
20. THIRUPPUKUZHI S.V., SUN C.T., *Testing and modelling high strain rate behaviour of polymeric composites*, *Compos. Part B*, **29B**, 535–546, 1998.
21. XIA Y., WANG X., *Constitutive equation for unidirectional composites under tensile impact*, *Compos. Sci. Technol.*, **56**, 155–160, 1996.
22. KARA A., TASDEMIRCI A., GUDEN M., *Modeling quasi-static and high strain rate deformation and failure behaviour of a (± 45)symmetric E-glass/polyester composite under compressive loading*, *Mater. Design.*, **49**, 566–574, 2013.
23. SHAH KHAN M.Z., SIMPSON G., *Mechanical properties of a glass reinforced plastic naval composite material under increasing compressive strain rates*, *Mater. Lett.*, **45**, 167–174, 2000.

Received August 27, 2013; revised version November 12, 2013.

Method for Determination of the Dynamic Elastic Modulus for Composite Materials

Abdellah MASSAQ^{1), 2)}, Alexis RUSINEK³⁾, Maciej KLÓSAK^{4), 5)}

¹⁾ *Ecole Nationale des Sciences Appliquées*

Avenue Abdelkrim Khattabi, 40000, Guéliz-Marrakech, Maroc

²⁾ *IbnoZohr University, Faculty of Sciences Agadir*

BP. 8106 Quartier Dakhla, Agadir, Morocco; e-mail: a.massaq@uiz.ac.ma

³⁾ *National Engineering School of Metz ENIM*

Laboratory of Mechanics, Biomechanics, Polymers and Structures – LaBPS, EA 4632
1 route d’Ars Laquenexy, CS 65820 57078 METZ Cedex 3, France; e-mail: rusinek@enim.fr

⁴⁾ *Universiapolis, Ecole Polytechnique d’Agadir*

Bab Al Madina, Qr Tilila, Agadir, Morocco; e-mail: klosak@e-polytechnique.ma

⁵⁾ *The State School of Higher Professional Education in Kalisz*

4 Nowy Swiat Street, 62-800 Kalisz, Poland

Majority of polymer matrix composite materials, a marked viscoelastic behavior and faculties of dissipation of energy, it thus proves necessary to know the viscoelastic properties, as the dynamic Young modulus. In this work, we will present a new experimental technique for determining the dynamic elastic modulus at high strain rates of polymer matrix composites materials by a statistical method demanding a large number of tests. This new technique is based on the split Hopkinson pressure bar. Further, we study the effect of strain rate on dynamic elastic modulus of a woven Polyamid 6 – glass fibre reinforced.

Key words: composite, dynamic Young modulus, Hopkinson bar, high strain rate.

1. INTRODUCTION

Elastic constants of materials have a great importance, both for engineering practice and research, because they describe a mechanical behavior of materials. Contrary to static loading for which these constants are clearly defined, the dynamic loading causes some difficulties in their determination. For a long time, dynamic values were derived from static ones. Then they were measured using visco-acoustic methods or ultrasounds [1–5]. However, those methods do not allow to cover a large range of stresses and they give a complex rigidity matrix

only at high frequencies. In order to determine a dynamic elastic modulus, some authors [5] directly use a linear part of stress-strain curve.

Our technique is based on the Hopkinson bar in compression [6, 7] which covers a large range of stresses for a range of very low frequencies. The use of the Hopkinson bar has become the most adopted and widely used method for determination of dynamic properties of composite materials.

2. MATERIAL AND MEASUREMENT TECHNIQUES

2.1. Material

The tested material is a composite made of armor tissue of equilibrate glass fiber and the matrix is composed of Polyamide 6 (PA6). The tests have been carried out on cylindrical specimens, loaded in three compression directions **L1**, **L2** and **T** (Fig. 1).

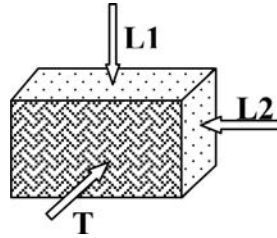


FIG. 1. Compression directions. Direction **T**: compression perpendicular to fibers, directions **L1** and **L2**: compression in the fibers principal direction.

2.2. Measurement of the wave propagation velocity in the composite PA6/glass

2.2.1. Measurement techniques. The technique allows to determine a propagation velocity of an elastic wave through the material cross-section. It uses Hopkinson bars for short-time loading $0 < t < 2\Delta t_s$, where Δt_s is transmission time of the elastic wave in the material [7]. This enables to determine a dynamic longitudinal elastic modulus for stresses close to zero:

$$(2.1) \quad E_d = \lim_{\sigma \rightarrow 0} \left(\frac{\partial \sigma}{\partial \varepsilon} \right)_\sigma .$$

This is a gradient at a point of the characteristic stress-strain curve which is demonstrated in Fig. 2 for the zero point.

The principle of the method is shown in Fig. 3. It consists on determination of time necessary for a wave to pass through the composite specimen. This measurement of time Δt_s is performed in two steps. First, an analysis of the oscillogram of an empty test is made, that means without a specimen and with two bars in contact (Fig. 3a). It allows to obtain the time Δt_0 necessary for the

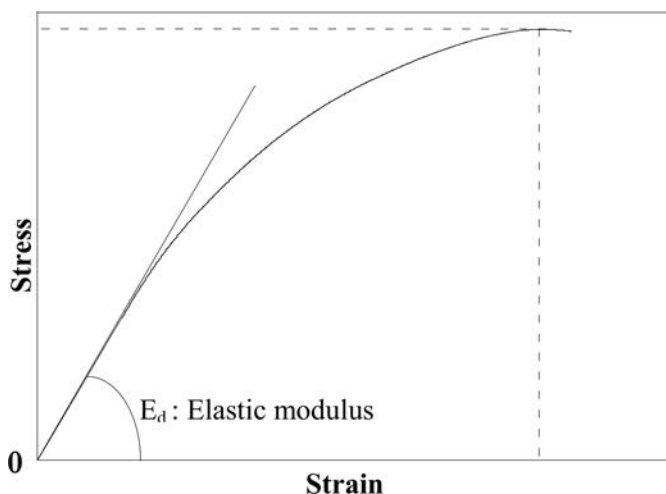


FIG. 2. Representation of the dynamic elastic modulus.

transmission of the elastic wave between the gauges T_1 and T_2 . Second, another test is realized in which the specimen of the length l is introduced between two bars which is shown in Fig. 3b. In this case, we measure the time Δt of the elastic wave transmission between the gauges T_1 and T_2 of the complete system bar-specimen-bar.

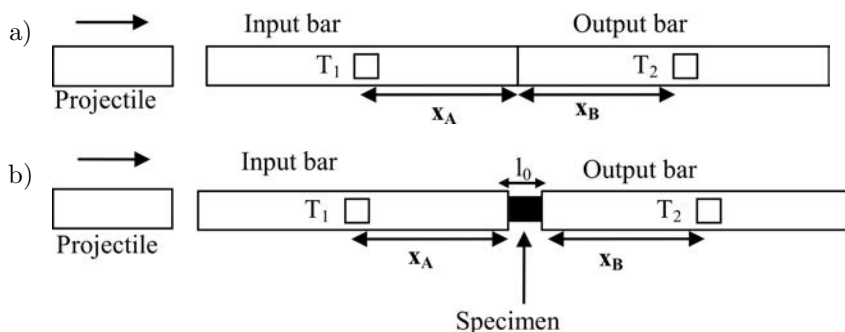


FIG. 3. a) Calibration of the set-up without specimen to define the characteristic time; b) Principle of the method for determination of transmission time of the elastic wave in the specimen.

Thereby, the difference between these two time intervals is equal to the propagation time Δt_s of the wave through the composite specimen. No loading is applied. We have then:

$$(2.2) \quad \Delta t_s = \Delta t - \Delta t_0 .$$

The velocity of the elastic wave in the bar is:

$$(2.3) \quad C_0 = \frac{x_A + x_B}{\Delta t_0} .$$

The celerity of wave propagation in the material is denoted by C_{os} and is given by:

$$(2.4) \quad C_{0s} = \left[\frac{l_0}{\Delta t_s} \right]_{\sigma},$$

where l_0 is the specimen length and σ is the applied loading.

The propagation velocity of the longitudinal elastic wave is independent of a local velocity, this means the velocity of an element that transmits the wave. It only depends on elastic properties of the material and on temperature.

We have carried out an extended study to define conditions for founding experimental results which can be exploitable and with a minimum of the error level due to time dependence. The optimal specimen length of 16 mm has been adopted. In addition, for each specimen we have performed two test series. Each series is made of 100 tests. The first series permits to determine the mean value of $\overline{\Delta t}$ whereas the second one is for Δt_0 evaluation. The tests with and without specimen have been mixed.

2.2.2. Results and discussion. The test results are presented in Figs. 4, 5 and 6. We have defined a basic time $\Delta t_b = 222 \mu s$, from which we obtain:

$$(2.5) \quad \Delta t_0 = \Delta t_0^* + \Delta t_b \quad \text{and} \quad \Delta t = \Delta t^* + \Delta t_b.$$

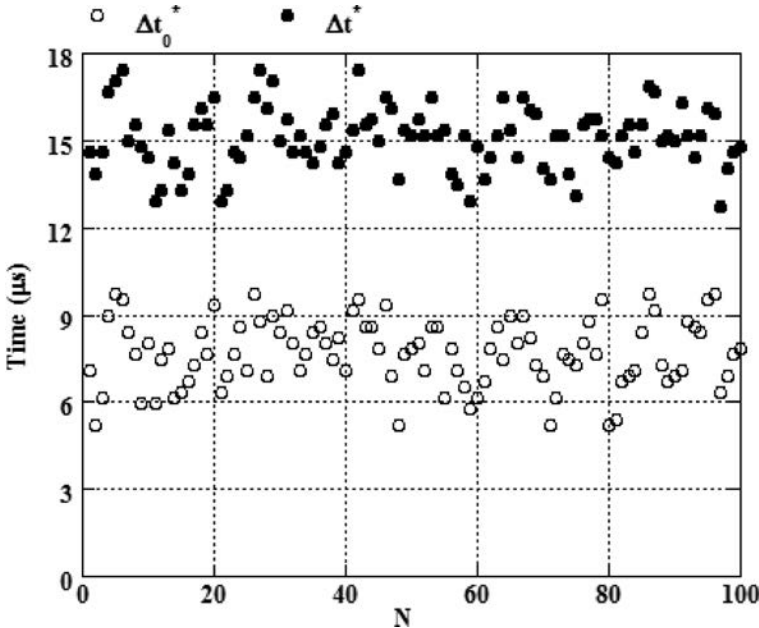


FIG. 4. Evolution of Δt^* and Δt_0^* as a function of the tests number; compression direction T.

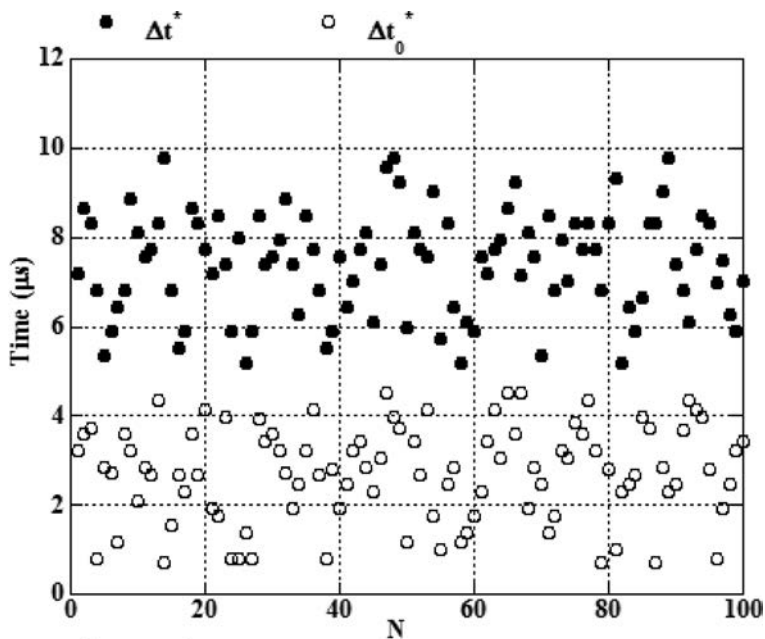


FIG. 5. Evolution of Δt^* and Δt_0^* as a function of the tests number; compression direction **L1**.

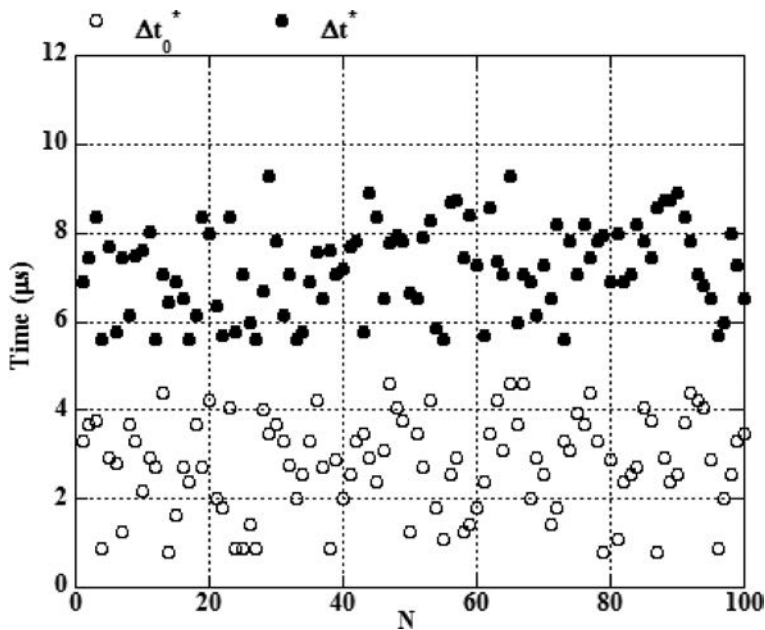


FIG. 6. Evolution of Δt^* and Δt_0^* as a function of the tests number; compression direction **L2**.

In this configuration, Δt_0^* and Δt^* represent new time scales. In order to avoid any risk of cracking in the material core, we have decided to perform tests at very low strain rates from 0.8 s^{-1} to 3 s^{-1} . The large number of tests has permitted to realize a static analysis of Δt and Δt_0 as well as a precise calculation of the wave transmission in our composite material.

The frequencies related to three compression directions given as a function of time Δt and Δt_0 can be presented by the histogram as it is shown in Figs. 7, 8 and 9. The relative frequencies distribution allows to carry out first observations on the evolution of time of the elastic wave propagation, but it also gives a first representation of the cumulative probability. The matrix of this function i.e. a cumulative probability has a key role in the stochastic approach of design.

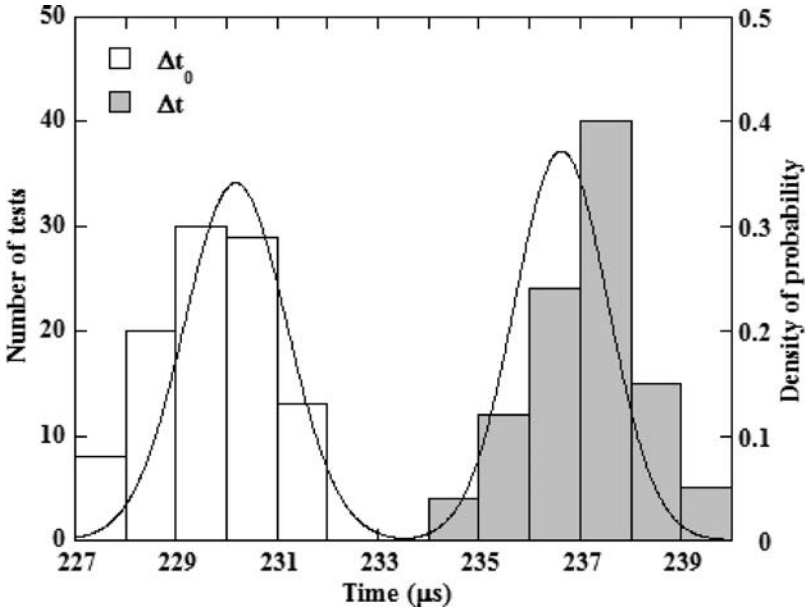


FIG. 7. Frequential distribution of Δt and Δt_0 represented in the form of histogram, adjusted by a normal distribution: compression direction **T**.

Table 1. Maximum relative frequencies and their classes for three compression directions.

Time	Compression direction					
	L1		L2		T	
	Δt_0	Δt	Δt_0	Δt	Δt_0	Δt
Class (μs)	[225–226]	[229–230]	[224–225]	[229–230]	[229–230]	[237–238]
Max. freq %	32	32	30	39	30	40

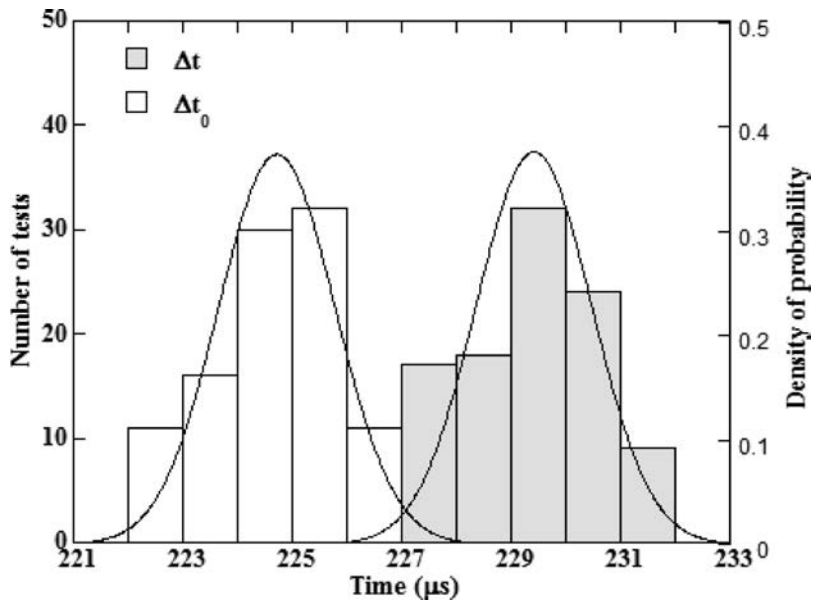


FIG. 8. Frequential distribution of Δt and Δt_0 represented in the form of histogram, adjusted by a normal distribution: compression direction L1.

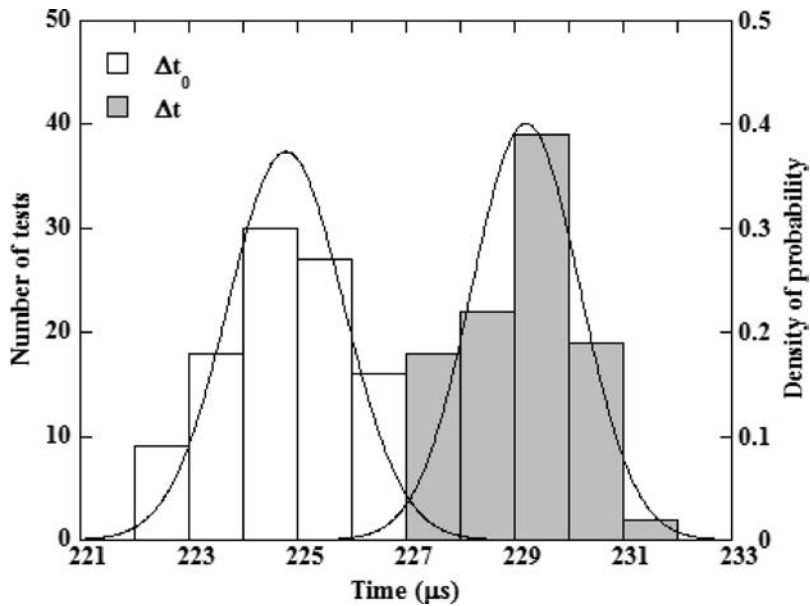


FIG. 9. Frequential distribution of Δt and Δt_0 represented in the form of histogram, adjusted by a normal distribution: compression direction L2.

2.2.3. *Adjustment by the normal law.* In order to perform an analysis based on a stochastic approach, it is fundamental to know a function of the density of

probability. This function can be expressed by the following formula:

$$(2.6) \quad p(\Delta t) = \left[\left(\frac{1}{S} \sqrt{2\pi} \right) \cdot \exp \left(-\frac{1}{2} \left(\frac{\Delta t - \overline{\Delta t}}{S} \right)^2 \right) \right], \quad S > 0.$$

where Δt is a variable.

The mean time $\overline{\Delta t}$ and the interval of type S of this population is given by the following relations, respectively:

$$(2.7) \quad \overline{\Delta t} = \frac{1}{N} \sum_{i=1}^N (\Delta t)_i,$$

$$(2.8) \quad S = \left[\frac{1}{(N-1)} \sum_{i=1}^N (\Delta t - \overline{\Delta t})^2 \right]^{1/2},$$

where N represents the number of observations.

All the histograms obtained during the tests have been adjusted by the normal law described here above. In Table 2, we have reported the mean values $\overline{\Delta t_0}$ and $\overline{\Delta t}$ deduced from those histograms (Figs. 7, 8 and 9) after adjustment by the normal law.

The mean value of the wave passage through the specimen, described as $\overline{\Delta t_s}$, is defined by:

$$(2.9) \quad \overline{\Delta t_s} = \overline{\Delta t} - \overline{\Delta t_0}.$$

The celerity C_{0s} is deduced from the expression (2.4).

It is important to note that due to the use of the value of $\overline{\Delta t_0}$ we could evaluate the elastic wave.

Table 2. Mean values deduced through the normal law.

	Δt_0 (μs)	Δt (μs)	Δt_s (μs)	C_{0s} (mm/ μs)
Compression direction L1	224.72	229.42	4.69	3.359
Compression direction L2	224.79	229.21	4.42	3.548
Compression direction T	229.67	237.11	7.44	2.346

2.2.4. Normality test using the Henry line. In order to validate the results obtained by the static analysis and then adjusted by the normal law, we have compared them with those adjusted by the method of Henry which is described in SAPORTA [8]. The latter consists on the graphical treatment of data. It enables to quickly verify whether a statistical distribution of a continuous variable resembles a normal distribution.

According to the method of Henry, if a variable $\overline{\Delta t}$ is a Gaussian one, for points $(\Delta t_i; U_i)$, where $U_i = (\Delta t_i - \overline{\Delta t})/S$, should be on the same line.

We can conclude from Fig. 10 that the points are aligned and the graphical adjustment using the method of Henry is satisfactory.

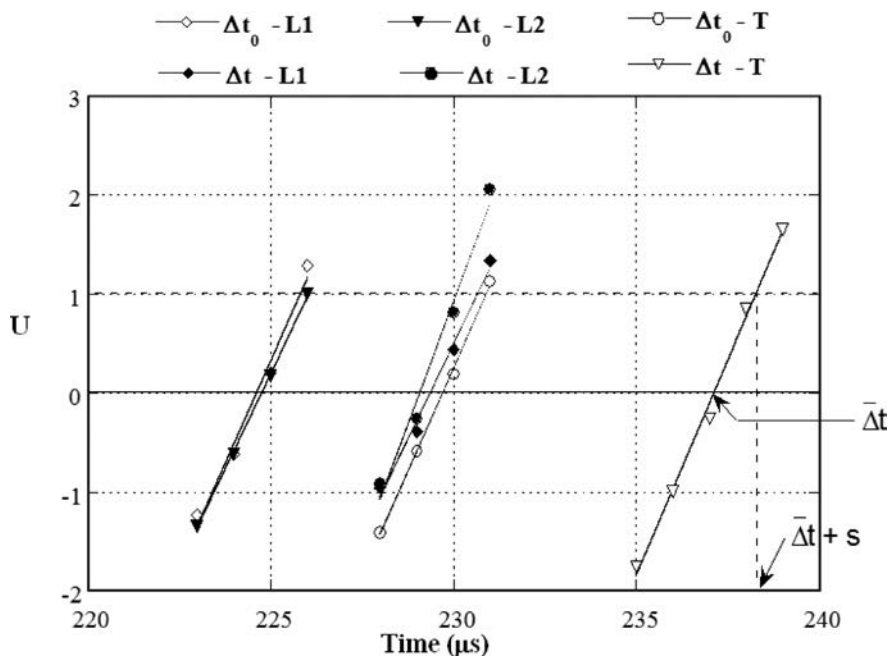


FIG. 10. Graphical adjustment to the law of Laplace-Gauss obtained for the compression directions **T**, **L1** and **L2**.

In Table 3, we have presented the theoretical Mean value ($\overline{\Delta t_0}$ and $\overline{\Delta t}$) and standard deviation S , calculated by the method of Henry, for three compression directions.

Table 3. Comparison: experiment vs. Henry's method.

		L1		L2		T	
		Δt_0	Δt	Δt_0	Δt	Δt_0	Δt
Henry's method	Standard deviation S	1.2000	1.3000	1.2888	1.0000	1.1889	1.1666
	Mean value (μs)	224.6	226.36	224.76	229.08	229.70	237.12
Experimental method	Standard deviation S	1.0671	1.1604	1.0671	0.9947	1.1686	1.0726
	Mean value (μs)	224.72	229.42	224.79	229.21	229.67	237.11

We have concluded that the graphical estimations of $\overline{\Delta t}$, $\overline{\Delta t_0}$ and S (standard deviation) differ slightly from the values $\overline{\Delta t_0}$, $\overline{\Delta t}$ and S determined through the described method (see Table 3).

From this comparative study, it appears the normal law is completely efficient to describe the frequential evolution of the elastic wave propagation time in the Hopkinson bar (with or without specimen). Finally, this adjustment method using the normal law has been adopted for all statistical analysis of our experimental results. In Fig. 11, we have presented the distribution functions of the variables Δt_0 and Δt for three tested compression directions. The functions are defined by the following expression:

$$(2.10) \quad P(\Delta t) = \int_{-\infty}^{+\infty} p(\Delta t) d(\Delta t).$$

The probability density functions obtained in the analysis have a similar allure for all compression directions **L** or **T**.

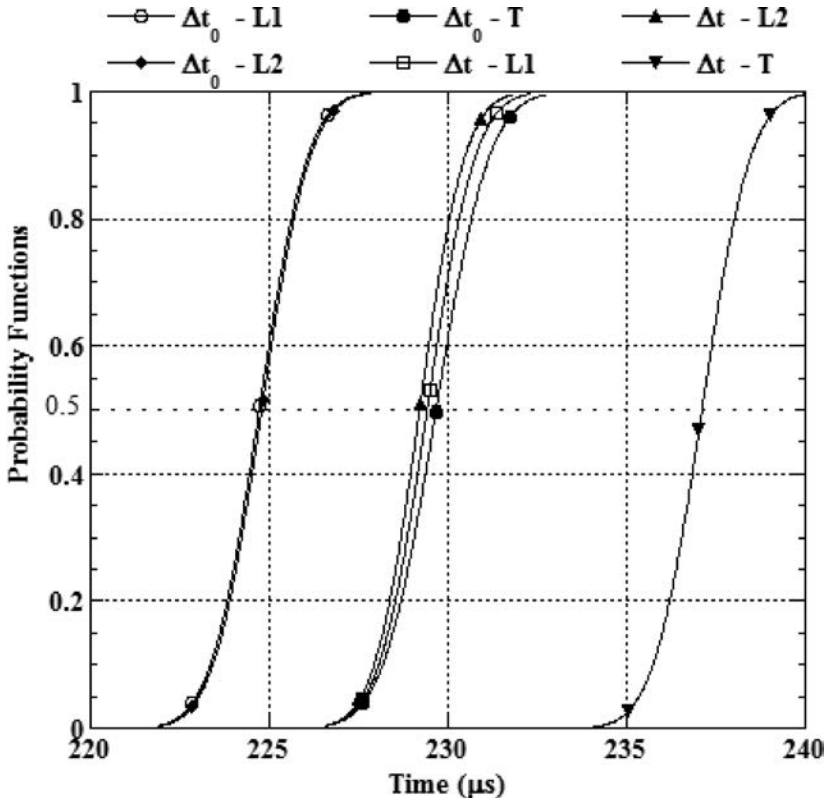


FIG. 11. Probability functions obtained for the compression directions **T**, **L1** and **L2**.

3. DYNAMIC ELASTIC MODULUS

Whilst it can be easily demonstrated that for metallic materials the elastic modulus is practically constant for any strain rate (conservation of the static value), it is not the case for viscoplastic materials such as most of polymers or composite materials with the polymer matrix.

Under dynamic loading, the phenomena of rotation or slipping may change a molecular structure of the polymer matrix, both in the crystalline and amorphous phase [9]. This change in structure may result in a change of the Young modulus which is a physical value linked to the material structure, in particular to the molecular orientation [10]. This is why it becomes so important to estimate the Young modulus in dynamic conditions.

The instant dynamic elastic modulus E_d is given by:

$$(3.1) \quad E_d(\sigma) = \left(\frac{\partial \sigma}{\partial \varepsilon} \right)_\sigma ; \quad \sigma > 0.$$

For stresses close to zero, the wave celerity does not depend on its frequency [7], therefore E_d is reduced to:

$$(3.2) \quad E_d = \rho_0 C_{0s}^2,$$

where ρ_0 is the mean value of the specimen density of the composite material used in the tests. For short loading intervals of time, $0 < t < 2\Delta t_s$, the celerity $C_{0s}(\sigma)$ is determined by:

$$(3.3) \quad \left(\frac{\partial \sigma}{\partial \varepsilon} \right)_\sigma = \rho_0 C_{0s}^2(\sigma).$$

The stress-strain relation is defined by the following equation:

$$(3.4) \quad \varepsilon = \frac{1}{\rho_0} \int_0^\sigma \frac{d\sigma}{C_{0s}^2(\sigma)} ; \quad \sigma = \text{constant}.$$

The wave celerity $C_{0s}(\sigma)$ is a slightly decreasing function of σ .

In Table 4, we have presented the values of the dynamic elastic modulus calculated by Eq. (3.2) for three compression directions.

Table 4. Dynamic elastic modulus for three compression directions.

Compression directions	L1	L2	T
E_d (MPa)	20691	23085	10098

4. IMPACT OF STRAIN RATE ON THE ELASTIC MODULUS

In order to study the impact of strain rate on the elastic modulus, the compression tests in quasi-static conditions have been carried out using a hydraulic machine (Zwick REL). The compression dynamic tests have been performed with the Hopkinson bar system. The range of strain rates: 10^{-5} s^{-1} to 2300 s^{-1} .

Three specimens have been used for each test condition. Figures 12, 13, and 14 present a synthesis of stress-strain curves for the composite PA6/glass, loaded in the parallel and perpendicular direction to fibers.

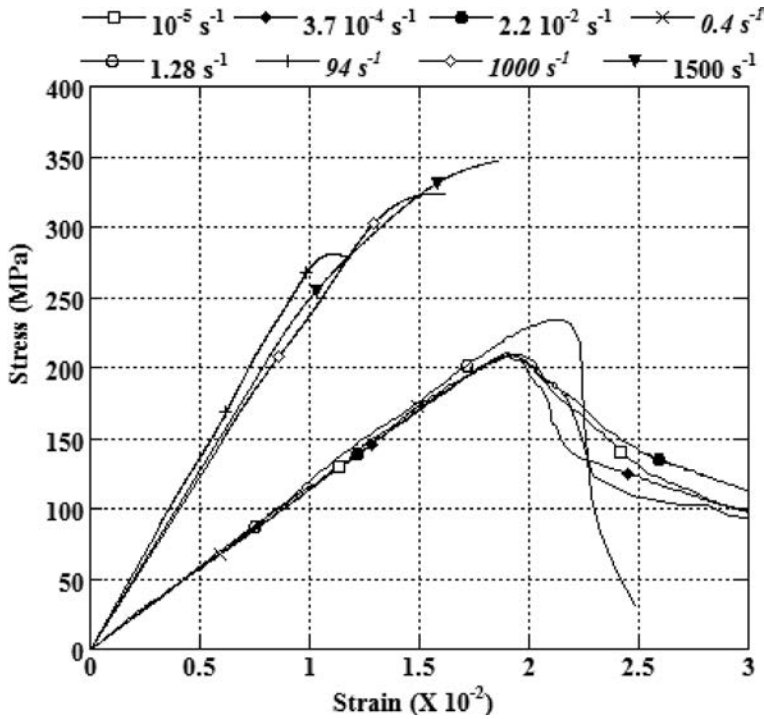


FIG. 12. Stress-strain curve at different strain rates, compression direction L1.

The dynamic modulus is higher than the static modulus obtained during the quasi-static compression tests. Table 5 reveals this difference which proves a high viscosity of the matrix.

Table 5. Dynamic elastic modulus for three compression directions.

Compression directions	E_s (MPa)	E_d/E_s	$(E_d - E_s)/E_s$ (%)
L1	11281	1.8	83.4
L2	11466	2.0	101.3
T	5265	1.9	91.8

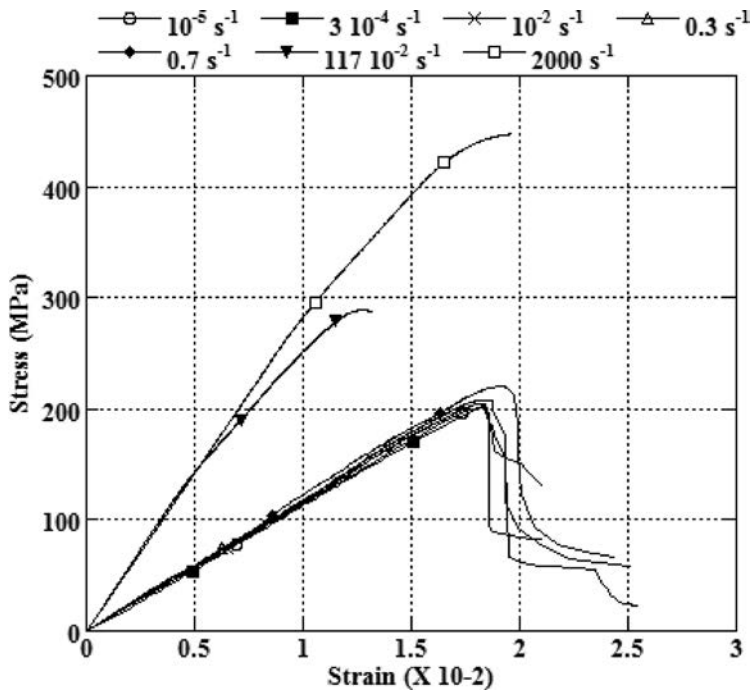


FIG. 13. Stress-strain curve at different strain rates, compression direction L2.

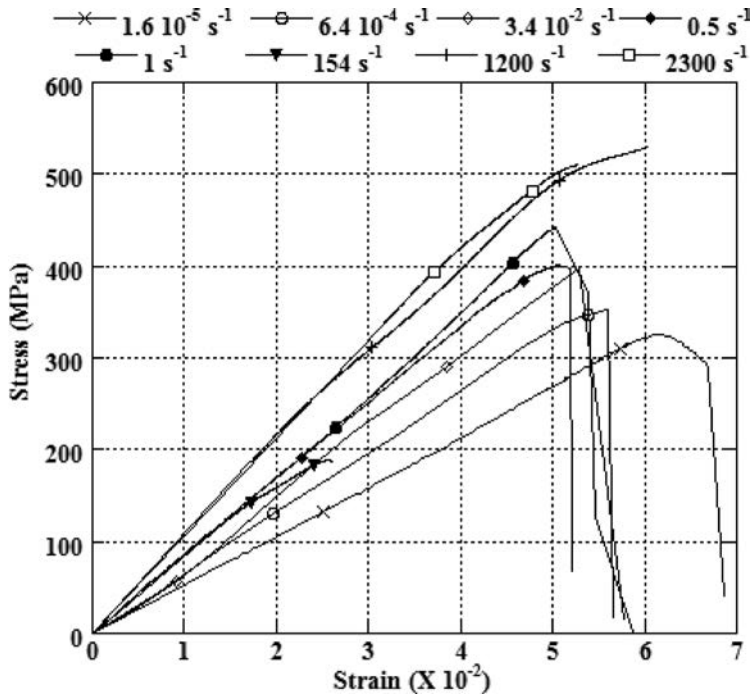


FIG. 14. Stress-strain curve at different strain rates, compression direction T.

Figure 15 shows the elastic modulus is sensitive to the strain rate because the values obtained in dynamic tests are higher than those from quasi-static ones. As far as compression in fibers direction is concerned, we can also observe a slight strain rate sensitivity for quasi-static loadings. On the other hand, the modulus increases linearly above $\dot{\epsilon} = 1 \text{ s}^{-1}$. In case of the compression direction **T**, the elastic modulus seems to vary linearly as a function of log for both ranges of strain rates (quasi-static and dynamic). A linear correlation leads to the following equation:

$$(4.1) \quad E_T = E_0 + \beta \log(\dot{\epsilon}/\dot{\epsilon}_0).$$

For $\dot{\epsilon}_0 = 1 \text{ s}^{-1}$, the quasi-static modulus in the compression direction **T**, $E_0 = 8577.7 \text{ MPa}$, β is the sensitivity coefficient of the elastic modulus to the strain rate, $\beta = 673.41$.

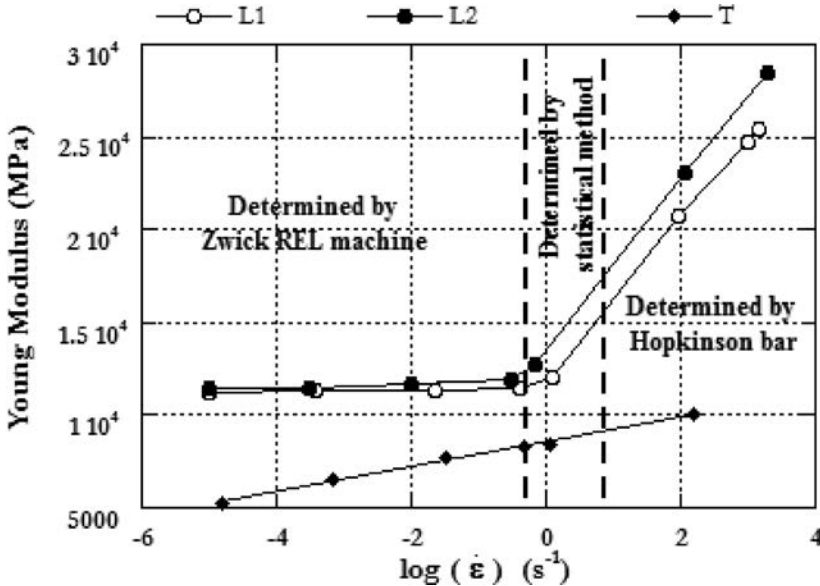


FIG. 15. Impact of the strain rate on the elastic modulus.

5. CONCLUSIONS

From the tests obtained, we can conclude and confirm the Hopkinson bar system enables to measure the wave propagation velocity in composite materials and calculate dynamic elastic modulus. In contrast to acoustic methods, this technique allows for determination of the elastic modulus in the large range of stresses and at very low frequencies.

This conclusion opens a perspective to evaluate all dynamic elastic parameters (ν , G and E) for viscoelastic materials of a brittle or semi-brittle nature.

REFERENCES

1. OLSEN C., FABRICIUS L. IDA., KROGSBOLL A., PRASAD M., *Static and dynamic Young's Modulus for Lower Cretaceous chalk. A low frequency scenario*, AAPG International Conference, Cancun, Mexico, 24-27, October 2004.
2. OLSEN G.T., WOLFENDEN A., HEBUR M.G., *Experimental Investigation of the Dynamic Elastic Modulus and Vibration Damping in $MoSi_2$ -30% Si_3N_4 as a Function of Temperature*, Journal of Materials Engineering and Performance, **9**, 1, 116–119, 2000.
3. SRIKANATH N., SARAVANARANGANATHAN D., GUPTA M., LU L., LAI M.O., *Modelling and determination of dynamic elastic modulus of magnesium based metal matrix composites*, Materials Science and Technology, **16**, 3, 309–314, 2000.
4. ZHENG. L., SHARON HUO X., YUAN Y., *Experimental investigation on dynamic properties of rubberized concrete*, Construction and Building Materials, **22**, 939–947, 2008.
5. TARFAOUI M., CHOUKRI S., NEME A., *Effect of fibre orientation on mechanical properties of the laminated polymer composites subjected to out-of-plane high strain rate compressive loadings*, Composites Science and Technology, **68**, 2, 477–485, 2008.
6. KLEPACZKO J.R., *The modified Split Hopkinson Bar*, Theoretical and Applied Mechanics, **4**, 479–491, 1971.
7. KLEPACZKO J.R., *Quasi-static and Dynamic Compression Behavior of Coal*, Technical Report No. 1, Dept. of Mech. Engng., The University of Manitoba, Winnipeg, 1982.
8. SAPORTA G., *Probabilités analyse des données et statique*, Ed. Technip, Paris, 1990.
9. VERMEULEN B., GUEGUEN V., BERGÉ F., PERRING F., LAM T.M., REFFO G., *Résistance à l'impact des matériaux composites à base de tissus de polyéthylène haute performance, polyaramide et verre*, Composites, **19**, 53–57, 1997.
10. WORD I.M., *Mechanical properties of solid polymers*, Ed. Wiley, London, 1983.

Received November 9, 2013; revised version December 22, 2013.

From the Editorial Board

Our Reviewers

The Editorial Committee wishes to express many thanks and appreciation to all the referees, listed below, for their valuable opinions concerning papers submitted to the Engineering Transactions in 2013:

M. Bijak-Żochowski	P. Lacki
A. Brandt	P. Lipinski
L. Dietrich	G. Mikułowski
L. Drenchev	Z. Mróz
H. Garbalińska	K. Nalepka
R. Gieleta	Z. Nowak
W. Grzesik	J. P. Okrajni
T. Jankowiak	A. Styczek
Ł. Jankowski	W. Sumelka
A. Z. Kocańda	J. Szumbariski
M. Kotełko	W. Zębala

Received reviews for articles published in 2013 year.



POLISH ACADEMY OF SCIENCES
Institute of Fundamental
Technological Research
and Committee on Mechanics



Morskie Oko in Tatra National Park



Hotel Belvedere - Venue of the Conference
ul. Droga do Białego 3, Zakopane

S^{39th}oiMech
2014

**39th SOLID MECHANICS
CONFERENCE
Zakopane, Poland
September 1-5, 2014**

<http://solmech2014.ippt.pan.pl/>

Invited Plenary Lectures:

Holm Altenbach, Germany

Mechanics of Nanostructures

Josef Eberhardsteiner, Austria

Mechanical Behavior of Wood – a Bridge from Microstructure to Structural Applications by Means of Computational Methods

Narinder Gupta, India

Some Aspects of Large Deformations of Structures under Dynamic Loading

David Hayhurst, UK

High-temperature Continuum Damage Mechanics. Simulation of Materials and Components from Processing and Manufacture to Component Performance

Shaker Meguid, Canada

Multiscale Modelling of Multifunctional Nanocomposites for Aerospace Applications

Ryszard Pęcherski, Poland

Plastic Flow and Failure of Solids. Modelling Across Scales

Krzysztof Wiśniewski, Poland

Recent Improvements in Mixed/Enhanced Shell Elements with Drilling Rotation

Ramon Zaera Polo, Spain

Deformation of Dynamically Phase Transforming Metals in Adiabatic Conditions: Thermal Effects and Instabilities

Important dates

Abstract submission deadline	28 February 2014
Notification of acceptance	30 March 2014
Early conference fee payment deadline	31 May 2014
Conference fee payment deadline	30 June 2014
Conference time:	1–5 September 2014

Registration

Registration for the Conference should be performed on-line using the registration form available at

<http://solmech2014.ippt.pan.pl/>

Conference Fee

Registration fee:	before 31.05.2014	after 31.05.2014
Full	1800 PLN	2050 PLN
Student	1200 PLN	1450 PLN
Accompanying person	800 PLN	800 PLN

Contact: Institute of Fundamental Technological Research
phone: +48 22 826 98 34 fax: +48 22 826 73 80
e-mail: solmech2014@ippt.pan.pl

Further informations & guidelines will be available at the Conference site:

www.solmech2014.ippt.pan.pl

DIRECTIONS FOR THE AUTHORS

The periodical *ENGINEERING TRANSACTIONS (ROZPRAWY INŻYNIERSKIE)* presents original papers which should not be published elsewhere.

As a rule, the volume of a paper should not exceed 40 000 typographic signs. The following directions are particularly important:

1. **The paper submitted for publication should be written in English.**
2. The title of the paper should be as short as possible. The text should be preceded by a brief introduction; it is also desirable that a list of notations used in the paper should be given.
3. Short papers should be divided into section and subsection, long papers into sections, subsections and points. Each section, subsection or point must bear a title.
4. The formula number consists of two figures: the first represents the section number and the other the formula number in that section. Thus the division into subsections does not influence the numbering of formulae. Only such formulae should be numbered to which the author refers throughout the paper. This also applies to the resulting formulae. The formula number should be written on the left-hand side of the formula; round brackets are necessary to avoid any misunderstanding. For instance, if the author refers to the third formula of the set (2.1), a subscript should be added to denote the formula, viz. (2.1)₃.
5. All the notations should be written very distinctly. Special care must be taken to distinguish between small and capital letters as precisely as possible. Semi-bold type must be underlined in black pencil. Explanations should be given on the margin of the manuscript in case of special type face.
6. Vectors are to be denoted by semi-bold type, transforms of the corresponding functions by tildes symbols. Trigonometric functions are denoted by sin, cos, tan and cot, inverse functions – by arcsin, arccos, arctan and arc cot; hyperbolic functions are denoted by sh, ch, th and cth, inverse functions – by Arsh, Arch, Arth and Arcth.
7. The figures in square brackets denote reference titles. Items appearing in the reference list should include the initials of the first name of the author and his surname, also the full of the paper (in the language of the original paper); moreover:
 - a) In the case of books, the publisher's name, the place and year of publication should be given, e.g., 5. ZIEMBA S., *Vibration analysis*, PWN, Warszawa 1970;
 - b) In the case of a periodical, the full title of the periodical, consecutive volume number, current issue number, pp. from ... to ..., year of publication should be mentioned; the annual volume number must be marked in semi-bold type as to distinguish it from the current issue number, e.g., 6. SOKOŁOWSKI M., *A thermoelastic problem for a strip with discontinuous boundary conditions*, Arch. Mech., **13**, 3, 337–354, 1961.
8. The authors should enclose a summary of the paper. The volume of the summary is to be about 100 words, also key words are requested.
9. The preferable format for the source file is TeX or LaTeX while MS Word is also acceptable. Separate files for the figures should be provided in one of the following formats: EPS or PostScript (preferable), PDF, TIFF, JPEG, BMP, of at least 300 DPI resolution. The figures should be in principle in gray-scale and only if necessary the color will be accepted.

Upon receipt of the paper, the Editorial Office forwards it to the reviewer. His opinion is the basis for the Editorial Committee to determine whether the paper can be accepted for publication or not.

Once the paper is printed, the issue of Engineering Transactions free of charge is sent to the author. Also the PDF file of the paper is forwarded by the e-mail to the authors.

Editorial Committee
ENGINEERING TRANSACTIONS



PRELIMINARY PROGRAMME 2014

http://www.cism.it/about/2014_Courses

ADVANCED SCHOOLS

JUAN CARLOS SIMO SESSION

Complex Viscous Flows <i>Coordinators: A. Sellier (Palaiseau, F), S. Osamu (Tokyo, J)</i>	May 19 – 23
Collective Dynamics of Particles: from Viscous to Turbulent Flows <i>Coordinators: G. Bouchet (Aix-Marseille, F), C. Marchioli (Udine, I)</i>	May 26 – 30
Extremely Deformable Structures <i>Coordinator: D. Bigoni (Trento, I)</i>	June 2 – 6
Topology Optimization of Structures and Continua – Computational Aspects and Background <i>Coordinators: G. Rozvany (Budapest, H), G. Paulino (Urbana, IL, USA)</i>	June 9 – 13
Mechanobiology of Cells and Tissues: Motility and Morphogenesis <i>Coordinators: A. De Simone (Trieste, I), M. Arroyo (Barcelona, E)</i>	June 16 – 20
20 th CISM-IUTAM International Summer School on "Multiscale Mechanobiology of Bone Remodeling and Adaptation" <i>Coordinator: P. Pivonka (Crawley, AUS)</i>	June 23 – 27
Flowing Soft Matter: Bridging the Gap between Statistical Physics and Fluid Mechanics <i>Coordinators: D. Bartolo (Lyon, F), D. Saintillan (Urbana, IL, USA)</i>	June 30 – July 4
Cavitation Instabilities and Rotordynamic Effects in Turbopumps and Hydroturbines <i>Coordinators: L. d'Agostino and M.V. Salvetti (Pisa, I)</i>	July 7 – 11
Structure and Multiscale Mechanics of Carbon Nanomaterials <i>Coordinator: O. Paris (Leoben, A)</i>	July 21 – 25

D. HOWELL PEREGRINE SESSION

Electrospinning: from Electrohydrodynamic to Controlled Structure and Physical Properties of Nanofibers <i>Coordinators: P. Sjakiewicz (Warsaw, PL), E. Zussman (Technion City, IL)</i>	September 1 – 5
Ferroc Functional Materials: Experiment, Modeling and Simulation <i>Coordinators: J. Schröder and D. Lupascu (Duisburg-Essen, D)</i>	September 8 – 12
Shell-like Structures – Advanced Theories and Applications <i>Coordinators: H. Altenbach (Magdeburg, D), V. Eremeyev (St. Petersburg, RUS)</i>	September 15 – 19
Singular Configurations of Mechanisms and Manipulators <i>Coordinators: D. Zlatanov (Genoa, I), A. Müller (Chemnitz, D)</i>	September 22 – 26
Advanced Finite Element Technologies <i>Coordinators: J. Schröder (Duisburg-Essen, D), P. Wriggers (Hannover, D)</i>	October 6 – 10

ADVANCED PROFESSIONAL TRAINING

Advances in Medium and High Temperature Solid Oxide Fuel Cells Technology <i>Coordinators: M. Boaro (Udine, I), A. Arico (Messina, I)</i>	July 14 – 18
Seismic Safety Assessment and Design of Chemical and Process Plants under Accident Conditions <i>Coordinators: O.S. Bursi (Trento, I), S.A. Karamanos (Volos, GR)</i>	October 13 – 17

OTHER EVENTS

ROMANSY-2014 20 th CISM-IFTtoMM SYMPOSIUM on "Theory and Practice of Robots and Manipulators" <i>General Chair: R. Ganiev (Moscow, RUS)</i>	June 23 - 26
Fundamentals and Applications of Ceria in Catalysis <i>Coordinators: A. Trovarelli (Udine, I), P. Fornasiero (Trieste, I)</i>	July 11 – 14

HOSTED MEETING

Corso EuroSDR Edu-Serv 11 E-Learning Courses 2014 Course Seminar <i>Coordinators: F. Crosilla (Udine, I), F. Remondino (Trento, I)</i>	March 24 – 28
---	---------------

